

**DEPARTMENT OF PHYSICS AND ASTRONOMY  
UNIVERSITY OF HEIDELBERG**

Bachelor Thesis in Physics  
submitted by

**Pascal Becht**

**2018**

born in Neuenbürg (Germany)



# **Quality assurance of gas electron multiplier foils for the ALICE TPC upgrade via leakage current measurements**

This Bachelor Thesis has been carried out by Pascal Becht at  
GSI Helmholtzzentrum für Schwerionenforschung GmbH, Darmstadt (Germany) and  
Physikalisches Institut Universität Heidelberg, Heidelberg (Germany)  
under the supervision of  
Prof. Dr. Silvia Masciocchi



## Abstract

Within the upgrade of the ALICE experiment's time projection chamber the current multi-wire proportional chambers are replaced by gas electron multiplier (GEM) based ones. GEM electrodes are perforated, copper-clad polyimide foils, which provide electron multiplication capabilities. Before they are assembled inside the new readout chambers, it is indispensable that the GEM foils undergo an extensive quality assurance program. A key measure for the quality of a GEM foil is the amount of *leakage current* that goes through the foil, when a high potential difference is applied between the two metal layers.

This thesis presents the measurement (procedure) of these small leakage currents through the GEM foils. A comparability check of the data from different institutes that perform leakage current tests with the same GEM foils revealed that the overall measured current levels deviate strongly.

Moreover, a statistical analysis of the leakage current data is done in order to identify different determining factors. It is found that the leakage current of a GEM foil increases with increasing active area and decreasing pitch size of the holes. Additionally, the impact of the geometrical GEM hole properties on the leakage current is investigated. There, an indication that the leakage current correlates with the electric field inside the holes is identified. Furthermore, limitations and possible improvements for this analysis are discussed.

## Zusammenfassung

Ein zentraler Bestandteil in der Aufrüstung der Zeitprojektionskammer des ALICE Experiments ist der Austausch der derzeitigen Vieldrahtproportionalkammern durch auf Gaselektronenvervielfacher (GEM) basierten Ausleseammern. GEM Elektroden sind beidseitig mit Kupfer beschichtete, perforierte Polyimidefolien, die sich zur Elektronenvervielfachung eignen. Bevor sie in den Ausleseammern verbaut werden können, ist es unabdinglich, dass die GEM-Folien einer umfassenden Qualitätssicherung unterzogen werden. Dabei ist die Stärke des Leckstroms, welcher fließt sobald eine Hochspannung zwischen den beiden Metallschichten angelegt wird, ein zentrales Maß für die Qualität dieser GEM-Folie.

Diese Arbeit beschreibt die Messung solch kleiner Leckströme durch eine GEM-Folie. Desweiteren wurde eine Vergleichbarkeitsprüfung zwischen den verschiedenen Instituten, die die Leckstrommessung an den selben Folien durchführen, durchgeführt. Es stellte sich heraus, dass die gemessenen Stromwerte verschiedener Institute stark voneinander abweichen.

Um verschiedene Einflussgrößen des Leckstroms durch eine GEM-Folie zu untersuchen, wurden die Messdaten einer statistische Auswertung unterzogen. Es wurde herausgefunden, dass der Leckstrom mit wachsender aktiver Fläche und geringerem Lochabstand ansteigt. Zusätzlich wurde der Einfluss von geometrischen Eigenschaften der Löcher auf den Leckstrom untersucht. Hierbei wurden Anzeichen gefunden, dass der Leckstrom mit dem elektrischen Feld in den Löchern korreliert ist. Abschließend wird über Einschränkungen und Verbesserungsmöglichkeiten dieser Analyse diskutiert.



# Contents

	Page
<b>1 The ALICE experiment</b>	<b>1</b>
1.1 Introduction to ultra-relativistic heavy-ion physics . . . . .	1
1.1.1 Quark-gluon plasma . . . . .	2
1.1.2 Physics observables . . . . .	4
1.2 Experimental setup . . . . .	5
1.3 The ALICE time projection chamber . . . . .	7
1.3.1 Working principle . . . . .	8
1.3.2 Concept of particle identification with a TPC . . . . .	9
<b>2 Introduction to gas electron multipliers</b>	<b>12</b>
2.1 Working principle and performance . . . . .	12
2.2 Different applications . . . . .	14
<b>3 The ALICE TPC upgrade</b>	<b>17</b>
3.1 Motivation . . . . .	17
3.2 Readout chamber design . . . . .	19
3.3 Design and characteristics of the GEM foils . . . . .	20
3.4 TPCU workflow and quality assurance . . . . .	22
<b>4 The leakage current test</b>	<b>24</b>
4.1 Testing equipment . . . . .	24
4.2 Experimental setup . . . . .	26
4.3 Testing procedure . . . . .	27
4.4 Measurement process and data . . . . .	30
<b>5 Determining factors of leakage current</b>	<b>33</b>
5.1 Post-processing of the leakage current data . . . . .	33
5.2 Data comparison between the measurement sites . . . . .	34
5.3 Area dependence of leakage current . . . . .	36
5.3.1 Results and discussion . . . . .	37
5.4 Pitch size dependence of leakage current . . . . .	40
5.4.1 Results and discussion . . . . .	41
5.5 Dependence of the leakage current on hole properties . . . . .	43
5.5.1 Post-processing of hole size data . . . . .	44
5.5.2 Results and discussion . . . . .	46
<b>6 Conclusion and outlook</b>	<b>50</b>
<b>Appendices</b>	<b>53</b>
A.1 List of abbreviations . . . . .	53
A.2 List of figures . . . . .	54

A.3 List of tables . . . . .	55
A.4 Additional figures . . . . .	56
<b>References</b>	<b>56</b>
<b>Acknowledgement</b>	<b>59</b>
<b>Declaration</b>	<b>61</b>

# 1 The ALICE experiment

ALICE, standing for *A Large Ion Collider Experiment*, is one of the four major physics experiments which are located at CERN's Large Hadron Collider (LHC) near Geneva in Switzerland. After the first conceptual ideas at the end of 1990, it was approved as an experiment in 1997 [1]. In contrast to the other experiments at the LHC (ATLAS, CMS and LHCb), ALICE is explicitly dedicated to measure heavy-ion collisions. Therefore, the experiment is designed to study the physics of strongly interacting matter under extreme conditions, such as high energy densities and temperatures. Particularly, the properties of a special state of (nuclear) matter, the quark-gluon plasma (QGP), are investigated. It is the state of our early universe, which existed throughout a few microseconds after its creation in the Big Bang [2].

To achieve the physics goals of ALICE a multi-purpose detector system is used. It is capable of detecting hadrons, electrons, muons and photons, which are created in the collisions of heavy ions. The main ion collision system is lead-lead (Pb-Pb), however there is the possibility of colliding lighter ions, such as xenon-xenon (Xe-Xe) in order to vary the interaction volume (system size). Additionally, proton-lead (p-Pb) collisions are recorded for a certain period of time. Since only 28 days per year are dedicated for the LHC ion runs [3], ALICE also takes data during proton-proton (pp) collisions, which also serves as a reference for the heavy-ion programme [4].

## 1.1 Introduction to ultra-relativistic heavy-ion physics

Under normal conditions, like they predominate in our current universe, *quarks* and *gluons* are bound into composite objects known as hadrons. To be more precise, quarks and their antiparticles, the antiquarks, are the elementary building blocks of hadronic matter, which is held together by gluons that carry the *strong interaction*. According to the Standard Model of particle physics (anti)quarks and gluons carry colour-charge, whereas the hadrons as their composite particles are colour-neutral. Due to this constraint, there are quark triples, the *baryons*, and pairs of one quark and one antiquark, the *mesons*. Both nucleons, the proton and the neutron, are prime examples of baryons, which build nuclear matter. The phenomenon that quarks do not appear as freely moving particles, but are bound in more complex objects is called (*colour*) *confinement*.

This phenomenon of confinement is caused by a unique feature of the strong interaction, which can be described by the according quantum field theory, *Quantum Chromodynamics* (QCD). It results from the functional dependence of the strength of the force on the distance between the strongly interacting particles that carry colour-charge, such as quarks. For small distances below the nucleon radius, i.e. smaller than 0.9 fm [5], the coupling constant of the strong interaction nearly vanishes. This effect gives rise to quarks moving quasi-free over small distances, which is denoted as *asymptotic freedom*. In the opposite direction, i.e. for larger distances, the force between two quarks increases. In contrast to the (electrically) uncharged photon, which carries the electromagnetic force, gluons carry colour charge. This makes strong gluon-gluon coupling possible, while there is no electromagnetic coupling between photons. As a consequence, the gluon field between the quarks forms *flux tubes* (often referred to as colour strings), which cause the increase of the strong force with distance [6]. Thus, the analogy of a rubber band between two particles is often made to illustrate this behaviour of the strong interaction, since there the tension also increases with a growing distance.

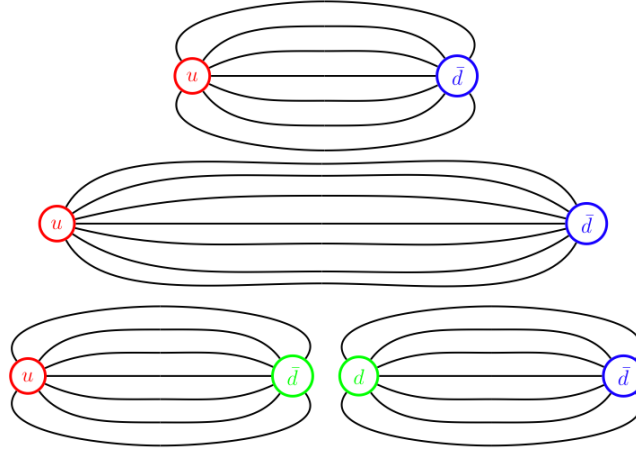


**Figure 1.1** Sketch to illustrate quark confinement using the example of an up ( $u$ ) and an antidown ( $\bar{d}$ ) quark. Black (field) lines represent the flux tube. At the bottom the fragmentation process, as described in the text, can be seen [7]

If the quarks are further separated to a critical distance, where the energy of the gluon field exceeds the mass energy of a quark-antiquark pair, it becomes energetically favourable to spontaneously form such a pair. Effectively, two new bound states are built. By reason of this process, which is illustrated in figure 1.1, the quarks stay confined instead of being free, but the energy in the gluon field is reduced by building two shorter flux tubes. This is called (*string*) *fragmentation* or *hadronisation* [7].

However, QCD predicts a transition from conventional hadronic or nuclear matter to a *deconfined* state of matter at sufficiently high densities and/or temperatures. This means that the quarks and gluons in this special phase of matter are no longer bound, but can move freely over distances, which are significantly larger than the dimensions of a nucleon. Since this deconfined state of matter shows properties, which are analogue to an ordinary plasma, it is referred to as quark-gluon plasma (QGP). The QGP is the extreme state of matter in the early universe within a few microseconds after the Big Bang. Owing to the progress in accelerator technology, nowadays the QGP can be experimentally created in heavy-ion collisions at ultra-relativistic energies [2].

### 1.1.1 Quark-gluon plasma

Since the QGP is predicted by QCD calculations, the transition from ordinary nuclear matter to QGP must happen at temperatures, which are equivalent to the order of the QCD energy scale parameter  $\Lambda_{\text{QCD}} \approx 200 \text{ MeV}$ . Dividing this value by the Boltzmann constant  $\kappa = 8.617\,330\,3 \times 10^{-5} \text{ eV K}^{-1}$ , the critical (transition) temperature  $T_c$  is of the order  $10^{12} \text{ K}$  [4, 5]. In this regime of extreme conditions the common method of solving the QCD equations (by perturbative approximations) is not very reliable anymore. Thus, another approach of solving these equations is needed. This can be done by numerical calculations on a lattice for vanishing baryochemical potential  $\mu_B$ , which is a measure for the energy needed to add one baryon to the considered system.

According to such lattice QCD calculations it is predicted that the QGP forms at energy densities of at least  $1 \text{ GeV fm}^{-3}$ , while the energy density of nuclear matter in the ground state is of the order  $\epsilon_0 \approx 0.15 \text{ GeV fm}^{-3}$ . The corresponding (pseudo-)critical temperature is calculated to be in the range  $155 - 160 \text{ MeV}$ , which is still subject of ongoing research [2].

To be able to investigate fundamental properties of the QGP, it can be experimentally created in heavy-ion collisions at (ultra-)relativistic energies. This is done by different particle accelerator facilities all around the world. For example there is the Relativistic Heavy Ion Collider (RHIC) at

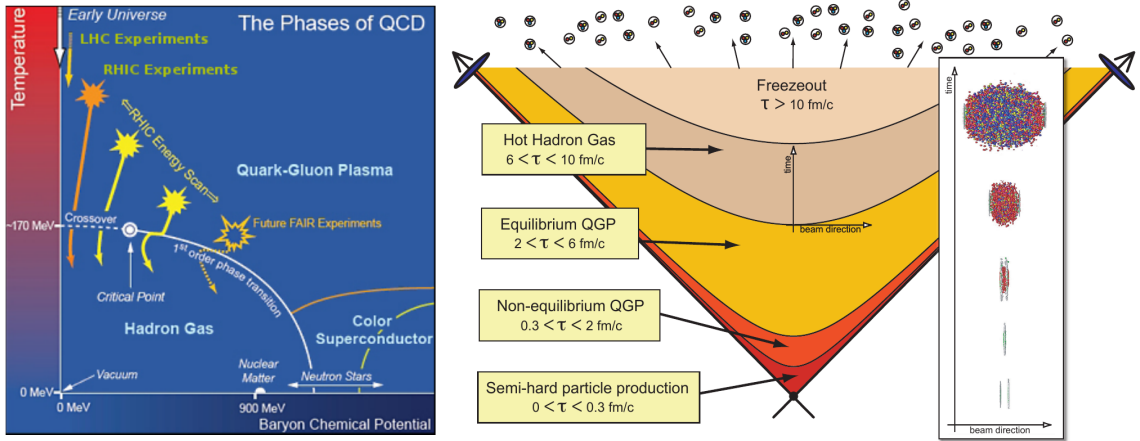


**Figure 1.2 (left)** Semi-qualitative sketch of the QCD phase diagram of nuclear matter. The temperature is shown on the vertical axis, while the baryochemical potential ( $\mu_B$ ) is shown on the horizontal axis. The white solid line represents the first-order phase transition from hadron gas to the QGP phase. For low  $\mu_B$  there is a crossover region between the two phases (white, dashed line). Additionally, possible paths of artificially created systems in heavy-ion collisions at different accelerator facilities, e.g. CERN (LHC), BNL (RHIC) and the FAIR are indicated in yellowish lines [8].

**(right)** Schema of the space-time evolution of QGP generated by ultra-relativistic heavy-ion collisions at LHC energies. The vertical axis represents the time, while the horizontal axis shows the space coordinate along the beampipe. Different evolution steps of the system are indicated by different colours (red to brownish).  $\tau$  denotes the time passed after the collision. The space-time evolution of the Lorentz contracted nuclei collision in the lab-frame [9]

Brookhaven National Laboratory (BNL), New York, USA, which mainly collides gold ions at *centre-of-mass energies per nucleon pair* up to  $\sqrt{s_{NN}} = 200$  GeV [10], and the Facility for Antiproton and Ion Research, Darmstadt, Germany, which is currently under construction. However, the LHC at CERN, Geneva, Switzerland is probably the most prominent and powerful example. It delivers lead-lead collisions at energies up to  $\sqrt{s_{NN}} = 5.5$  TeV to the four LHC experiments (ALICE, CMS, LHCb, ATLAS) [11].

The physics control parameters of producing a QGP are on the one hand the collision energy of the colliding ions and on the other hand the interaction volume, i.e. the size and the overlap of the geometrical cross section (centrality) of the colliding nuclei. Therefore, different regions of the QCD phase diagram of nuclear matter can be probed by variation of the collision energy. In figure 1.2 on the left a sketch of this phase diagram is shown. As it can be seen there, the LHC provides extremely high temperatures at vanishing  $\mu_B$ , i.e. low baryon density. Therefore, ALICE is well suited to test predictions by lattice QCD (see beginning of this subsection).

Once created in a heavy-ion collision the QGP evolves in space-time. Driven by a pressure gradient it expands in volume and thus cools down. If the temperature drops below a critical value, the QGP undergoes a phase transition from the deconfined back to a confined state. As a consequence of the now active colour confinement, hadrons are built and exist in a gaseous state (hadron gas). This process is indicated in figure 1.2 on the left by yellow and orange trajectories. A more detailed view on the evolution of heavy-ion collisions at LHC energies is given in figure 1.2 on the right. The time intervals ( $\tau$ ) given are rough estimates, but reasonable if a central region in the QGP is considered.

Within the passing time of the two colliding (lead) nuclei initial, hard parton-parton (constituents of the nucleons, i.e. quarks and gluons) scattering takes place. During this time the system is dominated by so-called *hard* particle production. There, the energy is sufficient to produce quark-antiquark pairs of heavy flavours such as charm-anticharm ( $c\bar{c}$ ) or bottom-antibottom

( $b\bar{b}$ ). Also highly energetic partons (e.g. light quarks), which originate so-called *jets* (see next subsection 1.1.2), are produced. Until about 2 fm/c there are large deviations of isotropic thermal equilibrium. After a very short thermalisation time the QGP is in a state of local thermal equilibrium. Thus its dynamics, such as expansion and cooling, are described by linearised viscous hydrodynamics. When the temperature drops below the critical value, the phase transition takes place. Since mesons and baryons are built, the system gets too dilute to be reliably described by hydrodynamics. This process is called *chemical freeze-out*. The hadron yield and the particle abundance (distribution over the particle species) is fixed now, but still the produced hadrons are subject of elastic scattering. Further cooling down the *kinetic freeze-out* occurs. As the elastic scattering ceases, there is no momentum transfer between the hadrons. At this point of time the (momentum) spectra are determined and the hadrons stream freely to the surrounding detectors [2, 9]. There, the hadrons themselves or their decay products can be detected to finally be able to gain information about the properties of the QGP.

### 1.1.2 Physics observables

Since the investigation of the QGP requires a sufficiently large interaction volume, the ALICE experiment exploits the collision of  $^{208}\text{Pb}$ -ions at energies up to  $\sqrt{s_{\text{NN}}} = 5.5$  TeV. However, the life-time of the produced QGP at the LHC is very short. The typical life-time is of the order 10 fm/c, which corresponds to few  $10^{-23}$  s. If this is translated into length scales, the QGP fills a volume of a few thousands of  $\text{fm}^3$  [2]. Both time and spatial dimensions cannot be resolved directly by any experiment in the world. Thus, other observables are needed to characterise the QGP.

Pseudorapidity is a quantity that provides geometrical information on the angle with respect to the beampipe direction. It is defined as  $\eta = -\log(\tan(\vartheta/2))$ , with  $\vartheta$  being the angle between the charged-particle trajectory and the beampipe. Thus,  $\eta = 0$  denote perpendicular particle tracks with respect to the beampipe.

One (key) observable is the *multiplicity* of primary charged particles, which are created in a heavy-ion collision. For a largest possible pseudorapidity ( $\eta$ ) range, the primary charged-particle pseudorapidity density  $dN_{\text{ch}}/d\eta$  and its dependencies on the collision energy, geometry and system can be considered. This provides information on the relative contribution of particle production from hard scattering and soft (thermal) production processes when compared to predictions of different particle production models [12].

In general, a particle can be characterised by its *transverse mass*  $m_{\text{T}} = \sqrt{m_0^2 + p_{\text{T}}^2}$ , where  $m_0$  is the rest mass and  $p_{\text{T}}$  the *transverse momentum*, i.e. the momentum projection in the plane perpendicular to the beampipe direction.

There are a few methods to probe the QGP. One of them is the use of so-called *hard probes*, which stand out because of their high transverse mass of typically more than several GeV. This energy scale is well above the temperature of the medium at the freeze-out. Therefore, they are produced in hard scattering processes during the pre-equilibrium phase of the QGP. Surviving the QGP and strongly interacting with its hot, dense matter they provide information about the QGP properties. Observables of hard probes are production yields of hadrons containing heavy (flavour) quarks (charm, bottom). Also high- $p_{\text{T}}$  hadrons within *jets*, which are narrow sprays of hadrons produced by the hadronisation of a single quark or gluon, interact with the QGP and lose energy (*jet quenching*). As a consequence they are an additional example of hard probes.

Besides this, there are other ways to investigate QGP properties. For example the production of quarkonia, which are bound states of a heavy quark and its corresponding antiquark, is another possible observable. There, the production yield of the  $J/\psi$ -meson ( $c\bar{c}$  ground state) or other quarkonia states ( $c\bar{c}$  and  $b\bar{b}$ ) can be compared to the respective yields in pp collisions. Suppression or enhancement of these yields in heavy-ion collisions provide information about QGP

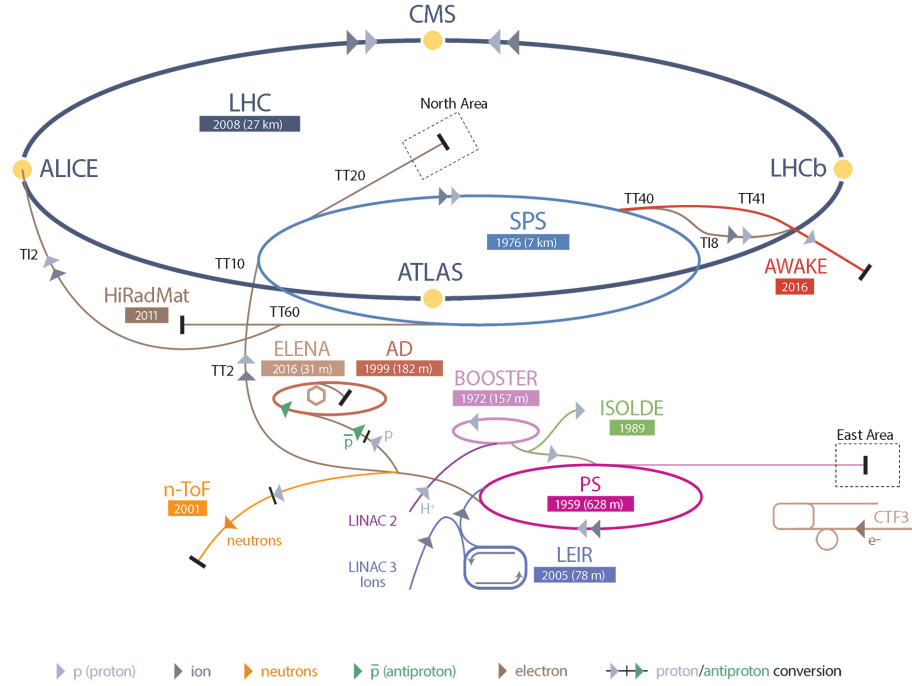


**Figure 1.3** Sketch of the accelerator complex at CERN. The Pb-ions for heavy-ion collisions at the LHC begin their journey in the linear accelerator 3 (LINAC 3). For the main acronyms consult the list of abbreviations (section A.1) [15]

(deconfinement) characteristics. Furthermore, the results can be compared to particle-production model predictions, such as the *statistical hadronisation model* [13].

Since over 99 % of the produced particles are *soft*, i.e. they have a momentum below 2 GeV/c, these *soft probes* are suitable to give access to statistical quantities of the QGP like its temperature and chemical composition [14]. Also hydrodynamic features of the QGP can be tested by considering the so-called *collective flow* of the particles.

In order to gain a multifaceted view on the QGP phenomena, the results from the different probes are combined. For a more detailed overview of QGP observables [2] can be consulted.

## 1.2 Experimental setup

The  $^{208}\text{Pb}$ -ions begin their journey in the linear accelerator 3 (LINAC 3) at CERN's accelerator complex, which is schematically shown in figure 1.3. There, they are pre-accelerated and injected into the Low Energy Ion Ring (LEIR), where they get compressed into short, dense bunches suitable for the Proton Synchrotron (PS). On their path through the PS and the Super Proton Synchrotron (SPS) the ion bunches are further accelerated before they are finally injected into the Large Hadron Collider. About 100 m under the earth they can be collided at the four crossing points.

To measure the products of such lead-lead collisions at ultra-relativistic energies the ALICE experimental setup is located at one of these collision points in an underground cavern. As the dedicated heavy-ion experiment at the LHC ALICE uses an advanced detector system, which is specially designed to meet the challenges due to the high particle densities. For example typically around 2000 to up to 3000 particles are created per collision at  $\sqrt{s_{\text{NN}}} = 5.02$  TeV in the 5 % most central collisions [12]. The properties of these particles have to be determined in order to investigate the QGP as described in subsection 1.1.2. Therefore, excellent particle identification

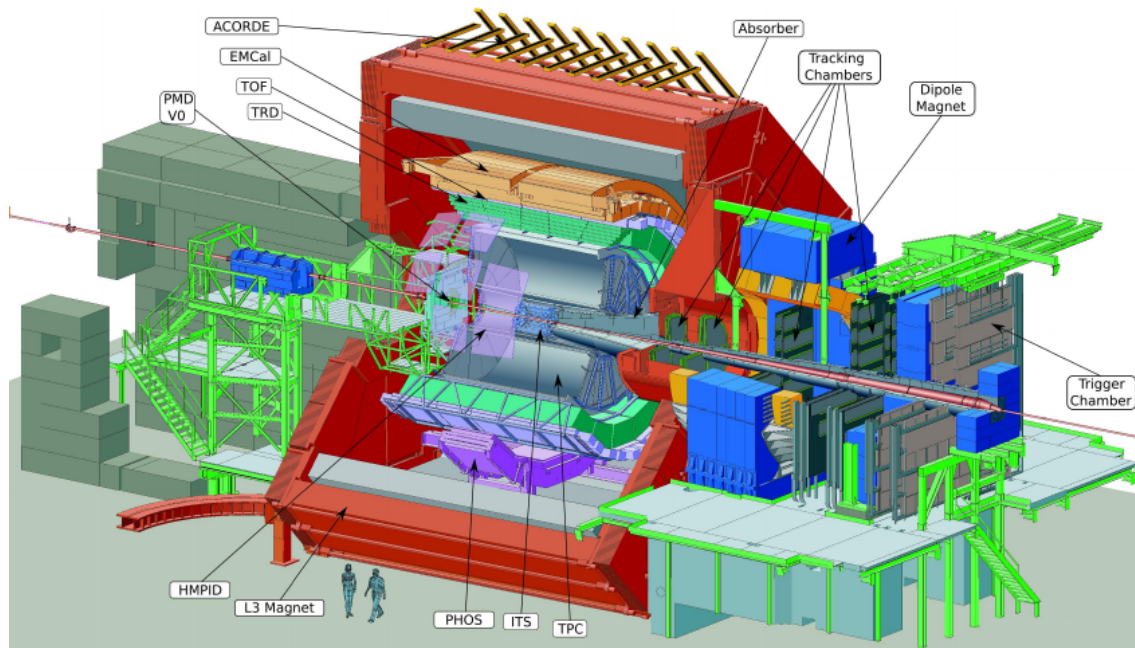


**Figure 1.4** Sketch of the ALICE detector system. The main detectors are labelled. More details on the purposes and technology are given in the text. For the acronyms consult the list of abbreviations (section A.1) [16]

(PID) capabilities in combination with a sufficient granularity are required. Additionally, an as large as possible pseudorapidity range, i.e. large acceptance of the detectors, is needed in order to detect a maximum number of particles that are created in the collision.

As a consequence, the ALICE detector system with all its single components is optimised to meet these requirements and offer the measurement of a broad range of observables at the same time. With its total dimensions of  $16\text{ m} \times 16\text{ m} \times 26\text{ m}$  and a total weight of about  $10\,000\text{ t}$  the entire ALICE detector system (including the magnet) is located around the collision point in an underground cavern. A sketch of the entire experimental setup is shown in figure 1.4. The ALICE experiment consists of a *central barrel* part, where hadrons, electrons and photons are detected, and the *muon arm*, which is a forward muon spectrometer.

The central barrel detectors are embedded in the large, red L3 solenoid magnet, which provides a relatively low, homogeneous magnetic field of  $0.5\text{ T}$ . This allows to experimentally access the detection of particles in the low transverse momentum region down to  $150\text{ MeV}/c$  [17]. Most of the detectors in the central barrel cover the full azimuth angle and are organised in a barrel shape around the interaction point. In the following they are shortly described in ascending order with respect to their distance from the interaction point.

The **Inner Tracking System (ITS)** is the innermost tracking detector of ALICE. It has 6 layers and uses 3 different types of silicon technology (two layers each), namely silicon pixels (SPD), silicon drift detectors (SDD) and silicon strips (SSD). Its main purpose is the determination of the primary vertex and secondary decay vertices with high resolution. It will be replaced by 7 layers of Monolithic Active Pixel Sensors (MAPS) during the next long shutdown (2019–2020).

Surrounding the ITS, there is the **Time Projection Chamber (TPC)**, which is the main tracking detector of ALICE. It is a gas filled drift chamber and provides Particle IDentification (PID) capabilities. Since this is the relevant detector for this thesis, it is described in more detail in section 1.3.

The **Transition Radiation Detector (TRD)** complements the tracking information. By detecting the transition radiation from electrons passing a radiator, it contributes to the electron

identification. This helps to solve ambiguities in PID by the TPC only by improving the electron pion separation.

The next detector layer is the **Time Of Flight detector (TOF)**. It consists of Multi-gap Resistive Plate Chambers (MRPC) and is used for particle identification purposes in the intermediate momentum region (around a few GeV)

One detector not covering the full azimuth angle is the **High-Momentum Particle Identification detector (HMPID)**. It exploits the technology of proximity-focusing Ring Imaging Cherenkov detectors (RICH). Thus, it is used to enhance the PID in the high momentum region ( $p_T > 1 \text{ GeV}/c$ ), where energy-loss measurements in the ITS or the TPC become less accurate.

For energy measurements of electrons and photons there are two different electromagnetic calorimeters. The **Photon Spectrometer (PHOS)** is a lead-tungstate ( $\text{PbWO}_4$ ) crystal calorimeter, which is read out by Avalanche Photo-Diodes (APD). The other one is the larger lead-scintillator sampling **ElectroMagnetic Calorimeter (EMCal)**. Both mainly aim towards the energy measurement of electrons and photons as well as the detection of jets.

Finally, the **ALICE Cosmic Ray Detector (ACORDE)** is placed on the three top faces of the L3 magnet. Consisting of plastic scintillator arrays, it is used to trigger on cosmic muon events and for alignment of the other ALICE tracking detectors.

Along the beampipe direction there are the so-called **Forward Detectors (FWD)**, which are the **Zero Degree Calorimeter (ZDC)**, the **Photon Multiplicity Detector (PMD)**, the **Forward Multiplicity Detector (FMD)**, the **V0** and the **T0**. These are mainly used for further event characterisation (multiplicity) and provide trigger information.

The **muon spectrometer** consists of an absorber for hadrons, electrons and photons, a blue dipole magnet and tracking chambers to detect muons from the  $\mu^- \mu^+$ -decay channel of heavy-flavour vector-mesons such as the  $J/\psi$  ( $c\bar{c}$ ) or the  $\Upsilon$  ( $b\bar{b}$ ). Also *open-heavy-flavour* hadrons, which only contain a single heavy quark, can be detected via this decay channel. The tracking chambers are organised in 5 stations of Cathode Pad Chambers and 2 trigger stations, which use Resistive Plate Chambers.

For a more detailed description of the single detector components consult [1].

### 1.3 The ALICE time projection chamber

The TPC of the ALICE experiment is located in the central barrel and thus is embedded in the large L3 magnet (see figure 1.4). It provides capabilities of three dimensional reconstruction of charged-particle tracks. Furthermore, particle identification can be done by measuring the particle's energy loss in the active volume of the TPC. During the operation with Pb-Pb collisions, the ALICE TPC shows its outstanding strength by dealing with up to 20 000 primary and secondary particle tracks per event.

A detailed sketch of the TPC with all the major components is shown in figure 1.5 on the left. Basically, the ALICE TPC is a cylindrical container, which is filled with the working gas Ne-CO<sub>2</sub>-N<sub>2</sub> (90-10-5). Measuring 5 m in length and 5 m in diameter, the overall gas volume is about 90 m<sup>3</sup>. This makes the ALICE TPC the largest gas filled TPC in the world. It covers the full azimuth angle and a pseudorapidity range of  $|\eta| < 0.9$ , which matches with the other surrounding detectors such as ITS, TRD and TOF.

A central high-voltage electrode (CE), which is made of 23  $\mu\text{m}$  thick aluminised mylar foil, equally subdivides the gas volume into two smaller drift regions. Both of them are closed off by endplates, which are partitioned into 18 trapezoidal sectors. Each of the 36 sectors houses an inner (IROC) and an outer readout chamber (OROC). Currently, the readout chambers are realised as Multi-Wire Proportional Chambers (MWPC), which consist of multiple wire planes and one pad plane like it is shown in figure 1.5 on the right. Additionally, the active gas volume is enclosed in an inner and an outer field cage (FC) consisting of equally spaced strips. By applying 100 kV to

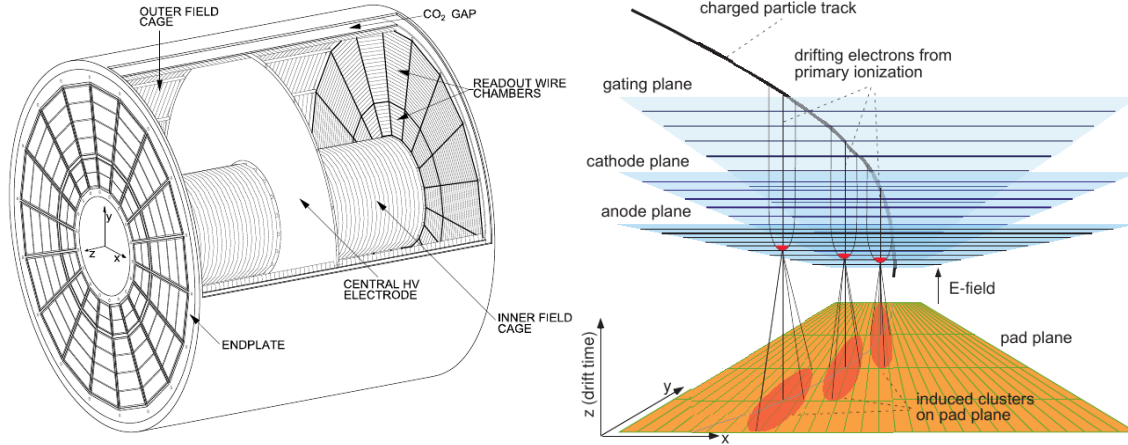


**Figure 1.5** (left) Sketch of the ALICE TPC with all important components. Additionally, the coordinate system is shown [11].  
 (right) Schematic of the TPC readout process by Multi-Wire Proportional Chambers [19]

the central electrode a highly homogeneous electric field between the CE and the readout plane of  $400 \text{ V cm}^{-1}$  is created. The strips of the field cage gradually follow the decreasing potential towards the readout plane and thus further contribute to the field homogeneity. Being operated inside the solenoid magnet, the homogeneous magnetic field of 0.5 T and the drift field in the TPC are aligned. For more detailed information on the ALICE TPC consult [18].

### 1.3.1 Working principle

A TPC is a special kind of drift chamber, which is capable of three dimensional space point measurements. As such it uses the ionisation signal in the working gas. To describe the working principle of a TPC the detection of only one charged-particle track is considered. Fundamentally, it can be characterised by four major steps.

**Electron-ion pair generation** The first step is the *primary ionisation* of the working gas. When a charged particle passes the active gas volume of the TPC, it continuously loses energy according to the *Bethe-Bloch formula* (see equation 1.2). As a consequence, the gas molecules are ionised along the particle track. Since the average energy deposited per electron-ion pair (typically  $\mathcal{O}(30 \text{ eV})$  for gases [20]) is only a very small fraction of the particle's total energy, the particle itself continues on his track practically undisturbed. The result are free electron-ion pairs along the particle track. Additionally, some of the primary electrons can have enough energy to further ionise gas molecules, which is called *secondary ionisation*.

**Drift of ionisation charges** Affected by the applied electric field between CE and readout plane, the free ionisation charges start to drift. The field direction is such, that the faster electrons drift towards the readout chambers to produce a signal, while the ions move in the other direction and are collected at the CE. Due to the field cage the electric field is highly homogeneous, which means that the electrons move relatively straight (z-direction) with only minimal lateral (xy-direction) movement due to diffusion. On their way through the gas the electrons repeatedly collide with the gas molecules. Their drift velocity  $w$  can approximately be described by *Townsend's formula*

$$w = \frac{e}{2m} E \tau, \quad (1.1)$$

where  $e$ ,  $m$  are the electron charge and mass respectively.  $\tau$  is the mean time between collisions, which depends on the gas mixture, pressure, temperature and the electric field strength  $E$ . In the case of the TPC, where all these parameters are controlled, the drift velocity of the electrons is effectively constant.

**Charge amplification** When the electrons arrive at the readout plane, they have to get amplified in order to produce a signal that can be measured and processed by the readout electronics. In the ALICE TPC this is achieved by *gas amplification* in the MWPCs as shown in figure 1.5 on the right. First the electrons pass the *gating grid* (gating plane), which is a wire plane that electrically separates the drift volume of the TPC from the readout region. After a collision happened the gating grid is *open* (totally transparent to electrical charges) for the maximum electron drift time of  $\mathcal{O}(100\ \mu\text{s})$  to collect all ionisation electrons. By the amplification field, which is created by the cathode and anode wire planes, the electrons are guided to the anode wires. In the vicinity of such an anode wire the electric field strength gets extremely large. Thus, the electrons are accelerated towards the wire and gain in energy. At some point they have enough energy to further ionise other gas molecules. In this so-called *avalanche process* the electron signal is amplified by a factor of about  $2 \times 10^4$  [19].

**Signal creation** The electrons are rapidly collected by the anode wire and are not used for the *signal creation*. However, the ions from the gas amplification process remain much longer due to their lower mobility in the gas (about a factor 1000 compared to electrons). While they drift back towards the cathode wires, they induce a mirror charge on the *pad plane*, which is large enough to be detected by the readout electronics. The geometry is chosen such that the induced signal spreads over several adjacent pads. By obtaining the centre of gravity of the charge distribution, a position resolution better than the pad size is achieved. This gives rise to a direct position measurement in the  $xy$ -plane. The  $z$ -coordinate is reconstructed via the drift time (obtained from the arrival time of the signal and a starting time by trigger information) and the constant drift velocity of the electrons.

**Ion backflow** During the gas amplification and signal creation the gating grid stays *closed* to prevent the ions from drifting into the active gas volume. There, they could accumulate and cause massive space point distortions by disturbing the homogeneous drift field. This is achieved by applying positive and negative voltages to the wires in an alternating way, which makes the gating plane completely opaque to electric charges. To ensure an efficient ion collection the gating grid remains closed for about  $180\ \mu\text{s}$  [21].

When a heavy-ion collision has happened, not only one, but thousands of produced charged particles propagate from the interaction point and thus pass the active volume of the TPC. Providing the simultaneous tracking of multiple charged particles in all three dimensions with a high granularity and at the same time offering PID capabilities, the ALICE TPC is the ideal instrument to detect the products of a heavy-ion collisions. Furthermore, it has a low material budget and can easily cover large volumes in order to have an acceptance that is as large as possible.

### 1.3.2 Concept of particle identification with a TPC

As mentioned before, the ALICE TPC has two major tasks. At first, there is the measurement of the three dimensional charged particle tracks, which is already described in the previous subsection 1.3.1. Secondly, the identification of charged particles is done. Therefore, the measurement of

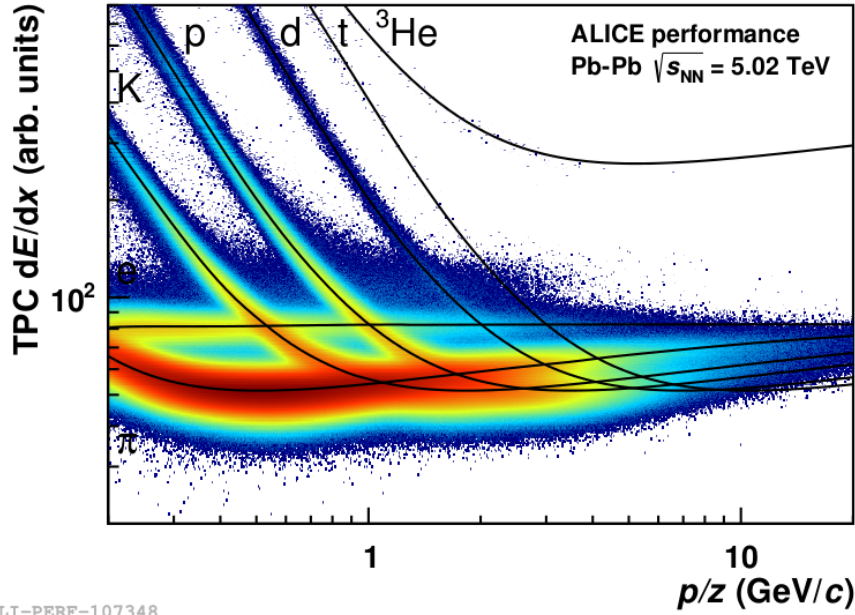


**Figure 1.6** Specific energy loss  $dE/dx$  in the ALICE TPC against rigidity of positive charged particles for particle identification purposes. It is visible that the specific energy loss of pions ( $\pi$ ), Kaons (K), protons (p), deuterons (d), tritium (t) and helium ( $^3\text{He}$ ) nuclei follows the typical shape of the Bethe-Bloch formula. Electrons (e) with their light mass represent a special case and cause ambiguities (crossover of black lines) in the PID even at low momentum. The colour scheme denotes the number of counts from blue (low) to red-brown (high) [22]

further particle properties such as the specific energy loss  $dE/dx$  of the particle in the working gas and its momentum  $p$  is required.

The mean energy loss ( $dE$ ) by ionisation per path length ( $dx$ ) when a charged particle passes a medium (working gas of the TPC) is well described by the *Bethe-Bloch formula*

$$-\left\langle \frac{dE}{dx} \right\rangle = K z^2 \frac{Z}{A} \frac{1}{\beta^2} \left[ \frac{1}{2} \ln \left( \frac{2m_e c^2 \beta^2 \gamma^2 T_{\max}}{I^2} \right) - \beta^2 - \frac{\delta(\beta\gamma)}{2} \right]. \quad (1.2)$$

**K**: constant, **z**: electrical charge of the passing particle, **Z**: charge number of the passed medium, **A**: atomic mass of the medium,  $m_e$ : electron mass, **c**: speed of light,  $\beta$ : velocity of the incident particle,  $\gamma$ : Lorentz factor,  $T_{\max}$ : maximal energy transfer in a single collision with a shell electron of the medium, **I**: mean excitation energy of the medium,  $\delta$ : density correction

This equation is valid in the range  $0.05 < \beta\gamma < 500$  for charged particles with a mass bigger than the muon mass ( $m > m_\mu$ ). Electrons are a special case, which cannot be described by the Bethe-Bloch formula without further corrections. Due to their small mass they can get strongly deflected when they scatter with another electron in the medium. Additionally, the incident and the target electron are indistinguishable, so quantum mechanical effects have to be taken into account.

Because of their small mass, electrons can loose energy via Bremsstrahlung, which is not considered in the Bethe-Bloch formula [23]. Apart from this exception the mean energy loss of a charged particle can be expressed in terms of  $\beta\gamma$  as demonstrated by equation 1.2. Since it is

$$\beta\gamma = \frac{p}{mc}, \quad (1.3)$$

the  $dE/dx$  depends on the particle's momentum  $p$  and its mass  $m$ . As a consequence the mass of the particle and thus its identity can be determined by a measurement of the particle's momentum and its specific energy loss in the working gas of the TPC. This is shown in the PID performance

plot of the ALICE TPC in figure 1.6. For a given momentum the energy loss is different for diverse particle species. It is also shown, that there are overlap regions (crossing of the black lines) such as the crossing of the *electron band* or in general for higher particle momenta, where the particle identification is ambiguous. There, additional PID information from the other detectors like TRD or TOF is needed to resolve these ambiguities.

Since the TPC is operated in a homogeneous magnetic field of known strength  $B = 0.5 \text{ T}$ , the tracks of the charged particles are bent in a circular way due to the Lorentz force. This curved track is then measured by the TPC and the momentum  $p$  of the particle can be determined from the track curvature  $R$  (radius of the circular track). For  $p$  in  $\text{GeV}/c$  and  $R$  in metre, it is

$$p_T = 0.3zBR \quad (1.4)$$

$$p = \frac{p_T}{\sin(\vartheta)}, \quad (1.5)$$

where  $p_T$  is the transverse momentum and  $\vartheta$  the inclination angle of the track with respect to the beampipe direction.

The specific energy loss of the charged particle traversing the TPC can be accessed by a measurement of the (primary ionisation) charge. In the case of a gas detector, which is operated in the so-called *proportional mode*, the amplified electron signal is proportional to the originally created primary ionisation charge. This is valid for gain factors (amplification factors) of about  $10^3 - 10^5$  [24]. As a matter of fact, the energy loss is then directly accessible by the number of measured ionisation clusters along the track length given that the gas properties are known.

## 2 Introduction to gas electron multipliers

A Gas Electron Multiplier (GEM) is a device for electron amplification in gas detectors. It was invented by Fabio Sauli at CERN in 1997 [25]. Before this time gas chambers, such as MWPCs or Micro-Strip Gas Counters (MSGC), were primarily used for electron amplification purposes in the according fields of application. As a matter of fact, such chambers started to show limitations especially in applications involving high charged-particle fluxes [26].

For example, the crucial point for MSGCs is the use of fragile metal electrodes, which are exposed to high electric fields in order to achieve a reasonable amplification factor (gain) around  $10^4$  for the detection of small ionisation signals. Thus, destructive discharges often happen and lead to a short lifetime for such devices. A similar problem occurs in the single electron detection with a MWPC, where also very high gains are required. Therefore, the idea of a preamplification stage came up, which makes the operation of the critical devices at much lower fields possible. Serving this purpose, the gas electron multiplier was developed.

In general a GEM is thin polymer foil, which is clad at both sides with a fine metal layer (few micrometres). As such, GEMs also involve fragile electrodes, but in contrast to the MSGCs the field geometry is more advantageous (see following section 2.1). A Kapton<sup>®</sup> polyimide film, which is an excellent electrical insulator over a wide temperature range [27], is often used as polymer foil. The standard metal is copper after a thinner layer of chromium, which makes the copper adhere to the Kapton<sup>®</sup>. Furthermore, the foil is strongly perforated with a hole density of the order of 50 – 100 holes/mm<sup>2</sup> [26]. Standard GEM foils feature a hexagonal hole pattern, which is produced by a photolithographic process and chemical etching afterwards. The degree of perforation is such that the foil is optically transparent for a human eye.

An electron microscope picture of a cross section of such a *standard* GEM foil is shown in figure 2.1. The three-layer structure of copper and Kapton<sup>®</sup> is well visible. Also the hexagonal hole pattern can be seen. In this example, the foil is 50 µm thick, while the pitch size (distance between two adjacent holes) is 140 µm. The hole diameter at the copper face is 70 µm. For a detailed overview on GEM development from their invention until today's state of the art consult [26].

### 2.1 Working principle and performance

As an electron amplification device GEM foils make use of gas amplification and are thus operated in a working gas. A potential difference of typically 300 – 400 V (working gas mixture Ar-CO<sub>2</sub> 70-30) is applied between the two metal layers. Due to the potential difference across the foil and the small dimensions of the amplification structures (hole pattern) *strong electric fields* of the order  $50 \text{ kV cm}^{-1}$  develop inside the GEM holes [28]. Figure 2.2 on the left exemplarily shows the electric field inside a single GEM hole. In this case the GEM foil is placed in between a cathode and an anode. With the appropriate potentials applied to these electrodes nearly homogeneous *drift* and *induction* or *transfer* fields are created above and below the GEM foil, respectively. In the figure, the induction field is higher than the drift field.

**Charge amplification** In such a field configuration a free electron created in the region above the GEM starts to drift towards the foil's surface. There, it is guided inside a GEM hole, where is accelerated due to the high electric field. As a consequence the electron acquires enough energy

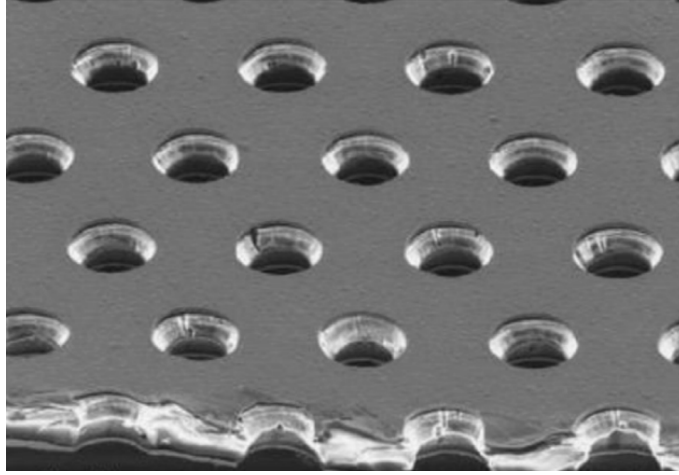


**Figure 2.1** Electron microscope picture of a small section of a standard GEM foil. It is 50  $\mu\text{m}$  thick, has a hole pitch of 140  $\mu\text{m}$  and a hole diameter of 70  $\mu\text{m}$ . It is indicated, that the hole diameter varies slightly with the hole depth [26]

to ionise gas molecules of the working gas, which is filling the entire structure. The electrons of this ionisation process are then accelerated and further ionise other gas molecules. Hence, the single incident electron is effectively amplified by an avalanche process inside the GEM hole. This *amplification by avalanche creation* in a GEM hole can be simulated by certain tools. Figure 2.2 on the right shows such a simulation of two electrons entering a GEM hole with a drift field of  $250 \text{ V cm}^{-1}$  above and a higher transfer field of  $3.75 \text{ kV cm}^{-1}$  below the GEM [28].

The paths of the electrons is depicted by light (orange) lines, while the ion trajectories are shown with dark (red) lines. Locations where gas ionisation happened are denoted by (green) dots. It can be seen that the main amplification happens in the last third of the hole depth at the bottom side and even below the GEM. Further, it is shown that a small fraction of electrons get collected at the bottom electrode of the GEM, which leads to a *electron extraction efficiency* lower than 100 %. Therefore, the *effective gain* (measurable) is always lower as the *real gain* due to efficiencies of the *electron collection* at the top electrode of the GEM and their extraction at the bottom side. Being dependent on the field configuration, the electron collection efficiency profits from a low field above the GEM, while the extraction efficiency can be enhanced by a high field below [29]. The extracted electrons from the amplification are then transferred to another amplification stage (another GEM) or are collected at an anode to obtain a signal. The possibility to stack multiple GEMs is one of their advantageous features. Often three or even four GEMs are combined in a stack to achieve effective gains of  $10^3 - 10^4$  as the product of the single foil gains. At the same time this ensures a more stable operation with a lower discharge probability due to the lower potential differences needed at each foil of the stack [26, 28].

**Signal creation** For the *signal creation* the extracted electrons from the last GEM stage before the readout anode are used directly. Therefore, the timescale of the signal creation corresponds to the drift time of the electrons from the bottom of the last GEM to the anode (few millimetres). This leads to a very fast signal compared to use the much slower ions for the signal creation as it is for example done in MWPCs. Using accordingly fast current amplifier at the anode, signals separated by about 20 ns can be distinguished. In a drift or time projection chamber this corresponds to about 1 mm multi-track resolution [26]. The needed spatial resolution can be achieved by the use of a patterned readout anode (pad plane).

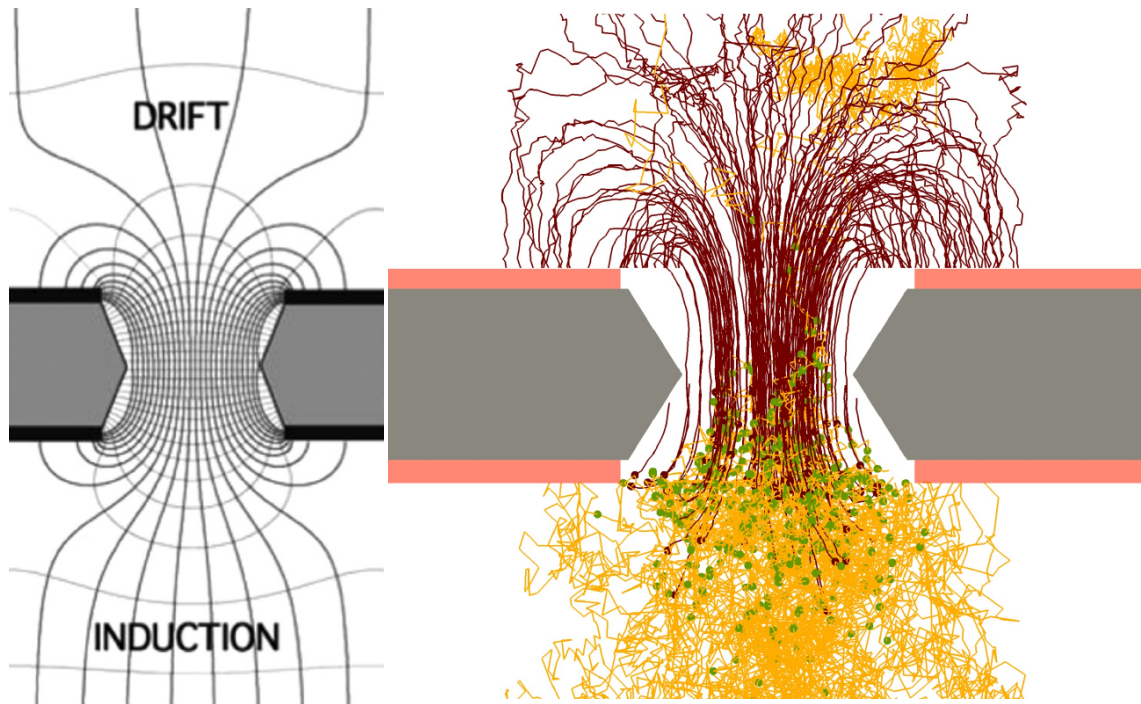


**Figure 2.2** (left) Sketch of the electrical field lines of a single GEM hole, when the foil is placed between a drift and a charge collection electrode. These electrodes together with the GEM foil itself generate the drift and induction field when set on according potentials [26]. (right) Garfield/Magboltz simulation of the impact of two incoming electrons in a GEM hole. Electron paths are shown in yellow, while ion paths are denoted in dark red. Green dots represent spots where gas ionisation happened [28]

**Ion backflow** Since the amplification process is based on the ionisation of the working gas, not only electrons, but the same amount of ions, are created. Due to their much higher mass as compared to electrons, they are less affected by diffusion [28]. Thus, they closely follow the electrical field lines on their drift back towards the top of the GEM. With an appropriate configuration of the electric fields most of them get collected at the (top) electrode, while a small fraction drifts back into the drift region. This behaviour is well described by the simulation illustrated in figure 2.2 on the right. As a matter of fact, GEMs provide intrinsic *Ion BackFlow (IBF)* blocking capabilities. This can be even optimised by the stacking of multiple GEMs and tuning of the (transfer) fields and potentials between and across the GEMs [30].

## 2.2 Different applications

GEM electrodes underwent an exhaustive research and development processes, which made them suitable for different fields of application. Nowadays, the technology is already applied or foreseen for the use in many particle physics experiments. Depending on the experiment's requirements there are highly sophisticated concepts of detectors using the GEM technology.

**GEMs in Cherenkov detectors** One example of such a concept is the use of GEM stacks for *single photoelectron detection*. In this case a GEM stack is used as an amplification device for the created photoelectrons by Cherenkov radiation for example inside a Ring Imaging Cherenkov detector (RICH). Figure 2.3 on the left illustrates the working principle of a GEM detector suitable for the detection of (Cherenkov) photons. The top metal layer of the first GEM (facing the radiator, where the Cherenkov effect happens and photons are emitted) is coated with an additional layer

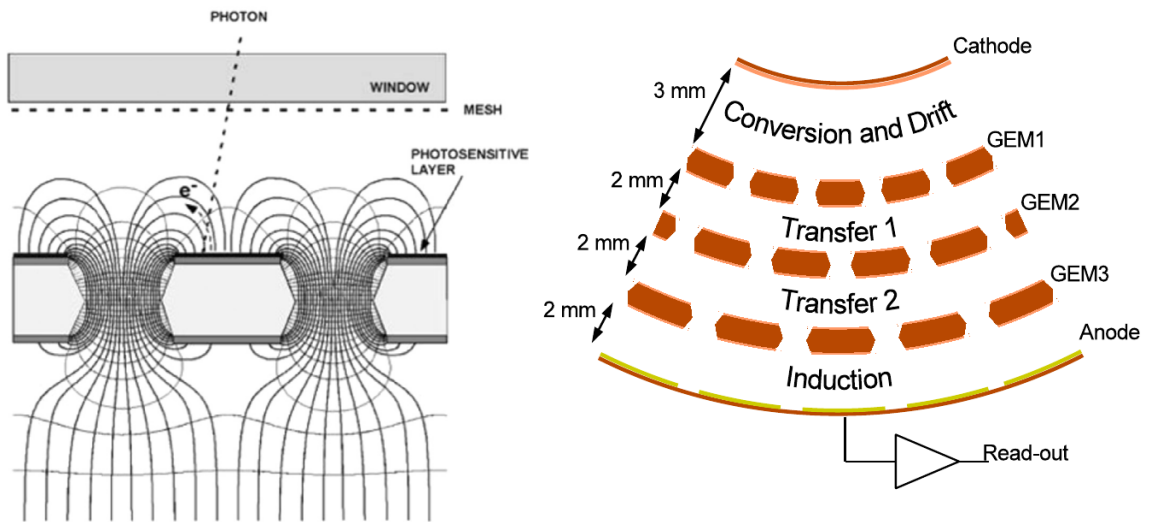


**Figure 2.3** (left) Sketch of a GEM foil for single photoelectron detection for example inside a RICH. The top metal layer is coated with an additional photosensitive layer, which serves as photocathode to convert the Cherenkov radiation into an electron signal. The mesh is for shaping the field lines to enhance the electron collection efficiency [26].  
 (right) Schematic of one of four detection layers for the new inner tracker of the KLOE-2 experiment. For the amplification of the ionisation signal from the conversion region a cylindrical GEM triple stack is used. The position resolution is provided by a segmented anode (pad plane) [32]

of photosensitive material such as Caesium-Iodide (CsI) to convert incident (Cherenkov) photons into electrons. A metal mesh above this GEM foil is used to shape the electric field such that the electron is collected by a GEM hole with high efficiency. The signal can be further amplified in subsequent GEM stages, which are made non-reactive by an additional coating (Ni or Au), to shield the copper of the GEM electrodes. Furthermore, the field configuration is optimised for low ion and photon feedback as well as low direct ionisation impact of the gas [31]. Finally, the signal is detected by a segmented anode to spatially resolve the *Cherenkov ring*.

For example, there were studies of a RICH using GEM technology for the future Electron Ion Collider (EIC). In this concept a quintuple GEM stack of  $10\text{ cm} \times 10\text{ cm}$  is directly used inside the radiator gas  $\text{CF}_4$  (windowless operation). This setup aims at the identification of charged particles with a momentum of up to  $50\text{ GeV}/c$  by measuring the ring shape of the few Cherenkov photons, which are created over a radiator length of approximately 1 m. For more details see [31].

**GEM stacks as tracking stations** An other field of application for GEMs is the *charged particle tracking*. Here, the GEMs are used to amplify the ionisation signal from charged particles traversing a short, gas filled *conversion region*. After the charged particle has left electrons from the primary ionisation of the working gas behind, they are collected by a GEM stack, which is placed in between a *cathode* and an *anode* to create the required *drift* and *induction* fields. Often stacks of three GEM foils are used. The ionisation electrons get amplified and are then absorbed by the pad plane (segmented anode) to get a signal. To achieve a reasonable position resolution the patterning of the pad plane is optimised for this task.

In figure 2.3 on the right a schematic of one of four concentric, cylindrical detection layers of the KLOE-2 (Frascati, Italy) experiment's inner tracker is shown [32]. Every of these layers involve a triple GEM stack. The unique feature of this detector is the cylindrical geometry even of the GEM foils. In general, the KLOE-2 inner tracker provides a position resolution of about  $200\text{ }\mu\text{m}$ . It has been installed in the experimental setup in 2013. More detailed information can be found in [32].

**GEMs in the ALICE TPC upgrade** Because of their intrinsic ion backflow blocking capabilities GEM stacks are predestined for the use in the *readout of TPCs*. Therefore, the decision was made to equip the ALICE TPC with GEM based readout chambers in an exhaustive TPC upgrade program. There, quadruple GEM stacks are used, which are optimised in terms of a reasonable energy resolution to do reliable particle identification. At the same time they are tuned to low ion backflow in order to keep space point distortions due to space charge accumulation in the drift volume at a manageable level. Details on the motivation and the explicit upgrade plans of the TPC are given in the following chapter 3.

## 3 The ALICE TPC upgrade

As already described in subsection 1.3.1 the ALICE TPC is currently read out by 72 MWPCs, which are operated with a gating grid. This will be changed during the ALICE TPC Upgrade (TPCU), because then the exchange of the current readout chambers by new GEM based readout chambers is foreseen. The procedure is planned for the Long Shutdown 2 (LS2) starting in December 2018, when the LHC stops operation for roughly two years. At this time the entire TPC is taken out of the L3 magnet and brought to the surface. There, the chambers are exchanged one-by-one in a cleanroom-like environment. After that, the TPC with its new readout chambers is reinserted into the magnet and mounted at its former place again.

### 3.1 Motivation

After the Long Shutdown 2 the so-called LHC Run 3 starts in 2021. There, the *luminosity* of the accelerator chain will be increased and the LHC will then provide Pb-Pb collisions with rates up to 50 kHz. This gives rise to an integrated luminosity of  $\mathcal{L}_{\text{int}} = 10 \text{ nb}^{-1}$ .

In this context, inverse femtobarn ( $\text{fb}^{-1}$ ) is the typical unit to measure particle-collision events per (geometrical) cross section (measured in  $\text{fb} \equiv 10^{-39} \text{ cm}^2$ ). Thus, it is a measure of the total number of events and the corresponding amount of data collected summed over a certain period of time per femtobarn of target cross section. For example  $1 \text{ fb}^{-1}$  is equivalent to approximately  $10^{12}$  pp collisions [33].

The previous lead-ion campaigns during the LHC Runs 1 and 2, lasting from 2015 to 2018, will conclude the initial LHC heavy-ion programme and give way to the high-luminosity operation in Run 3. Compared to the  $\mathcal{L}_{\text{int}} = 1 \text{ nb}^{-1}$  delivered by the end of Run 2, the integrated luminosity will increase by a factor 10. This leads to a massive enhancement of the sensitivity to rare hard probes especially at low transverse momentum ( $p_T$ ), which are exemplarily described in subsection 1.1.2. ALICE plans to record an as large as possible sample of events in Pb-Pb collisions, as they provide the opportunity to investigate the strongly interacting matter at high temperatures, such as the QGP. Performing these measurements requires the examination of every event delivered at the high luminosity during Run 3 in order to profit from the resulting enhanced statistics [21, 34].

The TPC is readout by MWPCs, which are operated in a gated mode in order to suppress the back flowing ions from the gas amplification process (cf. subsection 1.3.1). During the maximum electron drift time in the TPC of about  $100 \mu\text{s}$ , the gating grid (GG) is open in order to collect all electrons from the current event. Afterwards it closes for about  $180 \mu\text{s}$ . This time is needed to efficiently collect and neutralise the slow drifting amplification ions (compared to electrons). As a result, the current TPC readout has an effective dead time of the order  $280 \mu\text{s}$ . The current TPC is thus limited to a maximal readout rate of about 3.5 kHz. However, in central Pb-Pb collisions it is only read out at approximately 300 Hz [21].

These restrictions due to the gated operation of the MWPCs match well with the conditions in Run 1 and Run 2. However, the situation will be completely different for the future Run 3. There, the maximum electron drift time in the TPC of  $100 \mu\text{s}$  in combination with the the increased interaction rate, which results in  $20 \mu\text{s}$  time between the events, leads to an event pileup (tracks from different events, which overlap in the drift volume of the TPC) in the TPC of 5. In the case of a gated readout operation, this would lead to a huge amount of inaccessible events and

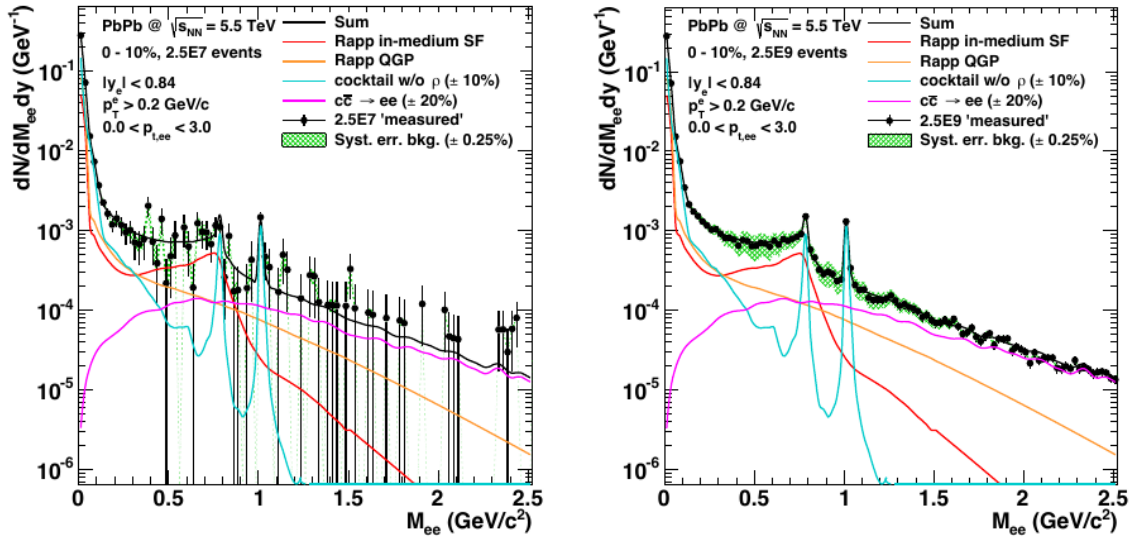


**Figure 3.1** Simulations of inclusive  $e^+e^-$  invariant mass spectra for the current (left) and an upgraded TPC (right) [21]. The plots show  $2.5 \times 10^7$  and  $2.5 \times 10^9$  events for the respective two cases for the most central Pb-Pb collisions at  $\sqrt{s_{NN}} = 5.5$  TeV (centrality class 0 - 10 %). Different contributions to the spectra are shown as coloured lines: light hadrons (blue), charm decays (magenta), thermal radiation from hadronic gas (red) and from QGP (orange). An increase in the readout rate in the upgrade case is crucial

therefore an unacceptable loss of possible data. As a consequence, the TPC has to be operated in a continuous readout mode in Run 3.

As an example of the benefits for the upgraded TPC, figure 3.1 shows the inclusive electron-positron ( $e^+e^-$ ) invariant mass spectrum for the current (left) and an upgraded version of the TPC (right), which can be obtained from the data of a typical yearly heavy-ion run. An upgrade of the TPC would increase the readout rate by about two orders of magnitude and thus provide higher statistics. It is clearly visible that the statistical uncertainties are significantly reduced in the upgrade scenario, which leads to a more precise spectrum.

The most naive approach is to simply operate the MWPCs in an ungated mode, i.e. with an entirely open gating grid. In this scenario the ions, which are produced during the gas amplification of the signal, drift back and accumulate in the drift volume of the TPC. There, these *space charges* modify the drift field and thus the ionisation electrons are deflected. The resulting space point distortions (see subsection 1.3.1) have to be accounted for in the data processing. During a dedicated period of time this was tested in pp collisions with an interaction rate of 200 kHz. It was found that massive distortions arise, which are strongly fluctuating in time. The higher luminosity in Run 3 would further contribute to this problem. For this reason, they cannot be corrected (with sufficient resolution) by data processing methods. As a consequence, the MWPCs are not suitable for the high-rate operation during Run 3. For more details on this study and space point distortion calibration in the TPC in general see [35].

On these grounds a new readout system is required, which offers a continuous readout and is capable of a stable high-rate operation. Furthermore, intrinsic blocking of ion backflow, in order to keep the space charge induced space point distortions on a manageable level, is necessary. At the same time the performance of the current TPC in terms of position and energy resolution should be maintained.

All these constraints and requirements are approached with new readout chambers, which are based on GEM technology. Studies of prototype  $10 \text{ cm} \times 10 \text{ cm}$  detectors as well as studies with prototypes of the size of a readout chamber proved that quadruple GEM stacks can provide a comparable performance as compared to the current MWPCs. At the same time, they feature a

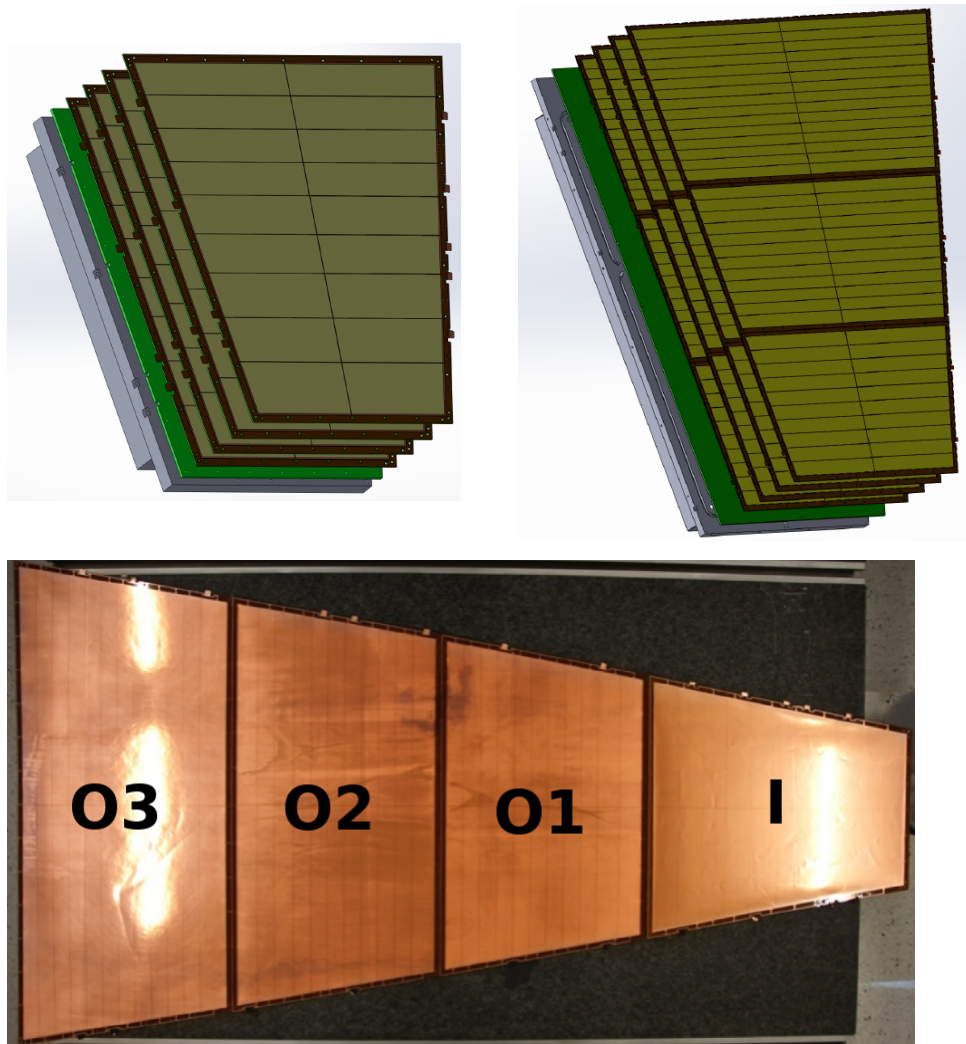


**Figure 3.2** (top) Schematic, exploded view of the GEM readout chamber design for IROCs (left) and OROCs (right). From rear to the front the alubody (grey), the glass fibre strong back, which holds the pad plane (green) and the stacks of four GEM foils each can be seen [21]. (bottom) Photograph of GEM foils in four different sizes which are used in stacks to cover one full trapezoidal sector of the ALICE TPC. Three diverse foil sizes (O1, O2 and O3) are applied within an OROC, while an IROC has only one stack of one foil size (I) [34]

sufficiently low ion backflow. More detailed upgrade plans are presented in the following sections 3.2 and 3.3.

### 3.2 Readout chamber design

Most of the components of the TPC are reused in the upgrade, because it is foreseen to exchange only the current readout chambers by the new GEM based ones. For example the gas system, the inner and outer field cage, the central electrode and the entire supporting structure stays the same. However, the GEM based readout chambers are newly built from scratch. In general, there are inner (IROC) and outer readout chambers (OROC). In total, this requires at least 36 new OROCs and 36 new IROCs to be built for the 18 sectors of each side of the ALICE TPC.

At the top of figure 3.2, schematics of the GEM based IROC (left) and OROC (right) designs can be seen. Both of them have a so-called *alubody* (grey), which supports the further components of the readout chamber. The ready chamber is attached to the supporting structure by this rigid

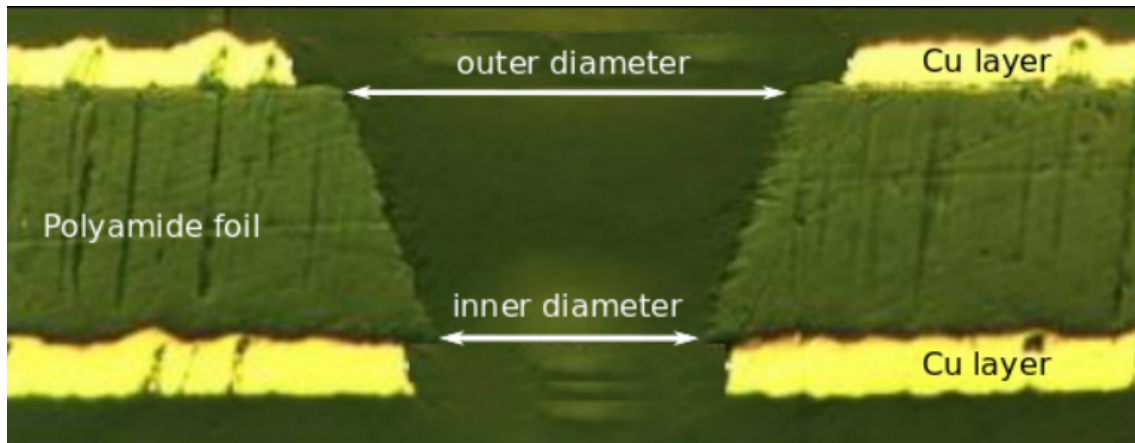


**Figure 3.3** Cross section through a GEM hole, which was produced by a single-mask technique. Due to the conical hole shape an inner and an outer hole diameter can be defined [36]

aluminium part. Furthermore, the readout electronics are mounted there. On top of the alubody, there is a glass fibre strong back (green), which holds the copper pad plane. The *quadruple GEM stacks* are mounted upon the pad plane.

Since it is technically not possible to produce large enough GEM foils to cover the entire OROC area, it is subdivided into three GEM stacks with different foil sizes. Therefore the sizes of the foils in the different stacks are denoted by the readout chamber type and the stack position inside the respective chamber. Innermost, there are the IROC foils (I), which are the smallest foils involved. They cover an area of about  $1678 \text{ cm}^2$ . Towards bigger radii the OROC 1 (O1), OROC 2 (O2) and OROC 3 (O3) foils follow. With an area of about  $2949 \text{ cm}^2$ , the O3 foils are the largest GEM foils involved in the upgrade. The four differently sized GEM foils are shown at the bottom of figure 3.2. There, they are exemplarily arranged in the same way as they will cover the trapezoidal area of one ALICE TPC sector, when they are mounted on the readout chambers.

### 3.3 Design and characteristics of the GEM foils

Due to the demanding conditions in Run 3, the GEM based readout chambers, and thus the individual GEM stacks, have to fulfil special requirements concerning the ion backflow properties and the energy resolution. In order to successfully operate the new readout chambers at high particle rates and in continuous readout mode, a value of the ion backflow of 1 % or below is needed. It is defined as

$$\text{IBF} = \frac{1 + \epsilon}{G_{\text{eff}}}, \quad (3.1)$$

where  $G_{\text{eff}}$  is the effective gain of the GEM stack and  $\epsilon$  is the total number of ions drifting back into the gas volume per incoming electron. To achieve a sufficient signal-to-noise ratio of about 20, the effective gain of a GEM stack has to be 2000 in the baseline gas mixture Ne-CO<sub>2</sub>-N<sub>2</sub> (90-10-5) [21]. Thus, an IBF of 1 % corresponds to  $\epsilon = 20$  back flowing ions per incoming electron.

In an extensive research and development programme (cf. end of section 3.1), which started in 2012, it was found that the required performance is accomplished by a quadruple GEM stack of special geometry. The involved GEM foils are  $50 \mu\text{m}$  thick Kapton<sup>®</sup> polyimide foils clad with a  $2 - 5 \mu\text{m}$  fine copper layer on both sides. The hexagonal hole pattern is produced by a lithographic process in a so-called *single mask technique* and chemical etching of the pattern afterwards. This leads to a conical hole shape, as it is illustrated in figure 3.3. Therefore, an inner ( $\sim 50 \mu\text{m}$ ) and an outer hole diameter ( $\sim 70 \mu\text{m}$ ) can be defined and measured by an optical method (see subsection 5.5.1).

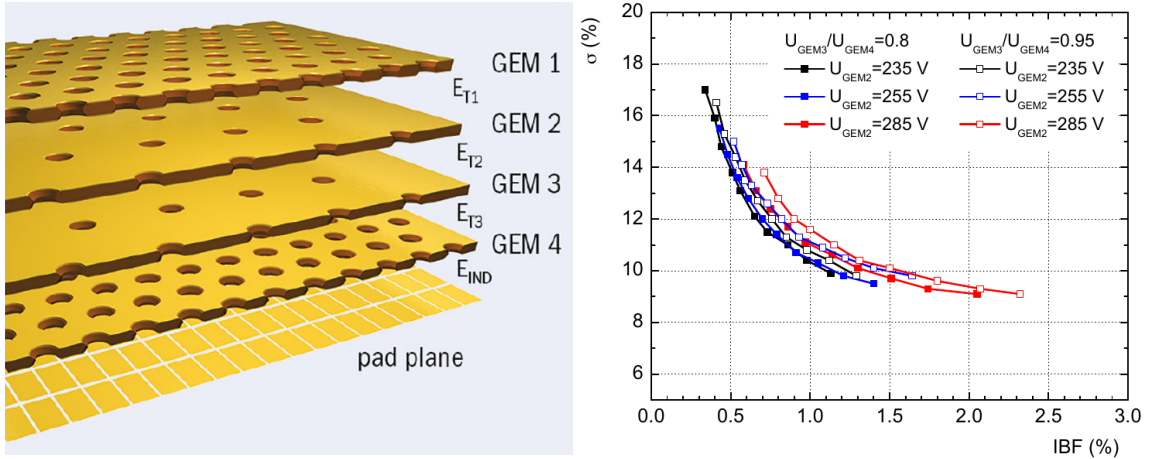


**Figure 3.4** (left) Schematic of the GEM stack design for the ALICE TPC upgrade. Two foils with doubled pitch size are mounted between two standard pitch foils. The transfer fields are denoted by  $E_i$ ,  $i = T1, T2, T3, IND$ . The picture is not to scale [37].

(right) Correlation of the IBF and the energy resolution at 5.9 keV of the left GEM configuration for different voltage settings of the single GEMs. From left to right, the potential difference across GEM 1 varies between 225 and 315 V. Different settings of the potential difference across GEM 2 are shown. The potentials at GEM 3 and GEM 4 are adjusted such that an effective gain of  $G_{\text{eff}} = 2000$  is achieved [21]

Figure 3.4 on the left schematically shows the GEM stack design of the ALICE TPC upgrade. Between two GEM foils (GEM 1 and GEM 4) with a *standard pitch* (SP) of  $140 \mu\text{m}$  (distance between two adjacent holes), there are two foils with a *large pitch* (LP) of  $280 \mu\text{m}$ . This special geometry helps to decrease the ion backflow. In contrast to electrons, Ions are more likely to follow the electric field lines and thus to end up at a GEM electrode, where they are neutralised. This behaviour is caused by their larger mass and hence lower diffusion as compared to the electrons. For this reason, the arrangement of the GEM foils in the upgrade follows the pattern SP-LP-LP-SP. To further benefit from this effect, the hole pattern of the first (GEM 1) and the third (GEM 3) is rotated by  $90^\circ$  in order to ensure an uniform misalignment of the holes from the different GEMs.

The main ingredient to reduce the IBF is the optimisation of the voltage settings and transfer fields between the GEMs. However, these also has an influence on the energy resolution, since the electron collection and extraction efficiency is accordingly modified when changing the fields between the GEMs. Unfortunately, a low ion backflow and a low energy resolution are competing factors as it is shown in figure 3.4 on the right. The reference for the  $dE/dx$  resolution is the energy resolution of the  $^{55}\text{Fe}$  ( $\gamma$ -source) photo peak at 5.9 keV. There, the requirement is a value of  $\sigma(^{55}\text{Fe}) = 12\%$  or below. The correlation plot in figure 3.4 (left) shows that it is possible to meet both requirements (IBF and energy resolution) with convenient voltage settings.

Ideally the GEM foils in the stack are stable when the voltages are applied. However, discharges between the foil electrodes or even between the different foils inside one stack can occur and have to be taken into account. In order to mitigate the impact of possible discharges (and short circuits) the top electrode of the GEM foils is segmented, which can be seen in the figures 3.5 and 5.3. For example it has been shown that the energy of the discharge and thus its destructive potential is significantly reduced by reducing the capacitance between the two metal layers of a GEM foil [38]. Each of the segments roughly has an area of about  $100 \text{ cm}^2$  and can be connected to a high voltage (HV) power supply via a common HV path and loading resistors of  $R_L = 5 \text{ M}\Omega$  [21]. The number of the segments for each foil size is summarised in table 3.1, while their numbering scheme is depicted in figure 3.5 using the example of an OROC 3 foil. Moreover, the bottom side

segment 0	1
2	3
4	5
6	7
8	9
10	11
12	13
14	15
16	17
18	19
20	21
22	23

**Figure 3.5** Numbering scheme of the 24 segments of an OROC 3 GEM foil. The segments of the smaller foils are numbered in an according way [36]

Foil size	# segments
IROC (I)	18
OROC 1 (O1)	20
OROC 2 (O2)	22
OROC 3 (O3)	24

**Table 3.1** Number of segments for each GEM foil size

of the GEM foils is not segmented and thus can be directly connected to a power supply. For more detailed information on the connection of the single GEM segments see section 4.2.

The GEM foils for the upgrade are produced as large rectangular foils with the embedded trapezoidal structure of the active area. Every foil can be identified by its unique serial number of the type O3-G1-001 (OROC 3, GEM 1, foil number 001). For handling and stretching purposes as well as to stabilise the entire foil, they are put into a surrounding *optiguard* (aluminium) frame. Some photographs of such foils with the optiguard frame can be seen in figure 4.2. Before being mounted on a chamber, the active part, which is illustrated in figure 3.2 (bottom) for each foil size, has to be cut out.

### 3.4 TPCU workflow and quality assurance

In order to guarantee the success of the ALICE TPC upgrade and to stay on operating schedule 38 institutes from America and Europe are involved. Furthermore, an extensive quality assurance (QA) programme for the different detector components is followed. An overview of the working flow for the TPC upgrade is shown in figure 3.6. Only the key stations for the GEM foils, which are relevant for the scope of this thesis, are described in the following.

All GEM foils are produced in the Printed Circuit Board (PCB) workshop at CERN. There, their electrical properties are immediately tested with the so-called *leakage current test* (see chapter 4 for more details). If they pass the test, they are either sent to the Helsinki Institute of Physics, Finland, or the Wigner Research Center for Physics in Budapest, Hungary, where the foils are inspected with an optical method in order to detect mechanical and etching defects of the foils. Additionally, the hole diameters are measured and checked for uniformity. Furthermore, long-term leakage current test is performed before the foils of different sizes are sent to the according institutes.

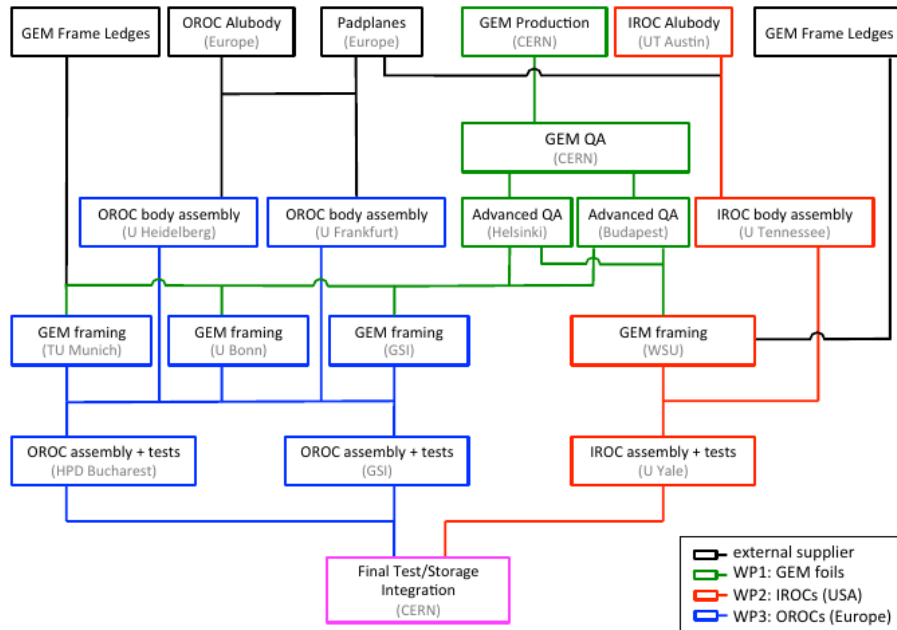


**Figure 3.6** Sketch of the workflow concerning the different components in the ALICE TPC upgrade. The colours denote different working processes. For example the GEM production and their QA shown with green lines. Additionally, the involved institutes are shown [39]

The complete IROC production takes place in America. As a first step, the corresponding IROC foils are sent to the Wayne State University (WSU), Detroit, USA. In parallel, the OROC production takes place in Europe. In Germany, the O1, O2 and O3 foils are taken care of by the Technical University of Munich (TUM), the University of Bonn and the GSI Helmholtz Center for Heavy Ion Research, Darmstadt, respectively. At these *framing institutes*, the foils undergo the leakage current test twice, before and after they are stretched and glued to an appropriate glass fibre frame surrounding the active area in order to enhance their mechanical sturdiness. Moreover, this frame is necessary to mount the foils into a stack.

Finally, the foils are shipped to the institutes, where the the final readout chambers are built and tested. For the IROC foils this is Yale University, USA, while for the OROC foils there is the National Institute for Physics and Nuclear Engineering, Bucharest, Romania, and GSI, which contributes as a framing and a chamber building institute. Before the foils are stacked on the chambers, they have to pass the leakage current test (after their transport) again. At this point, the foils are ready to be *trimmed*. Carefully cutting along the outer edges of the glass fibre frame, only the trapezoidal active area remains, which is then mounted on top of the pad plane.

The ready and tested chambers are then sent to CERN, where they are stored inside special transportation boxes under controlled conditions until they are finally installed in the TPC. For a detailed overview of the different QA steps of the GEM foils consult [39].

## 4 The leakage current test

The proper selection of the GEM foils, which are finally assembled in the new readout chambers of the ALICE TPC, is crucial in order to assure their stable and uniform operation in the demanding conditions during LHC Run 3. Therefore, an extensive quality assurance (QA) and characterisation programme of the GEM foils is followed. A key aspect is the *electrical characterisation of the GEM foils*, when a potential difference is applied across the foil. In consideration of this fact, the foils are tested with the leakage current test after every major production step as it is already described in section 3.4.

The basic idea of the leakage current test is to apply a high potential difference of  $U_{HV} = 500$  V to each of the foil segments. This nominal value is chosen such that it is marginally below the breakdown voltage (voltage at which continuous, destructive discharges occur) of the GEM foils in a dry nitrogen atmosphere. After the foil has charged up, comparable to the charging of a plate capacitor, the current through the segments saturates to a certain value, the *leakage current*. During the entire measurement the current is recorded over at least 1000 s by a sensitive amperemeter (picoampere scale). Moreover, it is checked in terms of its overall level and possible discharges, where the current suddenly rises by several orders of magnitude for a very short time.

In order to ensure the stable operation of the GEM foils in their final application, it has been found that a value of the leakage current per foil segment of less than  $I_{\text{limit}} = 0.5$  nA in a dry nitrogen atmosphere is sufficient as a quality measure. Additionally, the foil should behave stable during the entire measurement time. In the ideal case, there should not be any discharges at all. However, rare, individual discharges can be tolerated during an otherwise stable operation. If these requirements are not met, i.e. the leakage current level of one segment is above 0.5 nA or discharges occur repeatedly or even continuously, the GEM foil fails the leakage current test and is sent back to the CERN workshop. There, it is tried to recover the foil by a re-cleaning process. In the case of successful recovery the foil undergoes all the QA steps again. Otherwise, it is permanently rejected from the use in the TPC upgrade.

In the following sections the testing equipment (section 4.1), the experimental setup (section 4.2) and the measuring procedure (section 4.3) of the leakage current test is described. Since the leakage current test is a standardised routine in the QA programme of the GEM foils, it is basically the same at every measuring institute. Thus, within the scope of this thesis it is described using the example of GSI.

### 4.1 Testing equipment

To perform the leakage current test some specialised equipment is used. The major experimental components are described in the following.

**Cleanroom** To protect the GEM foils from dust and other environmental influences, they are stored, handled and tested inside a cleanroom. There, environmental parameters such as temperature and humidity are permanently controlled. Furthermore, the amount and size of dust particles in the air is extremely reduced by continuous air circulation and filters. To keep these conditions special clothing, such as a hairnet (and beard protection if applicable), a special cleanroom overall and cleanroom shoes, have to be put on inside an air lock before entering the

cleanroom. Exemplary, the blue cleanroom overalls and white, antistatic shoes used in GSI's cleanroom can be seen in the figures 4.2b and 4.2c.

**Test drawer** A (test) *drawer* is a structure to electrically contact the GEM foil in an easy, efficient and safe way. It consists of two acrylic glass plates, which measure approximately  $120\text{ cm} \times 80\text{ cm}$ . They are held together at the edges by multiple (black) screws and spacers at a small distance (ca 2 cm) from each other. The bottom plate has a trapezoidal cutout with the dimensions of the active area of a GEM foil. As a consequence, a separate drawer for each foil size is available. A photograph of a drawer bottom plate with the spacers for an O3 foil is shown in figure 4.2d. The closed drawer is shown in figure 4.2g.

A GEM foil can be placed on the bottom plate of the drawer and is held in position by its aluminium *optiguard frame* at the very edges of the foil, which perfectly fits into notches on the bottom plate. Another notch is milled at the edge of the cutout in order to compensate the height of the (trapezoidal) glass fibre frame surrounding the active area (see section 3.4). In case on an unframed foil the notch can be padded up with a dedicated plastic dummy frame. The notches in the drawer bottom plate for the supporting, rectangular (silver) optiguard frame and the trapezoidal glass fibre frame can be seen in figure 4.2d.

At the inner side of the cover plate there are metallic pins, which can vary their height due to spring suspension. They precisely establish an electrical connection to each of the foil segments (for the leakage current measurement) and to the HV path to power the foil. Spacers prevent the cover plate from touching the GEM surface. Another pin contacts a copper plate, which is used to connect the unsegmented bottom electrode of the GEM foil with ground. Each of these pins are connected to a corresponding spring pin at one of the long edges of the drawer. These, are used to connect the drawer to the *test box*. Figure 4.2g and 4.2i show the cover plate of the drawer with the golden metal pins and wires electrically connecting the foil to the drawer.

**Test box** Since the leakage current test has to be performed in a dry nitrogen atmosphere, a test box is needed to control the required environmental parameters. It is a gas tight acrylic glass box with a removable lid in order to insert or remove the drawer. Furthermore, there is a gas supply at one of the short sides of the box to flush it with dry nitrogen gas. A gas outlet through a long hose is placed at the opposite side of the box to avoid large overpressure and backflow of the surrounding air into the test box. A photograph of the closed test box with the attached nitrogen gas supply (blue hose on the right face) and an inserted drawer is depicted in figure 4.2j.

Inside the test box at one of the long box walls there are multiple contact faces to establish an electrical connection with the spring pins of the drawer. Each of these faces connects to one of 26 coaxial cable plug sockets on the outside of the test box. There are 24 sockets, which are connected to the amperemeter (underneath the table) for the current measurement of each foil segment by (red) coaxial cables as shown in figure 4.2j. Additionally, there is one socket for the HV and ground connection and one spare.

**Amperemeter** To measure the small leakage currents a very sensitive amperemeter is required. Therefore, a 24 channel amperemeter with a resolution of  $0.1\text{ pA}^1$  is used for the current measurement of each foil segment. This amperemeter is often referred to as *picoammeter*. The measurement values are read out and displayed by a computer via a LabVIEW™ (see [40]) program. Figure 4.2l shows the control panel of this application. The averaged values over one second measurement time for each segment are written and stored in a simple text file.

<sup>1</sup>The manufacturer's specification of the measurement accuracy of the picoammeter is  $0.1\text{ pA}$  to  $0.2\%$  at  $23\text{ }^\circ\text{C}$

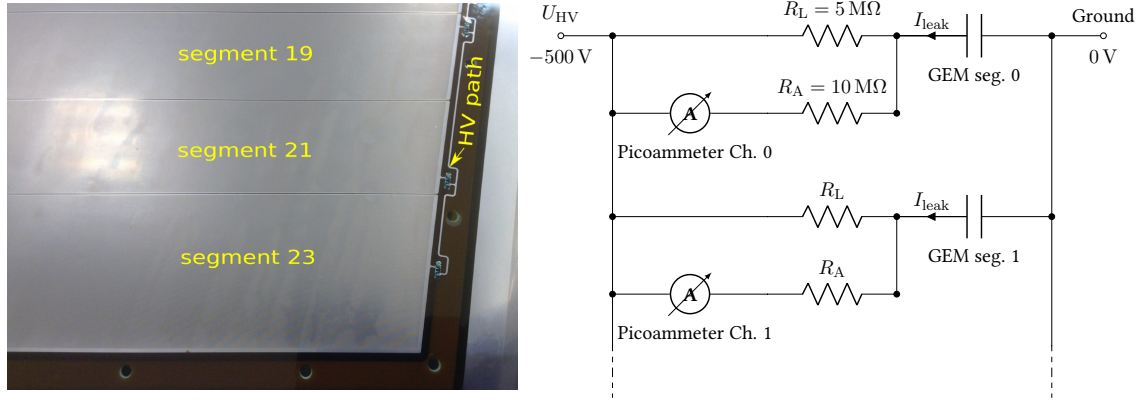


**Figure 4.1** (left) Closeup of the segmented side of an O3 foil. Three of the 24 segments are partly visible. On the right, adjacent to the active area the HV path (thin copper line), which connects the single foil segments via the loading resistors to the HV source, can be seen. The glass fibre frame, which is glued to the foils, shines through the (brown) Kapton® band [36]. (right) Wiring diagram of the leakage current test. The GEM foil segments are represented by plate capacitors. Additionally, the loading resistors  $R_L$  and the internal resistance of the picoammeter  $R_A$  is shown. Adopted from [41]

**HV source** To power the GEM foil during the test an *iseg* high voltage power supply is used. It provides the required *negative* voltage of  $U_{HV} = -500$  V and can be regulated by the same LabVIEW™ application, which reads out the picoammeter.

## 4.2 Experimental setup

A photograph of the entire experimental setup for the leakage current test in GSI’s cleanroom is shown in figure 4.2j. There, all the different components described in the previous section 4.1, except for the high voltage power supply can be seen.

For the leakage current test a potential difference of 500 V is applied across every segment of the GEM foil. This is realised by a single HV connection from the power supply to the HV path on the foil, which then delivers the applied voltage via 5 MΩ loading resistors to each segment. The photograph in figure 4.1 on the left exemplarily shows a closeup of the segmented side of an O3 GEM foil. Adjacent to the active area (the segments) the HV path, a thin copper line, as well as the loading resistors between the HV path and the segments can be seen.

For the current measurement each segment is additionally contacted by the drawer pins. Thus, an electrical connection between them and the picoammeter is established via the drawer and the test box connection systems (see section 4.1). An equivalent circuit diagram of the test setup is depicted in figure 4.1 on the right. Each GEM foil segment can be represented by a plate capacitor with a capacitance of  $C_{\text{seg}} \approx 5$  nF [21].

As they are no ideal capacitors a small leakage current  $I_{\text{leak}}$ , which flows through them, exists. It is measured by the picoammeter in parallel connection to the loading resistors. Since each channel of the picoammeter provides an internal resistance of  $R_A = 10$  MΩ, the leakage current splits between the two resistors. According to *Kirchhoff’s circuit laws* the measured current is smaller than the real leakage current through the segments by a factor

$$I_{\text{meas}} = \frac{R_L}{R_L + R_A} = \frac{1}{3}. \quad (4.1)$$

As a consequence, the leakage current limit of 0.5 nA/segment corresponds to a measured value of approximately  $I_{\text{limit, meas}} \approx 0.17$  nA/segment. In the following the term *leakage current* is used to describe the *measured* current values.

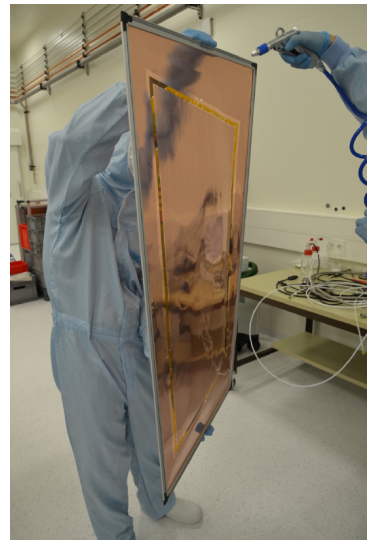
## 4.3 Testing procedure



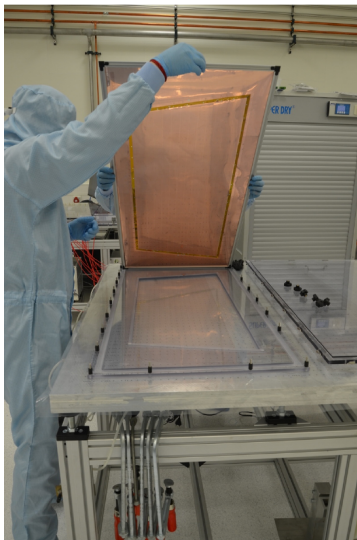
(a) GEM foils stored inside paper bags in a dry cabinet



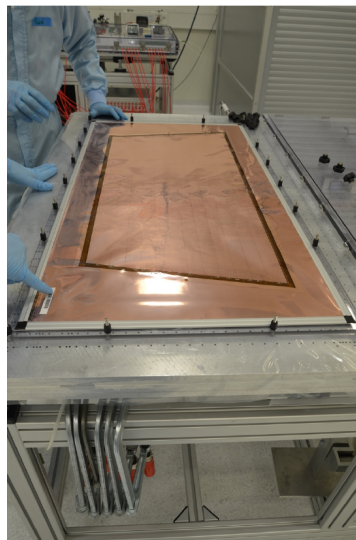
(b) Unpacking of a GEM foil from a paper bag



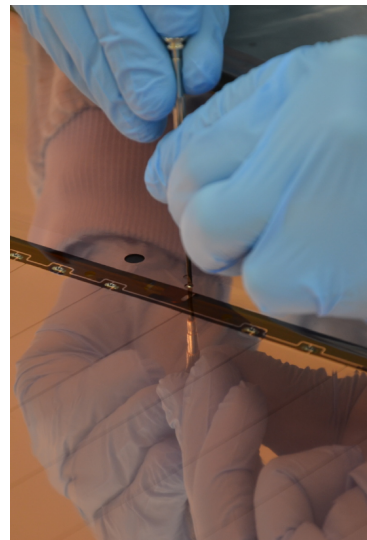
(c) Blowing potential dust off the foil with compressed nitrogen



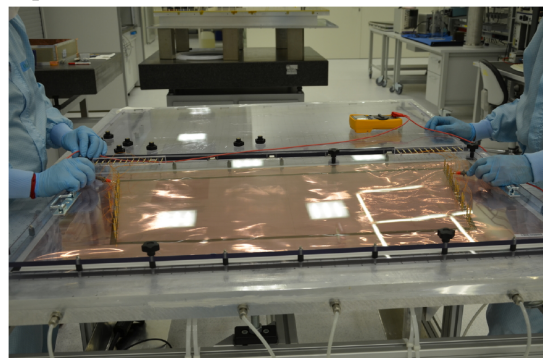
(d) Placing a foil on the bottom plate of the drawer



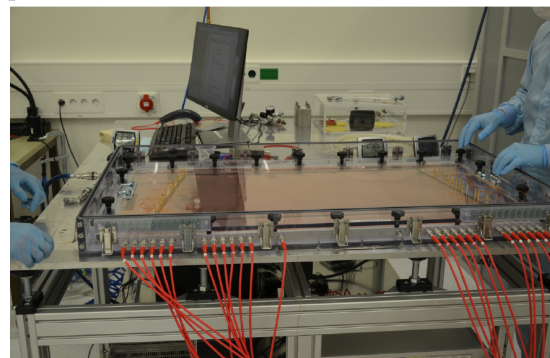
(e) GEM foil correctly placed in the drawer bottom plate



(f) Establishing electrical connection to the bottom of a GEM foil



(g) GEM foil connected to the drawer by the cover plate pins. Connectivity check with a multimeter

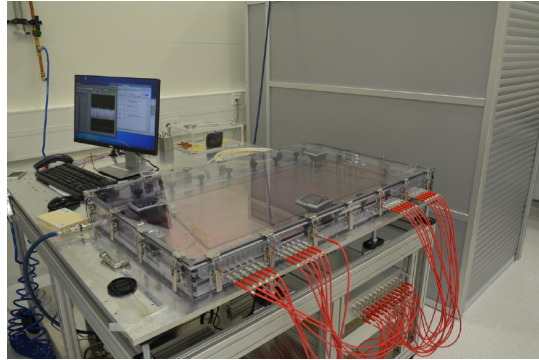


(h) Closed drawer inserted in the test box

## 4 The leakage current test



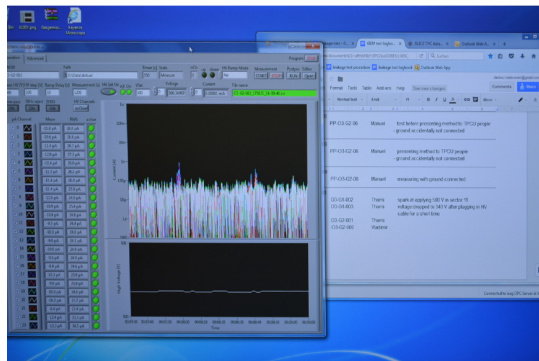
(i) Establishing connection from the *ground pin* to the test box



(j) Closed test box with the nitrogen gas supply (blue hose) attached



(k) One of three hygrometers in the test box to verify the required measurement conditions



(l) LabVIEW™ panel with live display of the measured current values of 24 segments and test logbook

**Figure 4.2** Photographs of the main steps in the leakage current testing procedure using the example of an O3 foil [41]

In the following the entire testing procedure including all the main steps as well as the preparation is described using the example of GSI. Furthermore, it is illustrated by photographs which present snapshots of the main work steps of the leakage current testing scheme.

**Preparation and requirements** Since the leakage current test is performed in a cleanroom the appropriate (antistatic) clothing such as a cleanroom overall and special shoes has to be worn (see section 4.1 paragraph *Cleanroom*). In addition to that, rubber gloves and a protective face mask, which covers the mouth and nose, are mandatory when handling the GEM foils. This is necessary, because GEMs as micro-pattern gas detectors are very susceptible to dust and other surface contamination, which can lead to a higher discharge probability when the high potential difference is applied across the foil. In general, two persons are required to perform the leakage current test.

For the preparation and the GEM handling at least one free table is necessary. In order to protect the GEM foils from surface contamination, the table surface is cleaned with isopropanol and a lint free cloth. Also the drawer has to be cleaned properly with the same means, before inserting a foil. Moreover, it is found that detaching and attaching the drawer screws produces tiny metal splinters, which possibly cause permanent short circuits during the leakage current test when they get into a GEM hole. To account for this problem, the screws are detached and cleaned in an isopropanol ultrasonic bath at the beginning of each measurement series.

**GEM storage and handling** To protect the GEM foils from humidity, which is another factor that increases a foil's discharge probability, they are stored inside a special *dry cabinet*, which

offers an environment of approximately 0% relative air humidity. Additionally, the foils are packed in *paper bags*, which are usually used to store photographic films, so as to protect them from other environmental influences. Figure 4.2a shows an opened dry cabinet with GEM foils wrapped in white paper bags inside.

For getting tested, the respective foil is taken out of its paper bag as illustrated in figure 4.2b. In general, the foils are handled by solely holding them at the supporting optiguard (aluminium) frame without touching their sensitive copper surface.

To ensure that the foil is dust free, it is cleaned by blowing at it with compressed nitrogen gas from both sides. Thus, potential dust particles are simply blown off. A picture of this cleaning process can be seen in figure 4.2c.

**Placing the GEM foil in the drawer** The cleaned GEM foil is then placed on the bottom plate of the opened drawer in a way which is illustrated on the photograph in figure 4.2d. The optiguard frame fits perfectly in the foreseen notch and thus holds the foil in position. Due to the cutout, the active area of the GEM foil is not touching the acrylic glass structure of the drawer.

Figure 4.2e shows a correctly placed foil. Every foil has a bar code label (bottom left), which references the exact foil type by a serial number of the type O3-G1-001 (OROC 3, GEM 1, foil number 1). At the very edge of the optiguard frame the black spacers, which prevent the cover plate from touching the foil can be seen.

**Establishing electrical connection and connectivity check** The next step is to establish the electrical connections between the GEM foil and the drawer pins. In order to connect the unsegmented bottom electrode of the GEM to the ground potential, a small copper plate is used. As illustrated in figure 4.2f the plate is thus turned underneath a copper flap at the rim of the active area using a screwdriver. The plate itself can be contacted by a *drawer pin* through a small hole outside of the active area.

At this point the drawer is closed with the cover plate and the black screws. Hence, the golden spring pins are now contacting each segment at the solder after the loading resistor (see figure 4.1) for the leakage current measurement. Additionally, there are two more pins that connect to the HV path and the copper plate for the ground connection. A photograph of the closed drawer with an O3 foil inserted is shown in figure 4.2g. Also the corresponding spring pins (in the following referred to as *outer drawer pins*) at the rear long edge of the drawer cover plate, which are individually connected by thin wires to the pins that contact the foil, can be seen.

To verify the correct electrical connection of the foil to the drawer, a connectivity check as also depicted in figure 4.2g is performed. First, the resistance between the HV pin and the outer drawer pins is measured with a multimeter. To ensure a good electrical contact to the foil, a resistance around the design value  $R_L = 5 \text{ M}\Omega$  should be determined for every segment. Subsequently, the total capacitance of the GEM foil is measured between the HV pin and the ground pin in order to verify a correct ground connection. If this connection is bad or even missing the observed capacitance is lower by at least one order of magnitude compared to the nominal value. Since at GSI only OROC foils are tested, table 4.1 only summarises the nominal capacitance of the respective foils.

**Inserting the drawer into the test box** If all electrical connections are tested to be good, the drawer is inserted into the test box. Figure 4.2h shows the open test box with the inserted drawer.

The outer drawer pins now connect to the corresponding contact faces inside the test box, while they are further connected with the picoammeter underneath the testing table via the red coaxial cables. Additionally, the HV pin and the ground pin have to be manually connected to their respective links by wires with crocodile clips. This action is shown in figure 4.2i. These

Foil size	Pitch	Total capacitance (nF)
OROC 1 (O1)	SP	79
	LP	91
OROC 2 (O2)	SP	104
	LP	119
OROC 3 (O3)	SP	131
	LP	151

**Table 4.1** Rough nominal capacitance of OROC GEM foils, which are used in order to check the ground connection from the foil to the drawer

links are both connected to a single coaxial cable, which is plugged into the HV power supply via the picoammeter.

To monitor the relative air humidity inside the test box, three digital hygrometers are placed at representative points. They must not be above the active area due to their possible influence on the leakage current measurement. At this point the test box is closed and the nitrogen gas supply (blue hose) is attached. A photograph of the closed test box with the gas supply is shown in figure 4.2j. Additionally, the pronounce red coaxial cables, the picoammeter underneath the testing table and the computer monitor to display the measurement results can be seen. A closeup view of a hygrometer inside the test box is shown in figure 4.2k

**Measurement process** When the relative humidity values of all three hygrometers are well below 10 % the gas flow is reduced until the vibrations of the GEM foil stop (i.e. are not visible by eye anymore). Then the measurement process can be started via a LabVIEW™ application, which simultaneously records and displays the leakage current values of all segments. Secondary, the HV power supply can be controlled via this application. During the measurement, one should refrain from touching the cables or moving above the GEM foil, because this already induces measurable currents. All incidents and problems during the measurement such as the occurrence of discharges are documented in a test logbook. A snapshot of the LabVIEW™ panel and the test logbook window in the background is shown in figure 4.2l. A detailed description of the measurement process can be found in the dedicated section 4.4.

**Post processing** After the measurement time of 1000 s the applied voltage is slowly (several minutes) ramped down in order to entirely discharge the GEM foil. When the ramp down is complete, the gas supply is removed and the test box is opened. Then the drawer is taken out of the test box and the cover plate is removed. To take out the GEM foil, the ground connection plate has to be turned back. The GEM foil is put back into its paper back and is finally stored in the dry cabinet again. Now a new foil can be tested.

## 4.4 Measurement process and data

The main steps of the measurement process have a visible impact on the leakage current signal of every foil segment. Therefore, two exemplary plots of the leakage current from one segment (in this case segment 0) of two different O3 foils against the measurement time are shown in figure 4.3. The numbers correspond to the measurement steps, which are explained in the following. Because the measured leakage values are negative, the absolute value is taken in order to enable the use of a logarithmic leakage current scale. Every measurement point in these plots correspond to time-averaged value of the measured leakage current leakage current over a 1 s time interval.

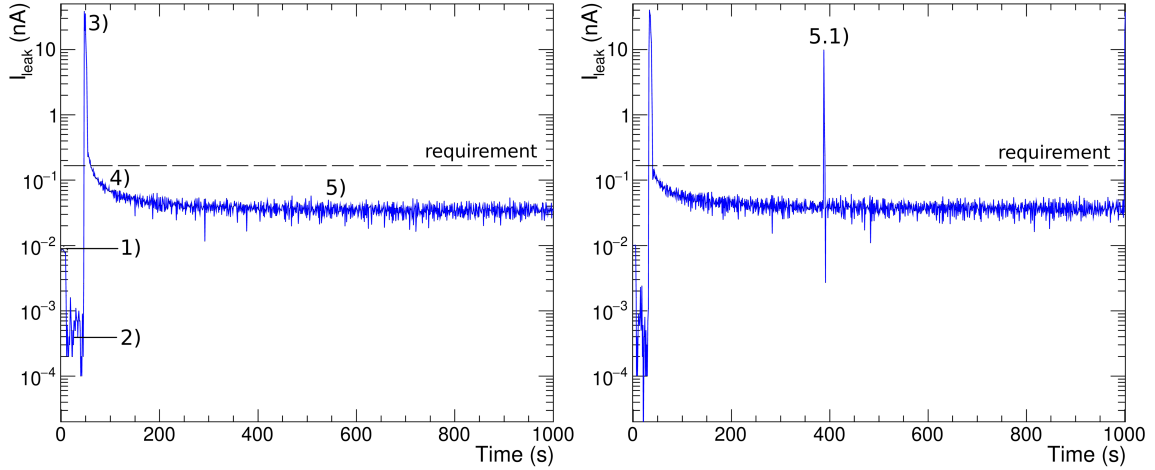


**Figure 4.3** Exemplary leakage current signals (blue line) of segment 0 from the measurement of two different OROC 3 foils. Both foils are measured after being framed at GSI. Foil O3-G1-010 (**left**) shows an ideal behaviour, while an isolated discharge occurred after roughly 400 s in the measurement of the other foil O3-G1-011 (**right**). In both plots the leakage current test requirement of 0.17 nA is denoted by a black dashed line. Additionally, the main steps in the measurement process are denoted by numbers and described in the text

As a consequence, one leakage current value per second for every segment is recorded and stored in a text file, which is then uploaded to a database.

**1) Offset measurement** Since the leakage current of a GEM foil is only of the order of 100 pA, a very precise measurement is needed. For this reason, the measurement values have to be corrected for a potential offset provided by the electronics. Therefore, a *reference measurement* of the current level with no potential difference applied across the GEM foil is done during the first few seconds of the data recording (plateau at step 1). Actually, the minimal output voltage of the HV power supply is not 0 V, but 2.41 V. The time-averaged value from this reference measurement is then used to correct the following data.

**2) Offset subtraction** The measurement of the leakage current is a very susceptible measurement. Thus, it has to be reassured if the offset was correctly taken. For example even human movements close to the test box or a motion of the coaxial cables can induce several 10 to few 100 pA and hence the reference measurement and the resulting offset value would be unfeasible. In this case the measurement has to be started again. When the offset value was taken correctly as in figure 4.3, it is subtracted from all the further data. After the current level has dropped, it is observed for another few seconds to ensure a correct subtraction.

**3) Application of the high voltage** After the successful offset correction the high potential difference can be applied across the GEM foil. Since a slow ramp-up of the voltage can cause the melting of potential dust particles, which then may result in a short circuit in a foil segment, the voltage is ramped up as fast as possible. In this case it is believed that the fast ramping *burns* the dust and thus cleans the foil. The fastest possible ramping is achieved by unplugging the HV cable from the power supply and ramp up the voltage to the nominal value of  $U_{\text{HV}} = -500$  V without any connection. The unplugging process induces currents, which cause the bump during step 2). When the voltage has stabilised at the desired value the high voltage cable is re-plugged into the power supply. As a consequence the foil charges up and a comparably high charging current of several 10 nA can be measured, which corresponds to the sharp spike in step 3).

**4) Saturation of the charging current** Since a GEM foil segment is comparable to a plate capacitor, also their charging behaviour is comparable. Therefore, after the application of the potential difference the charging current decays exponentially with a time constant of the order of  $\tau = RC$  (sub-second time scale). Due to the limited power output of the HV source, the large charging current at the beginning reduces the source voltage, which then counteracts to compensate this change. In the course of time, the current converges towards the level of the average leakage current.

**5) Leakage current level** During the saturation process in step 4) the currents are too high to get meaningful measurement values in order to characterise the leakage current of the GEM foil. Empirically it is found that the current has settled to a sufficient level after approximately 300 s total measurement time. In figure 4.3 it is shown that the leakage current level of the representative foils is well below the test requirements. The entire length of the leakage current measurement depends on its aim. If the long term behaviour of the GEM foil is under investigation the measurement can last up to 12 h. For QA purposes a total measurement time of 1000 s (less than 17 min) is considered as sufficient in order to get reliable leakage current values for each segment. For this reason, only this kind of tests are considered in the scope of this thesis.

**5.1) Discharges** Due to the potential difference applied across the foil and the resulting high electric fields inside the GEM holes, (short) discharges between the two GEM metal layers can occur. Often they are referred to as *sparks*. There are different factors which can increase the discharge probability of a GEM foil during the leakage current test. The major ones are dust particles on the foil, (surface) defects in the GEM structure and humidity of the working gas. When a spark occurs, the current often rises by two orders of magnitude or more, which is nicely illustrated in the example measurement shown figure 4.3 on the right plot. Therefore, every spark poses a risk of permanently damaging the foil. Fortunately, they are very rare given that the foils are treated with special care.

## 5 Determining factors of leakage current

The leakage current test plays a central role in the QA of GEM foils (cf. chapter 4). To have an estimate of the foil quality it is not necessary to consider the entire time development of the leakage current. Particularly if the foil performs well during the leakage current test in terms of its overall leakage current level and no or only single, isolated sparks occur, the relevant quality information of a GEM foil can be efficiently expressed with an appropriate set of values. For the ALICE TPC upgrade the major ones are the average leakage current of all segments and the number of sparks during the measurement procedure.

However, the purpose of this thesis is not only the QA of GEM foils with the leakage current test, but also the investigation of the determining factors of leakage current. The correlations of the leakage current with different (geometrical) properties of the GEM foils are of great interest. If these determining factors and their impact on the foil's leakage current are well understood, there is the chance to predict the foil's performance in a stack in terms of the effective gain or ion backflow properties. In this case the foils could be combined in an optimal way in order to achieve the optimal overall performance only using the data of QA measurements such as the leakage current and the hole properties from the optical inspection. Additionally, environmental factors like the humidity, pressure, temperature and type of the working gas play a role. In the sections 5.3, 5.4 and 5.5 three determining factors, namely the size of the active area, the pitch size and the hole properties, are investigated respectively.

### 5.1 Post-processing of the leakage current data

In order to further investigate the leakage current in terms of different dependencies, there is the need for a single representative value for each foil segment and measurement. Therefore, the raw data of the leakage current test (text files containing the measurement values), which contains information about the time development of the current over the measurement time as described in section 4.4, has to be post-processed. This is done with the C++ based data analysis framework *ROOT* developed at CERN. It provides the means for the efficient processing of big data samples and their storage. Furthermore, there are tools for the statistical analysis of data and the visualisation of results [42]. Hence, *ROOT* is well suited for the use in the post-processing and evaluation of the leakage current data within the scope of this thesis.

As already mentioned in section 4.4, paragraph 5), the current through the GEM segments, after applying the high potential difference across the foil, saturates at the leakage current level about 300 s past the start of data recording. Therefore, the leakage current values after this time are used in order to obtain a single, representative leakage current value to characterise each segment of the GEM foil during one measurement.

Figure 5.1 shows two different examples of leakage current distributions based on the raw data illustrated in figure 4.3. Every entry in the histograms corresponds to a measured leakage current value for measurement times larger than 300 s until the end of the data recording. Since the total measurement time is 1000 s and one value per second is stored in the raw data file, both histograms have 700 entries. The leakage current distributions are fitted with a Gaussian using the maximum likelihood method. In spite of some isolated outliers the data points are well described by the fit. As an estimate of the goodness of the fits the  $\chi^2$ -value and the degrees of freedom (ndf) are given in the summary boxes in the upper right corner of the plots. Furthermore,

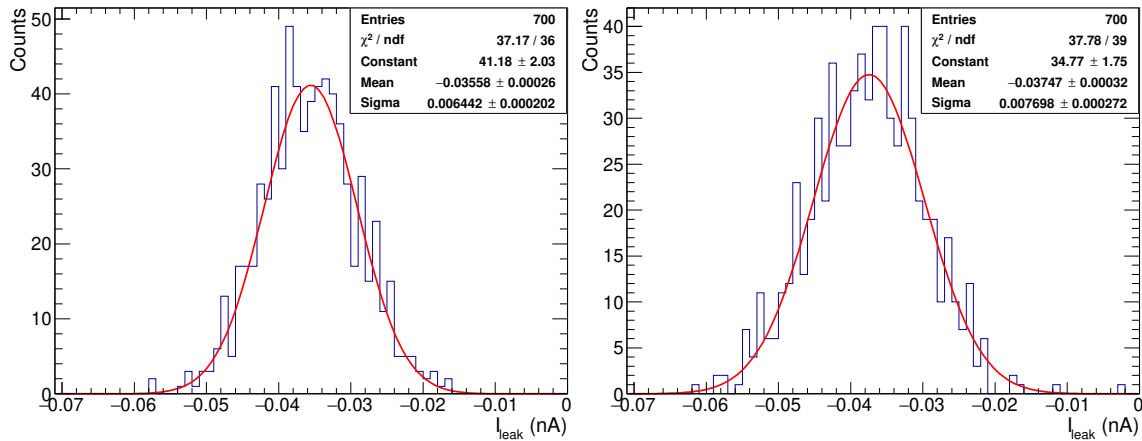


**Figure 5.1** Exemplary leakage current distributions for measurement times  $t > 300$  s. The raw data of the same GEM foils and segments, namely O3-G1-010 seg. 0 (**left**) and O3-G1-011 seg. 0 (**right**) measured after framing at GSI, as illustrated in figure 4.3 is used. A Gaussian (red line) is fitted to the distributions to obtain a representative leakage current value for each segment

the obtained fit parameters, namely a *Constant* (normalisation factor), the *Mean*, and the standard deviation *Sigma*, with their respective errors are also listed there.

As a matter of fact, the well matching Gaussian fits, which are all of similar goodness for the leakage current distributions of each foil segment and for every measurement at the different institutes, prove that the 300 s-threshold is reasonable. If the current had not saturated to a sufficient extent, the resulting leakage current distribution would have been asymmetric towards larger values. This would then result in a worse description by the symmetric Gaussian curve. Furthermore, it shows that the amplitudes of the noise during the test is Gauss distributed.

Since it is found that this fitting method of the leakage current distributions is stable in terms of fit convergence and reliability of the fit results, it is convenient to use it for the characterisation of a foil segment. Even if individual discharges occurred during the measurement, the increased leakage current values of these events are so large (at least one order of magnitude above the usual level) and few ( $\mathcal{O}(5)$ ) that they are outside the scope of the fit. Thus, they are simply ignored. The mean values and their errors are extracted from the Gaussian fits in order to have a representative value for each foil segment during one measurement. To make the later visualisation of the analysis results more intuitive, they are multiplied by  $-1$  in order to get rid of the conventional minus sign of the current values. The absolute value is not considered to conserve a possible change of sign by fluctuations or induction of a current.

Finally, the obtained mean leakage current values per segment for all available raw data (cutoff-date: 18 February 2018) of all four foil sizes (I, O1, O2, O3) and both pitches (SP, LP) are stored in text files and more efficient ROOT-files for further analysis. In the following the term *leakage current* or *leakage current per segment* is used to refer to these values.

## 5.2 Data comparison between the measurement sites

For the analysis of the determining factors of leakage current through the GEM foils the largest possible statistics has to be exploited. This includes measurement data from the different institutes that perform the leakage current tests as well as measurement data before and after the framing of the foils (see section 3.4). To legitimate this approach, it has to be verified that the leakage current measurements performed at the different institutes produces comparable data. Furthermore, it

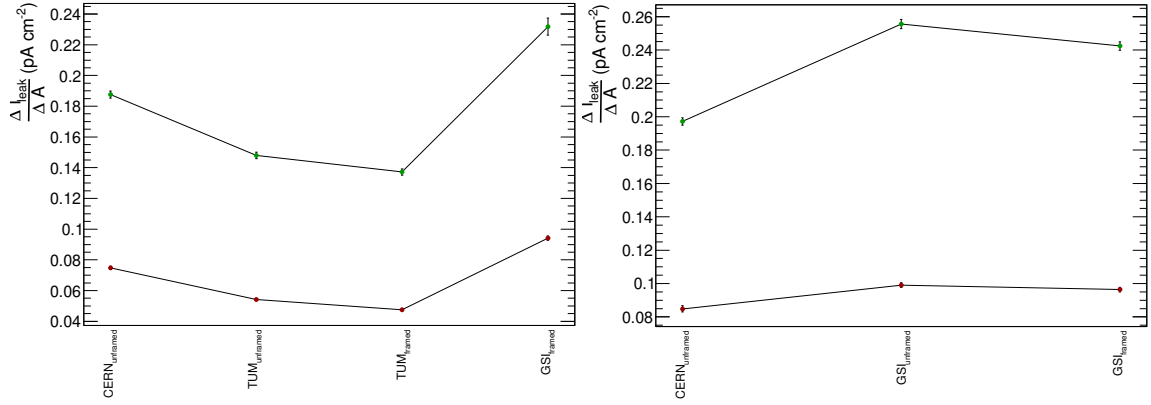


**Figure 5.2** Averages of all area normalised leakage current values per segment measured at the corresponding institutes (horizontal axis). Exemplary, data from O1 foils (**left**) and O3 foils (**right**) with standard (G1, G4, green dots) and large pitch (G2, G3, red dots) is used. The framing status of the foils is given in the index of the institutes

has to be checked whether the framing procedure causes has a systematic effect on the leakage current of a GEM foil.

In principle the leakage current data of the different institutes should be comparable, since the leakage current measurement in the context of the ALICE TPC upgrade is a standardised method. Therefore, all the institutes use similar equipment, e.g. same models of picoammeters and power supplies, and effectively follow the same test procedure, which is described in section 4.3. However, there may be different systematic effects on the leakage current measurements. For example there is the different atmospheric pressure and temperature because of the various geographic positions of the institutes. Additionally, the tests are performed in cleanroom conditions, which can differ from institute to institute. Also the cleanrooms are diversely equipped with other measuring systems or devices, which theoretically can contribute to the noise and thus have an influence (e.g. via electromagnetic radiation) on the running leakage current measurement.

Unfortunately, the aforementioned variables cannot be directly addressed within the scope of this thesis. Nonetheless, the average leakage current level measured at the different institutes can be considered in order to review their comparability. To be independent of the segment sizes (see section 5.3) and to enhance the statistics, the average *area normalised leakage currents* for each institute are compared. In particular, the values before and after framing the foil are included. The two plots in figure 5.2 exemplarily illustrate this for O1 foils on the left and O3 foils on the right. The two different pitch sizes (SP, LP) are denoted by colours. Data points of standard pitch foils (G1, G4) are identified by green dots, while the data points of large pitch foils (G2, G3) are shown with red dots. As GSI acts as framing and chamber building institute at the same time, there is one step less in the right plot. Leakage current data from the other OROC building institute in Bucharest is not used at all, since there were problems with the unified data format.

First of all, it can already be seen that the leakage current level for SP foils is systematically higher in comparison to the LP foils. This phenomenon is addressed in section 5.4. Furthermore, it is visible that GSI provides significantly larger leakage current levels compared to CERN or the Technical University of Munich (TUM). This behaviour is also confirmed by the comparison of the leakage current levels for O2 foils, which are framed at the University of Bonn. On the contrary, the levels obtained for measurements at TUM and in Bonn are both (unframed and framed case) below the level of CERN. Also significantly different leakage current levels for the IROC foils can be found between the different institutes.

As a consequence, the data of the leakage current test at the different measurement sites is considered suitable for the quality assurance of the GEM foils. However, it is not comparable

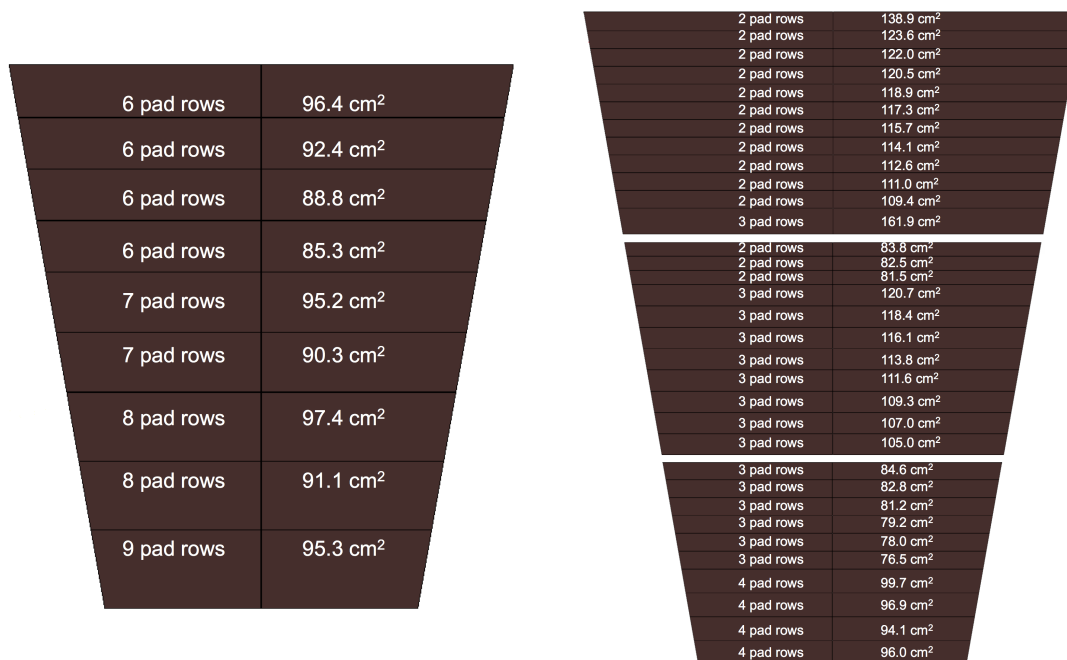


**Figure 5.3** Segment areas of IROC (**left**) and OROC (**right**) GEM foils and corresponding number of pad rows in the readout plane [43]

within the framework of a statistical analysis of the entire available leakage current data. On the basis of these results it has been decided to only make use of the leakage current data provided by CERN. Since every produced GEM foil for the ALICE TPC upgrade is measured there, this data set represents the highest available statistics of leakage current data, which has been measured under similar environmental conditions and is thus considered comparable. In this case a statistical analysis of this data set is legitimate.

Apart from this finding, this analysis offers the possibility to check the possible influence of the framing process on the foil's leakage current level. There, it has been found, that the leakage current through the foil either stays on a similar level or even improves after the framing. For example in the both plots shown in figure 5.2 the leakage current level slightly drops, when the foil is framed. A possible reason of this behaviour is the increased mechanical sturdiness, which is provided by the glass fibre frame. Doing the leakage current measurement, it has been observed that a vibration due to the nitrogen gas flow may enhance the leakage current of a GEM foil. Evidently, a framed foil is less susceptible to vibration and thus can have a lower leakage current level. However, this hypothesis needs further investigation and may not be the only possible reason causing this effect.

### 5.3 Area dependence of leakage current

An intuitive determining factor of leakage current through a GEM foil (segment) is the size of its active area. For example, within the scope of multiple leakage current tests of O3 foils at GSI, it is observed that the last two segments of each foil (segment 22 and 23, see figure 3.5) provide a systematically larger leakage current in comparison to the other ones. At the same time these two are the largest segments of an O3 foil, which already indicates a correlation between the leakage current and the size of the segment area.

The basic idea of the area dependence of the leakage current is the following. A larger area of a foil segment and thus also a larger number of GEM holes increases the probability of leakage current flowing across the foil. Since the density of the GEM holes is constant (in the ideal case),

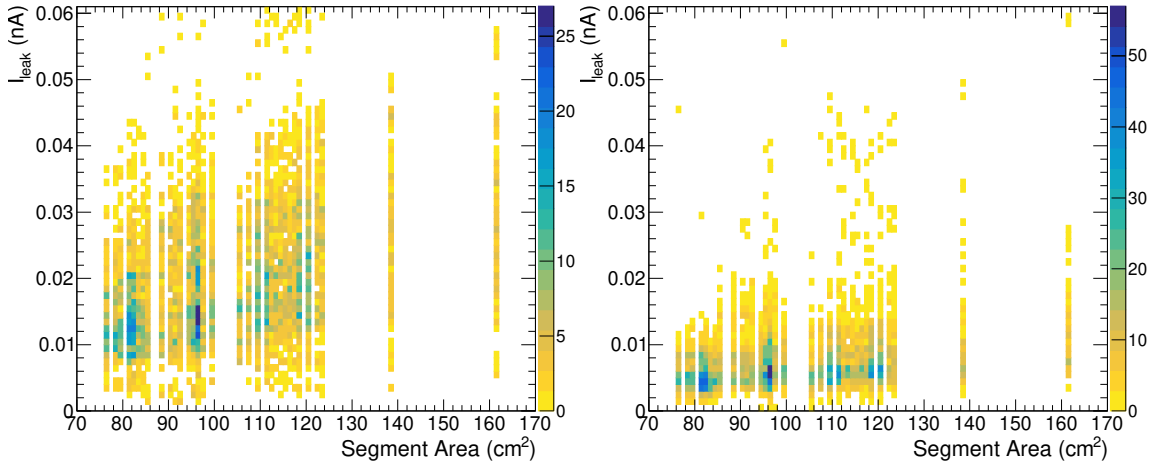


**Figure 5.4** Two-dimensional correlation plots to investigate the area dependence of leakage current. The number of entries per cell is represented by a colour scale. Foils with standard pitch (**left**) and large pitch (**right**) are separately analysed. Only CERN data for all four foil sizes (I, O1, O2, O3) is used

a proportionality between the leakage current and the area of the segment is expected. As a consequence, doubling the active area of the GEM foil would lead to a doubled leakage current.

Despite the intention that the segments of the GEM foils for the ALICE TPC upgrade should be approximately equal in size, there are technical constraints which actually lead to deviating segment areas. One reason for the different segment areas is the pad plane geometry. In order to optimise the performance of the readout chambers, the inactive borders of the GEM foil segments should match the patterning of the pad plane. This leads to constraints on the segment heights, which are correlated to the pad heights [21]. Together with the trapezoidal shape of the foils, the resulting segment areas vary strongly. Figure 5.3 illustrates these different segment areas for all foil sizes involved in the ALICE TPC upgrade. Additionally, the corresponding number of pad rows is denoted. Since the segments of the foils are pairwise mirror-symmetric, two subsequently numbered segments have the same area. The segments 22 and 23 of an O3 foil, which cover an area of  $161.9 \text{ cm}^2$ , are the largest ones. In contrast the smallest segments 10 and 11 only have an area of  $76.5 \text{ cm}^2$ . Hence, with a maximal area difference of  $85.4 \text{ cm}^2$  between the segments the GEM foils of the ALICE TPC upgrade are well suited to investigate the area dependence of the leakage current.

### 5.3.1 Results and discussion

To get a first assessment of the leakage current's dependence on the corresponding segment size, two two-dimensional correlation plots are shown in figure 5.4. For compatibility reasons foils of different pitch sizes are separately analysed. Therefore, the left plot represents the result for standard pitch foils (G1, G4), while the right plot shows the result for foils with large pitch. The underlying leakage current data for both plots is provided by CERN and represents leakage current measurements on GEM foils of all available sizes (I, O1, O2, O3). Every entry in the two histograms corresponds to one segment within one leakage current measurement.

As expected, a linear dependence of the leakage current on the segment area is visible for the SP foils on the left. However, for the LP foils this correlation is much less pronounced. This difference between the two plots can be qualitatively understood regarding the different pitch sizes. Evidently, the hole density of SP foils compared to LP foils is larger. Therefore, also the change in the leakage current when the segment area is increased by a certain amount is larger

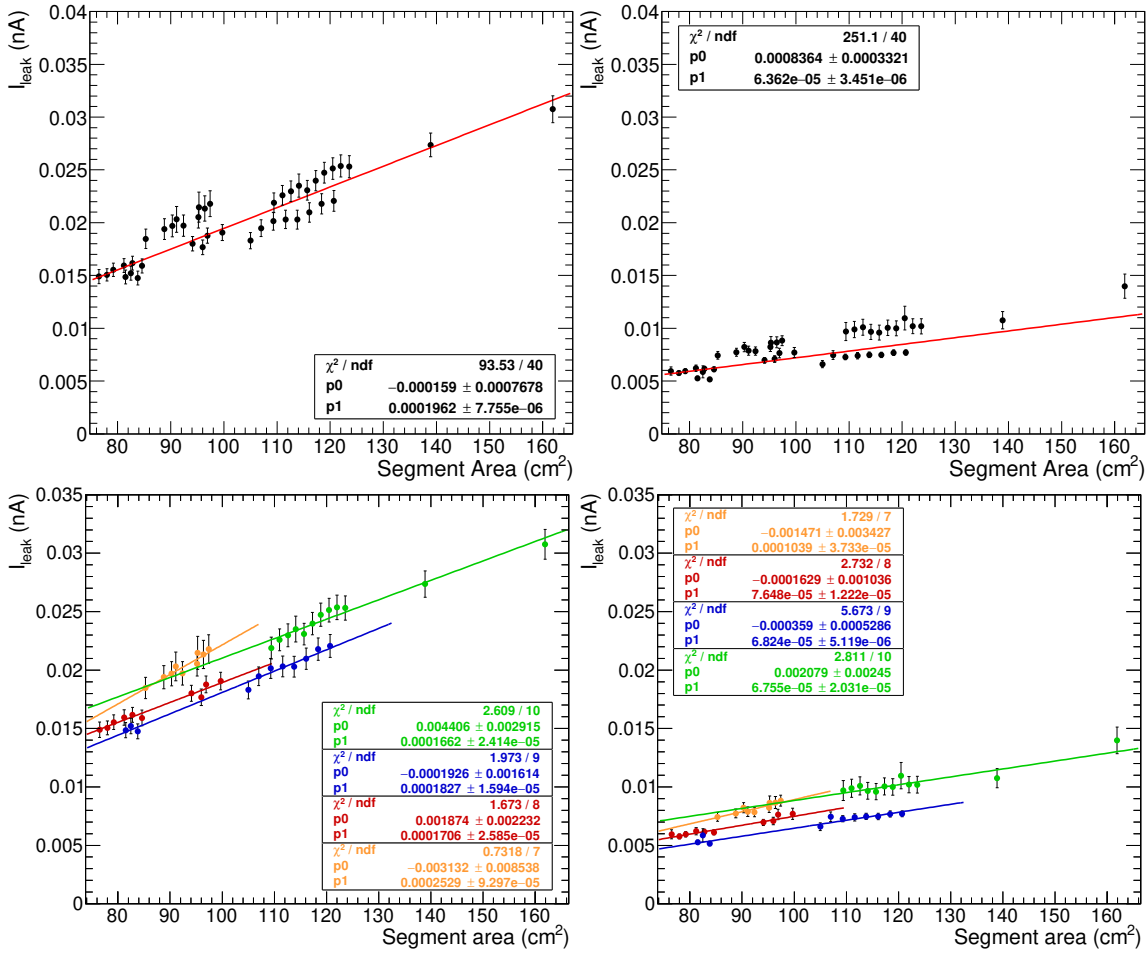


**Figure 5.5** Mean leakage current for every available segment area based on the same data that was used for the correlation plots in figure 5.4.

**(top)** A linear fit (red) line is performed to describe the data of SP foils (**left**) and LP foils (**right**). The corresponding results for the fit parameters, offset ( $p_0$ ) and slope ( $p_1$ ), as well as the  $\chi^2$ -value and the degrees of freedom (ndf) are listed in the boxes.

**(bottom)** The overall data from above can be decomposed into the different contributions of the four foil sizes, IROC (orange), O1 (red), O2 (blue) and O3 (green). Each of these contributions is itself fitted with a straight line and the fit results are summarised in the corresponding boxes

in the SP case, because more holes per area are contributing to the leakage current as compared to the LP case.

In order to gain more, quantitative information on the correlation between area and leakage current, the leakage current distributions of every available segment area are considered. As an example the 12 leakage current distributions for the segment sizes of O3 foils are shown in figure A.1 (section A.4). The mean value and its statistical error are obtained from each of these distributions and plotted against the associated segment areas ( $A$ ). The resulting graphs for standard and large pitch foils can be seen in figure 5.5 at the top left and right, respectively.

In both cases a straight line according to  $I_{leak} = p_0 + p_1 A$ , with an offset ( $p_0$ ) and a slope ( $p_1$ ) as free parameters, is fitted to the data. At first sight, the fits seem to describe the experimental data well and thus the linear dependence of the leakage current on the area is confirmed in both cases. The impact of the pitch size, which results in a substantially smaller slope of the linear fit for the LP data, is still distinctly visible. Considering the goodness of the fits it can be asserted that it is not as good as expected for such clear linear relations. A more detailed look on the data

reveals a certain pattern. More precisely, the data points can be grouped into four distinguishable contributions. Thus, different contributions of the four foil sizes (I, O1, O2, O3) are indicated. For this reason the data based on the measurement of foils with the same size is plotted separately again. This decomposition of the overall data for standard and large pitch foils is shown in figure 5.5 at the bottom left and right, respectively.

There, the data sets of the different foil sizes are represented by colours, namely orange for IROC, red for OROC 1, blue for OROC 2 and green for OROC 3 foils. Furthermore, it is visible that the distinguishable data groups in the collective plots above correspond to the contributions of the different foil sizes. Taking into account the linear behaviour of the data points, it can be seen that I and O3 foils provide a higher leakage current level compared to O1 and O2 foils, which gives a hint of a systematic effect on the leakage current caused by the production process of the GEM foils. This hypothesis is further discussed in chapter 6.

Each of the data subsets for the four foil sizes is individually fitted with a straight line. For all the different cases the data is well described by the fits. In contrast to the overall fit all the data points are in agreement with the individual graphs of the linear fit function within their statistical error. Furthermore, it can be seen that I and O3 foils seem to lie on the same line. In the case of O1 and O2 foils the linear graphs hint at a similar, but less strong, trend. The obtained parameter values of all linear fits shown in figure 5.5 are summarised in table 5.1. In order to make a statement concerning the informative value of the linear fits both fit parameter values, offset and slope, are compared with zero.

Pitch	Foil sizes	Offset (nA)	Deviation from 0 ( $\sigma$ )	Slope (nA cm <sup>-2</sup> )	Deviation from 0 ( $\sigma$ )
SP	All	$(-1.6 \pm 7.7) \times 10^{-4}$	0.2	$(196.2 \pm 7.8) \times 10^{-6}$	25.2
	I	$(-3.1 \pm 8.5) \times 10^{-3}$	0.4	$(25.3 \pm 9.3) \times 10^{-5}$	2.7
	O1	$(1.9 \pm 2.2) \times 10^{-3}$	0.9	$(17.1 \pm 2.6) \times 10^{-5}$	6.6
	O2	$(-0.2 \pm 1.6) \times 10^{-3}$	0.1	$(18.3 \pm 1.6) \times 10^{-5}$	11.4
	O3	$(4.4 \pm 2.9) \times 10^{-3}$	1.5	$(16.6 \pm 2.4) \times 10^{-5}$	6.9
LP	All	$(8.4 \pm 3.3) \times 10^{-4}$	2.5	$(63.6 \pm 3.5) \times 10^{-6}$	18.2
	I	$(-1.5 \pm 3.4) \times 10^{-3}$	0.4	$(10.4 \pm 3.7) \times 10^{-5}$	2.8
	O1	$(-0.2 \pm 1.0) \times 10^{-3}$	0.2	$(7.6 \pm 1.2) \times 10^{-5}$	6.3
	O2	$(-0.4 \pm 0.5) \times 10^{-3}$	0.8	$(68.2 \pm 5.1) \times 10^{-6}$	13.4
	O3	$(2.1 \pm 2.5) \times 10^{-3}$	0.8	$(6.7 \pm 2.0) \times 10^{-5}$	3.4

**Table 5.1** Summary of the parameter values, offset and slope, of all linear fits shown in figure 5.5 (rounded to two significant digits). Additionally, the deviation from zero (rounded to one decimal place) is listed for both parameters

The assumption that the leakage current through a GEM foil segment becomes zero with a vanishing segment area is reasonable. Therefore, the offset parameter of the linear fits is expected to be zero. In the table it is shown that almost every found offset value is in agreement with zero within its error range. The exceptions are the values of the cases SP-O3 and LP-All, which have deviations of  $1.5 \sigma$  and  $2.5 \sigma$  from zero, respectively. Still, this is not considered significant and therefore the fits confirm this hypothesis.

Also the obtained slope parameter values are compared with zero in order to exclude a possible constant behaviour. In spite of both IROC and the LP-O3 case, all slope values deviate from zero by more than  $5 \sigma$ . For the LP-O3 case the deviation is at least  $3.4 \sigma$ . The two IROC cases (SP and LP) only deviate from zero by  $2.7 \sigma$  and  $2.8 \sigma$ , respectively. At the same time these data sets cover the smallest area range, which results in relatively large errors of the fit parameters. For this reason, the anticipated proportional correlation between the leakage current and the GEM area is proven. Furthermore, the obtained slope values within one pitch size case are pairwise

compatible in terms of their respective errors. The average slope of the decomposition fits is  $(19.3 \pm 2.7) \times 10^{-2} \text{ pA cm}^{-2}$  for SP foils and  $(7.9 \pm 1.7) \times 10^{-2} \text{ pA cm}^{-2}$  for LP foils.

## 5.4 Pitch size dependence of leakage current

Within the investigation of the area dependence of leakage current through GEM foils in section 5.3 it has been shown that the pitch size also has an impact on the leakage current. There, it is found that the increase of the leakage current with the area for standard pitch foils is significantly larger than for foils with a large pitch. An elementary physical explanation of this effect is the following. Every GEM hole provides a certain probability for electrons to travel across the foil from one metal layer to the other. In the sum over the many thousand holes of one foil segment this can be measured as leakage current. Thus, for a given area of a GEM foil segment the leakage current level increases with the hole density, which is directly linked to the pitch size. For this reason the area normalised leakage current can be considered in order to investigate the pitch size dependence of leakage current.

The ALICE TPC upgrade involves GEM foils with two different pitch sizes. GEM 1 and GEM 4 foils have a *standard pitch* (SP) of  $140 \mu\text{m}$ , while for GEM 2 and GEM 3 foils with a *large pitch* (LP) the pitch size is doubled to  $280 \mu\text{m}$ . A schematic of the hexagonal hole pattern for these two cases is illustrated in figure 5.6. There, GEM holes of the LP pattern, which coincide with holes from the SP case (white circles), are highlighted with light blue colour. In order to compare the different hole densities for both cases, the red frame delimits the area of a *unit cell* of the hexagonal LP hole pattern. From this it can be derived that the hole density of SP foils is larger by a factor of four as compared to LP foils. Under the assumption that the leakage current of a GEM foil exclusively flows through the holes and every hole provides an equal contribution to it, the leakage current directly scales with the according hole density. Therefore, it can be expected that the area normalised leakage current of SP foils is higher than the one of LP foils by a factor of four as well.

A first estimate whether this hypothesis can be considered as true can be obtained by considering the slopes for the linear fits in figure 5.5. Since they provide a value for the area normalised leakage current, the ratio of the slopes between the SP and the LP area dependence analysis can be compared to the expectation value 4. For example the ratio of the mean slopes, which are obtained at the end of subsection 5.3.1, yields  $2.4 \pm 0.6$ . This corresponds to a deviation from the expectation of approximately  $2.5 \sigma$ , which is already an indication that there may be an other contribution to the area normalised leakage current besides the hole density.

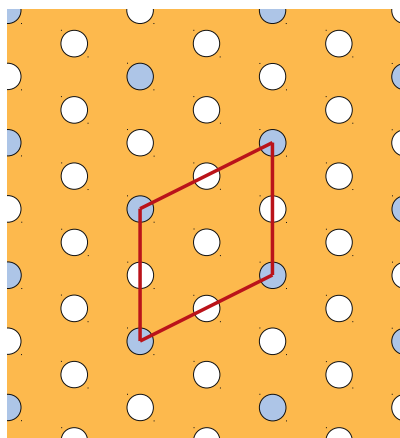


**Figure 5.6** Hexagonal hole pattern for standard pitch (white and blue circles) and large pitch (blue circles) GEM foils. The red frame represents an unit cell of the large pitch pattern

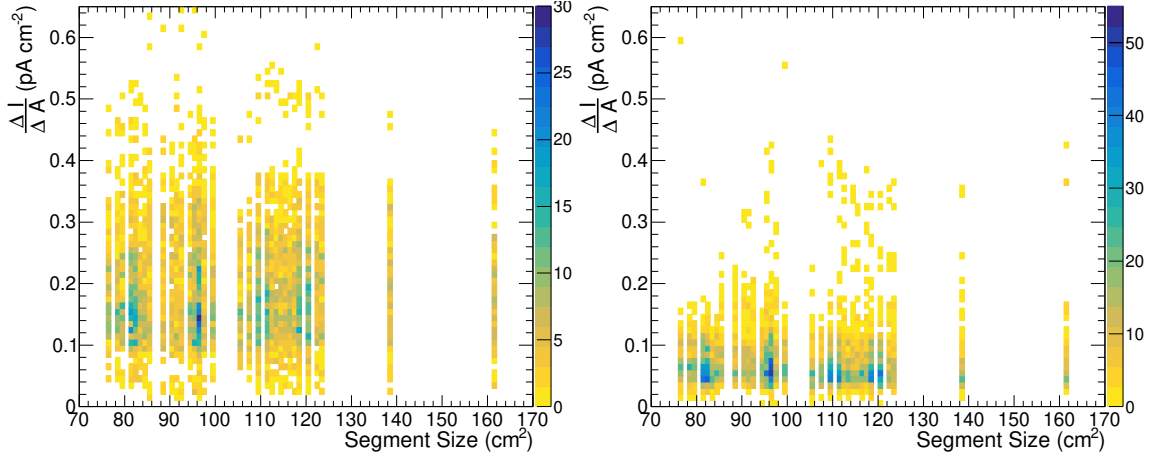


**Figure 5.7** Correlation plots for area normalised leakage current versus segment area based on the same data as in figure 5.4. SP foil data is shown on the **left**, while LP foils are represented on the **right**. Entries per cell are encoded by a colour scale. Only data measured at CERN is used

### 5.4.1 Results and discussion

For a more detailed investigation of the pitch size impact, all available leakage current data is normalised by the area. More precisely, every leakage current value is divided by the design value of the respective segment area, which are summarised in figure 5.3. In order to check whether this normalisation process has been done correctly, the correlation between the obtained area normalised leakage current and the segment size for SP and LP foils is shown in figure 5.7 on the left and right, respectively. It is clearly visible that in both cases the area normalised leakage current stays on a constant level over the entire area value range. Furthermore, this impression is quantitatively confirmed by the application of a linear fit (not shown in the figure) to both of the data sets. The found slope parameter is  $(-4.4 \pm 15.7) \times 10^{-5} \text{ pA cm}^{-4}$  for SP and  $(4.9 \pm 11.6) \times 10^{-5} \text{ pA cm}^{-4}$  for LP data. Since both values are compatible with 0 within their error ranges, the area normalisation is considered successful. Thus, the obtained area normalised leakage current data is reasonable for the use in the further analysis of the pitch size dependence of leakage current.

In figure 5.7 it is also shown, that the area normalised leakage current level of SP foils is distinctly higher than the one of LP foils. To gain more quantitative information on the difference between the SP and LP case, the data of the correlation plots is projected along the *area-axis* in order to obtain the two one-dimensional area normalised leakage current distributions, which are shown in figure 5.8. The distribution based on the data from SP foils is denoted by a green line, while the one for LP foils is shown in red. It is visible that the SP distribution is broader than the other one. This may be explained by the higher level of leakage current, which is linked to higher fluctuations. However, this needs to be clarified within a dedicated investigation. Both distributions show a tail towards larger current values. A possible explanation is the high probability of having imperfections in the GEM foil, which cause a higher leakage current, while the probability to have an ideally behaving foil, which has almost no leakage current, is much smaller. This results in an asymmetric area normalised leakage current distribution towards larger current values.

Since in the analysis of the area dependence of leakage current in section 5.3 different contributions of the four foil sizes (I, O1, O2, O3) are found, it has to be checked whether a similar effect is also visible for the area normalised leakage current distributions. Therefore, the two distributions in figure 5.8 at the top are decomposed into these contributions. The result for the SP and LP case is illustrated in the same figure at the bottom left and right, respectively.

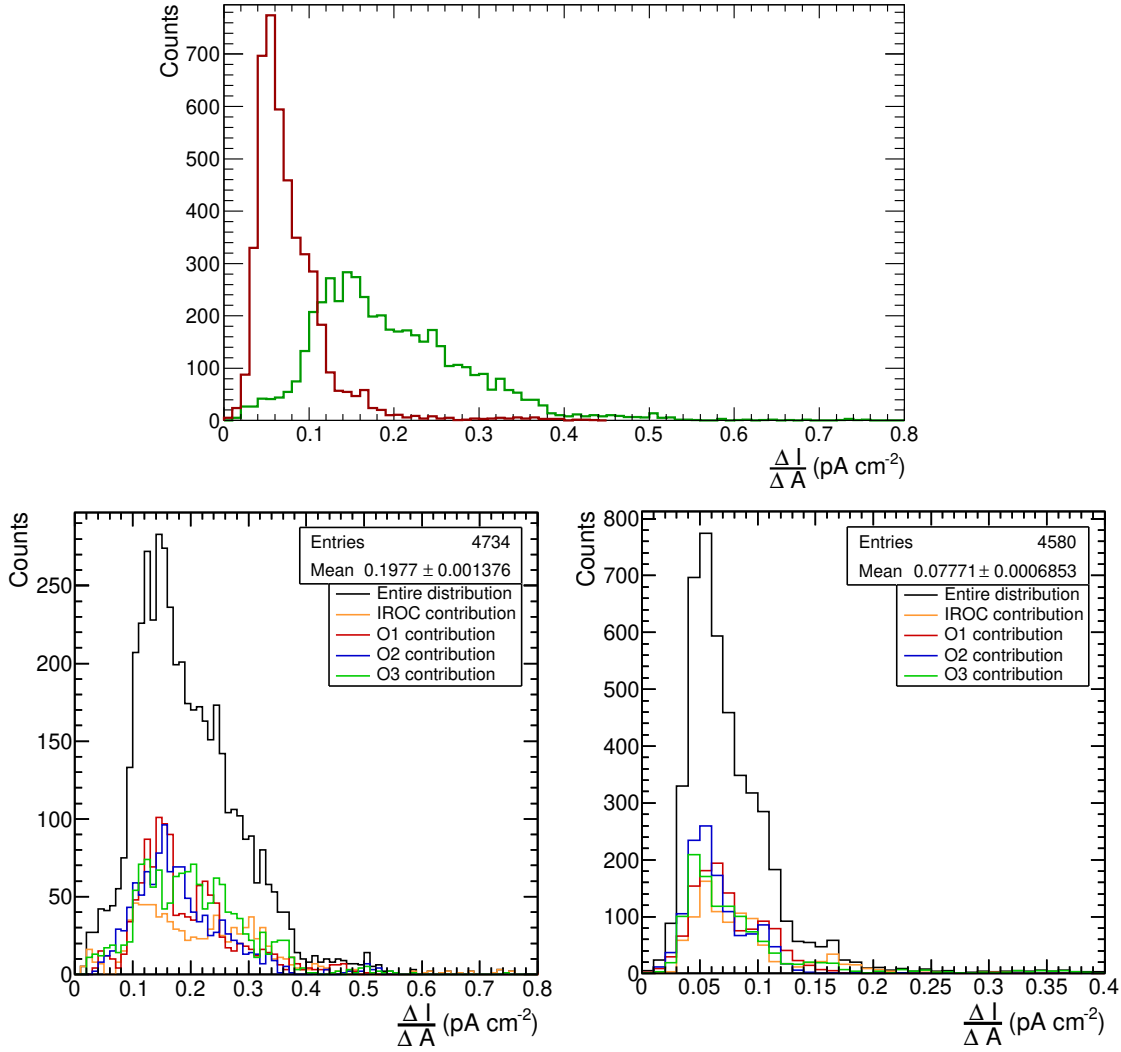


**Figure 5.8 (top)** Distributions of area normalised leakage current for SP (green line) and LP foils (red line). They represent the one-dimensional projections along the *area-axis* of the according data illustrated in figure 5.7.

**(bottom)** Decomposition of the overall area normalised leakage current distributions into the contributions of the four different foils sizes, I (orange), O1 (red), O2 (blue) and O3 (green). Note that the horizontal axis for the LP case (**right**) shows half the value range compared to the SP case (**left**). The number of entries, the mean value and the standard deviation listed in the boxes refer to the entire distributions

The black line represents the overall distribution, while the area normalised leakage current distributions for each foil size are represented by coloured lines, namely orange for I, red for O1, blue for O2 and green for O3 foils. Fortunately, there is no area normalised leakage current range, where only one foil size primarily contributes to the overall distribution. For this reason the data sets are considered suitable for the investigation of further determining factors of leakage current, e.g. the hole properties described in section 5.5, without losing statistics.

The mean values and according statistical errors are obtained and summarised in table 5.2 for every area normalised leakage current distribution shown in figure 5.8. Furthermore, the ratios between the corresponding values for the SP and LP case are calculated. Disregarding the O2 case the found ratios are pairwise compatible within a  $3\sigma$  error range. The O2 value shows deviations ranging from  $2.8\sigma$  to up to  $4.5\sigma$  with respect to all the other ratio values. Taking the average of

the different foil size values yields  $2.55 \pm 0.03$ , which itself is compatible with the ratio of the overall distributions within a  $1 \sigma$  error range.

Foil sizes	Pitch	Mean $\frac{\Delta I_{\text{leak}}}{\Delta A}$ (pA cm <sup>-2</sup> )	Ratio (mean values) $\left(\frac{\Delta I_{\text{leak}}}{\Delta A}\right)_{\text{SP}} / \left(\frac{\Delta I_{\text{leak}}}{\Delta A}\right)_{\text{LP}}$	Deviation from expectation 4 ( $\sigma$ )
All	SP	$0.198 \pm 0.001$	$2.54 \pm 0.03$	51.0
	LP	$0.0777 \pm 0.0007$		
I	SP	$0.220 \pm 0.004$	$2.50 \pm 0.06$	23.3
	LP	$0.088 \pm 0.002$		
O1	SP	$0.192 \pm 0.002$	$2.54 \pm 0.05$	28.9
	LP	$0.076 \pm 0.001$		
O2	SP	$0.182 \pm 0.002$	$2.76 \pm 0.06$	22.2
	LP	$0.0657 \pm 0.0010$		
O3	SP	$0.203 \pm 0.002$	$2.38 \pm 0.06$	26.3
	LP	$0.085 \pm 0.002$		

**Table 5.2** Summary of the mean area normalised leakage current values (rounded to one significant digit) obtained from the according distributions shown in figure 5.8. For five different foil size contributions the respective ratios between standard and large pitch values (rounded to one significant digit) and their deviation from 4 (rounded to one decimal place) are listed

In comparison with the predicted value of 4 for this ratio all the experimentally found values deviate by more than  $20 \sigma$ . Therefore, it is shown in a significant way that the assumptions of the hypothesis in the introduction of this section fail to describe the measured reality. As a consequence, there has to be at least one more determining factor of leakage current, which superimposes with the impact of the hole density. For example in contrast to the hypothesis that the leakage current solely flows through the GEM holes a plate capacitor without any holes also shows leakage current. For this reason, a possible explanation of this observed phenomenon could be boundary effects at the segment's delimitation or defects in the Kapton<sup>®</sup> insulator foil. Another factor which can contribute to a GEM foil's leakage current is the geometrical property of the holes themselves.

## 5.5 Dependence of the leakage current on hole properties

Not only the (segment) area or the pitch size, but also other factors are expected to have an impact on the leakage current of a GEM foil. Among these are the geometrical properties of the GEM holes themselves, which can slightly modify the strong electrical field inside (cf. section 2.1). For example the field inside a hole gets stronger with decreasing circumference (or diameter). If the leakage current is affected by the electrical field strength and thus the individual gain inside a hole, a higher leakage current is expected for smaller hole sizes.

In the framework of the ALICE TPC upgrade the GEM foils are produced using a photolithographic single mask technique and subsequent chemical etching of the hole pattern (cf. section 3.3). As it is illustrated in figure 3.3 this processing leads to a conical hole shape, which is why an inner and an outer diameter can be defined. By design the nominal value of the inner diameter is  $50 \mu\text{m}$ , while the outer diameter is  $70 \mu\text{m}$  and thus somewhat larger [21]. Despite all efforts to maintain hole diameters that are as constant as possible, there are always fluctuations due to the etching process. Exactly these deviations of the hole diameters from the nominal value provide the means to investigate the dependence of the leakage current on the geometrical hole

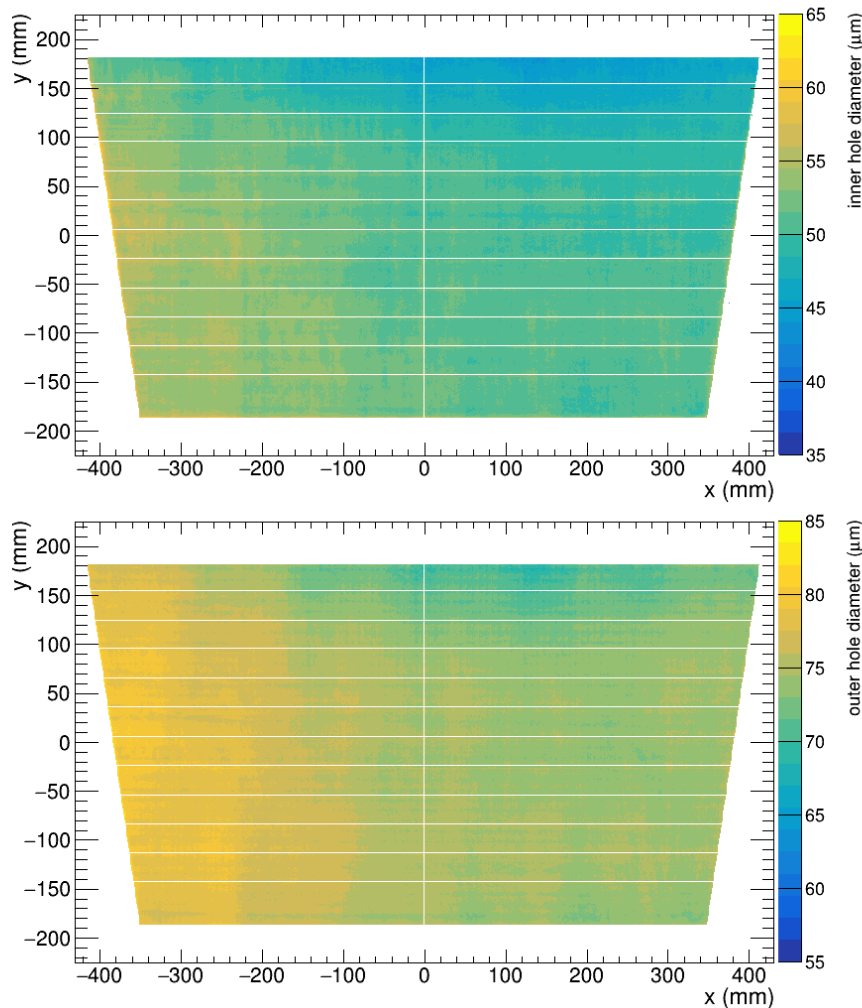


**Figure 5.9** Exemplary two-dimensional inner (**top**) and outer hole diameter (**bottom**) maps of the 03-G1-011 GEM foil. The different hole diameters are encoded by colour scales. In the xy-coordinate system every cell represents the mean hole diameter of a  $0.5 \text{ mm} \times 0.5 \text{ mm}$  area in this region. The inactive segment boundaries can be seen as white lines

properties of a GEM foil. In fact, the correlation between the area normalised leakage current and three quantities, namely the inner and outer diameter and the absolute difference between them (rim), is investigated in the following.

### 5.5.1 Post-processing of hole size data

After their production and some QA tests at CERN the GEM foils are sent to either Budapest or Helsinki for an optical inspection. There, aside from a long term leakage current test and a coarse visual inspection a precision optical measurement is done in order to determine the geometrical properties of the GEM holes such as the inner and outer hole diameters or small defects that were not detected in the first visual inspection. Among these are chemical residues from the etching, very large holes, missing holes, glue droplets or dust particles attached to the foil. More detailed information about these QA tests can be found in [21].

For this precision measurement the GEM foil is put on a back-illuminated light table. A high resolution 9-Megapixel camera mounted on a x-y positioning system above the table is used to scan the foil. The different hole diameters for every GEM hole are then extracted from the images. In figure 5.9 the exemplary two-dimensional inner (bottom) and outer hole diameter maps of

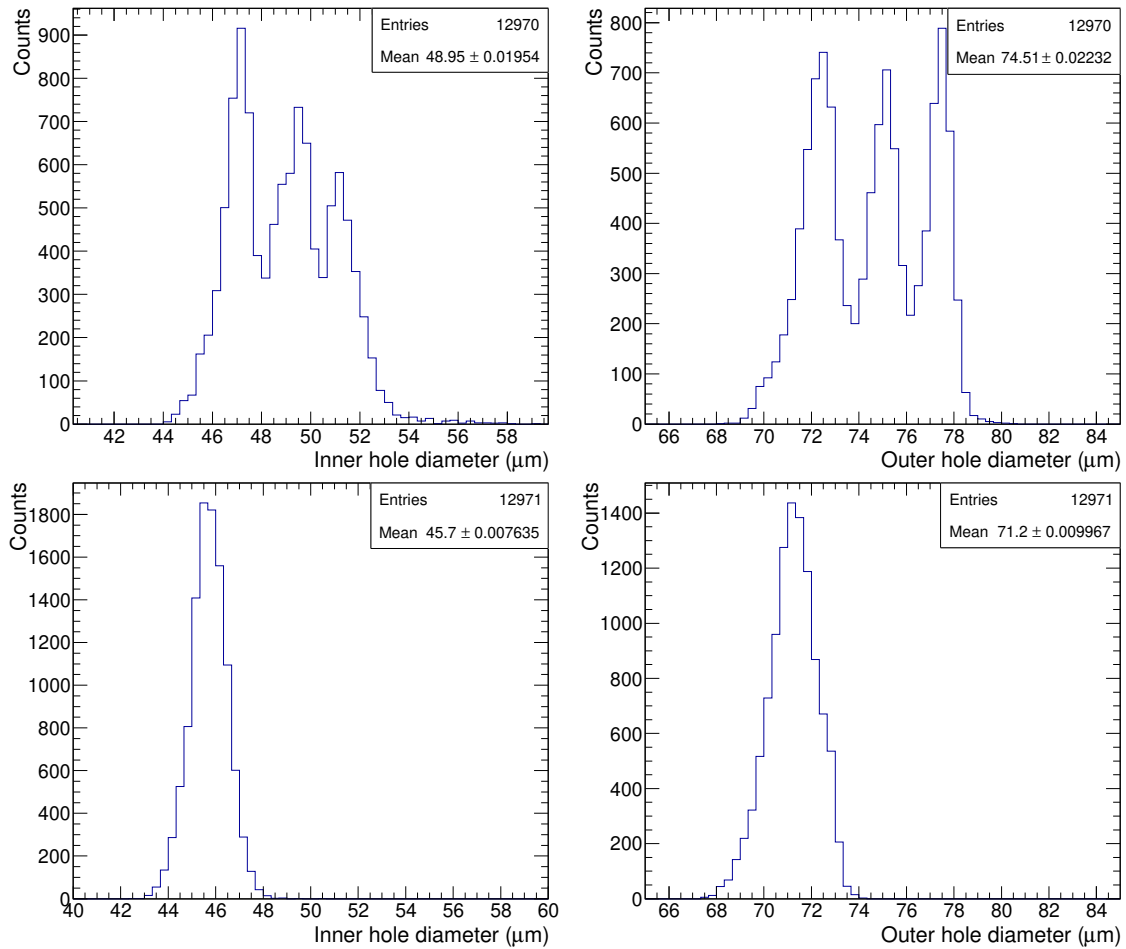


**Figure 5.10** Exemplary inner (**left**) and outer hole diameter (**right**) distributions of the two horizontally adjacent segments 0 (**top**) and 1 (**bottom**) of the O3-G1-011 GEM foil. The number of entries and the mean diameter value of the distributions are listed in the boxes in the top right-hand corner of the plots

an O3 foil are shown. Every  $0.5 \text{ mm} \times 0.5 \text{ mm}$ -cell in the plots corresponds to the averaged measured hole diameter over this area. Since the segment boundaries are inactive, i.e. have no holes, they appear as white lines inside the plots. Furthermore, a clear trend for both diameters can be seen in this specific example of the O3-G1-011 foil. Towards the left of the foil the diameter increases compared to the right hand side. It is found that this circumstance is not an isolated case, but is observed frequently due to the systematic influence of the etching procedure inside a chemical bath.

Since the leakage current data is only available per foil segment, but the hole diameters are measured over the entire foil size, geometrical cuts according to the segment boundaries are applied to the hole size data. Hence, hole diameter distributions can be obtained per segment. In figure 5.10 four of them are exemplarily shown. Left-hand, there are the inner hole diameter distributions for the two uppermost segments of the previously shown O3-G1-011 foil. The distribution for the left segment, segment 0, is shown at the top, while the one for the right hand side of the foil, segment 1, is shown at the bottom. The outer hole diameter distributions for the same segments are shown on the right in a similar way.

As illustrated in figure 5.9 the GEM foil under investigation tends to have increased hole diameters on the left as compared to the right, which is confirmed by the diameter distributions per segment in figure 5.10. Both distributions for segment 1, which represent the right half

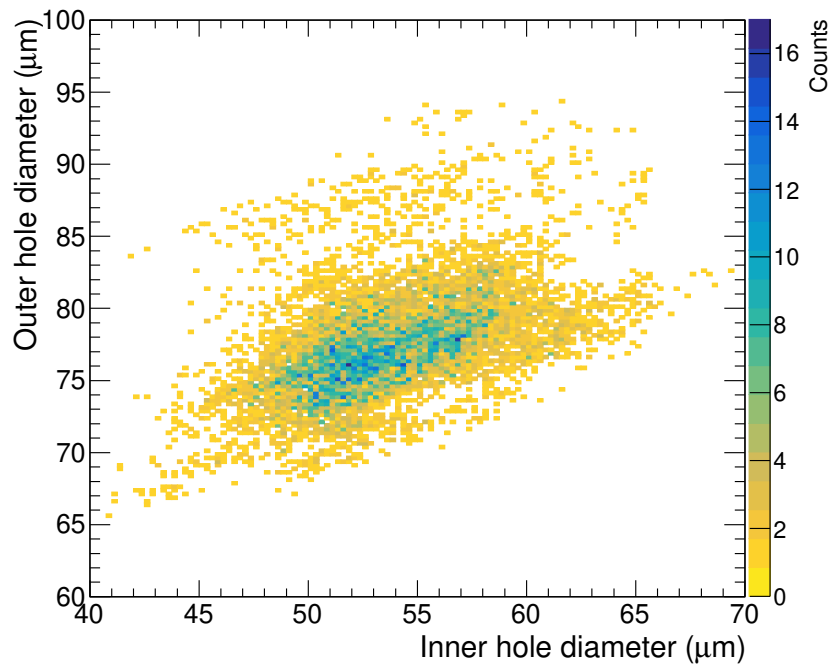


**Figure 5.11** Correlation between outer and inner hole diameter. Every entry represents the respective average outer and inner hole diameter per foil segment. The maximum available data for all four foils sizes (I, O1, O2, O3) and both pitch sizes (SP, LP) is used

of the foil, are relatively narrow around one central value and only one contribution can be observed. The mean values for the inner and the outer diameter are  $(45.700 \pm 0.008) \mu\text{m}$  and  $(72.200 \pm 0.010) \mu\text{m}$ , respectively. On the other hand, the distributions for segment 0 representing the left half of the foil are decidedly broader. In comparison to the according distributions for segment 0 below, there is also a contribution in the same diameter range (note the same horizontal scale as in the plots below). Additionally, two more peaks towards higher diameters can be seen. Especially in the two-dimensional map for the outer hole diameter in figure 5.9 an according stripy colour pattern can be seen in the left half of the foil. The respective mean values of the inner and outer hole diameter distribution are  $(48.95 \pm 0.02) \mu\text{m}$  and  $(74.51 \pm 0.02) \mu\text{m}$ . Thus, the hole diameter trend of the foil is also visible in the mean values per segment. Therefore, these mean diameter values are considered suitable for the further analysis of the hole diameter impact on the leakage current. If not explicitly specified otherwise, in the following the term *hole diameter* refers to the mean hole diameter value per foil segment.

### 5.5.2 Results and discussion

In order to get an estimate of the accessible inner and outer diameter ranges and to gain information about their mutual behaviour the correlation between the obtained inner and outer diameter values is illustrated in figure 5.11. Every entry in this histogram corresponds to the inner and outer diameter of one foil segment, while the entire plot is based on all available hole size data for the four foil sizes (I, O1, O2, O3) and both pitches (SP, LP).

As expected an overall linear behaviour between the inner and outer hole diameter is observed. This means, the larger the inner hole diameter, the larger the outer one and vice-versa. Such a dependence is intuitively expected because of the etching process. For example if the foil stays inside the etching bath for a longer time, both diameters accordingly get larger. Furthermore, it can be seen that the inner diameter primarily varies within a value range of approximately  $20 \mu\text{m}$  from  $45 \mu\text{m}$  to  $65 \mu\text{m}$ . Similarly, the outer diameter values are also majorly in a range of  $20 \mu\text{m}$  from slightly below  $70 \mu\text{m}$  to below  $90 \mu\text{m}$ . In both diameter directions the available

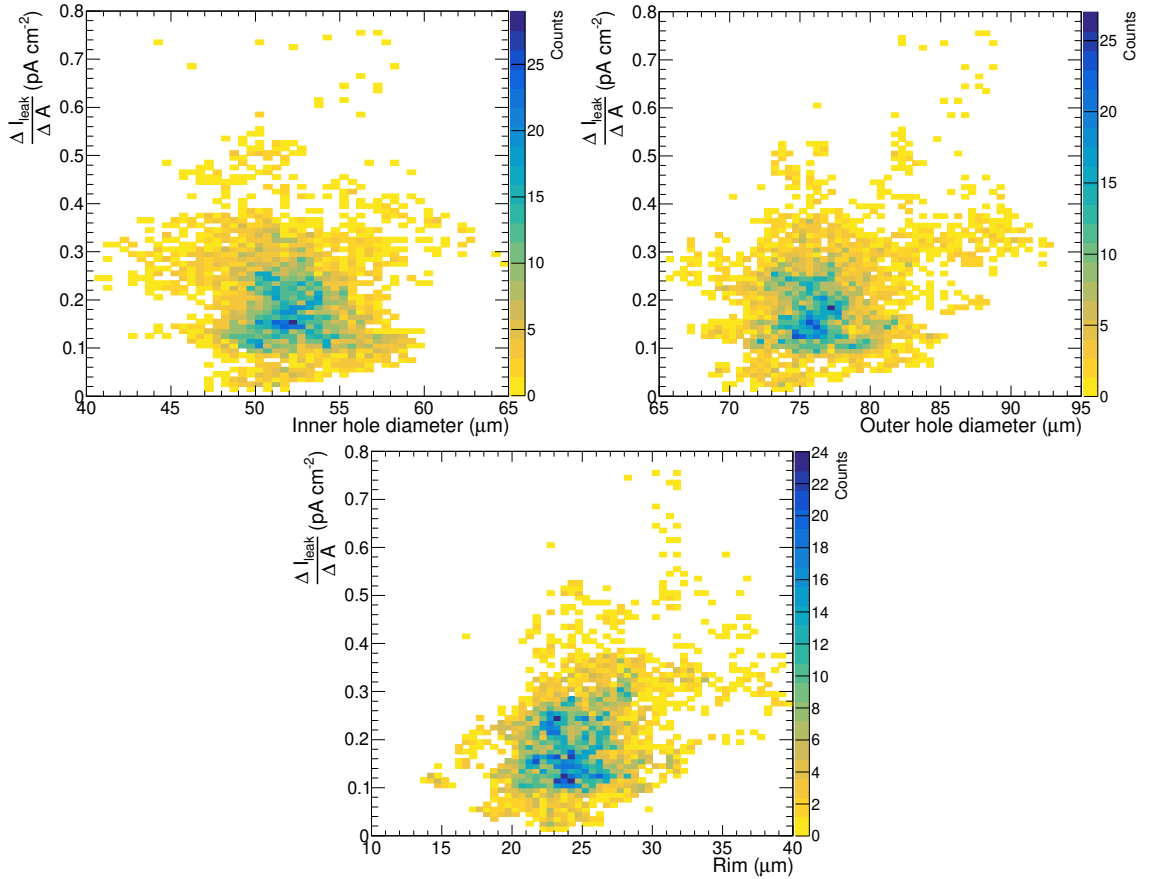


**Figure 5.12** Two-dimensional histograms for the correlation between area normalised leakage current and inner hole diameter (**top, left**), outer hole diameter (**top, right**) and the absolute difference (rim) between inner and outer diameter (**bottom**). Only leakage current data for SP foils measured at CERN is used

statistics decreases when considering extreme values. The most diameter configurations are around  $(52 \pm 5) \mu\text{m}$  for the inner and  $(75 \pm 5) \mu\text{m}$  for the outer hole diameter, which is within the specifications for the ALICE TPC upgrade [21].

In order to investigate the impact of these hole diameter fluctuations on the leakage current of a GEM foil they are correlated to the area normalised leakage current. The three resulting two-dimensional correlation histograms are shown in figure 5.12. At the top left and right the dependence of the area normalised leakage current on the inner and outer hole diameter is shown, respectively. Additionally, the dependence on the rim, which is a measure of how conical the GEM holes are, is illustrated at the bottom of the figure. For all three cases the plots are solely based on area normalised leakage current data from SP foils measured at CERN, since this data set provides slightly higher statistics as compared to the LP case. Furthermore, the upscaling of the LP values to the level of the SP case by the multiplication of the experimentally found ratio is not considered reasonable, since this is linked with too large uncertainties. For example no investigation of systematic effects between SP and LP foils is performed.

At first sight, no strong correlation between the area normalised leakage current and the three hole size parameters is visible. However, taking a closer look at the data some trends are betokened. For example the overall leakage current level seems to increase with increasing outer hole diameter and rim. This means the more conical a GEM hole is, the more leakage current goes through. In turn, it is weakly indicated that the leakage current level increases with decreasing inner hole diameter. Since the inner hole diameter is found to be primarily responsible for the

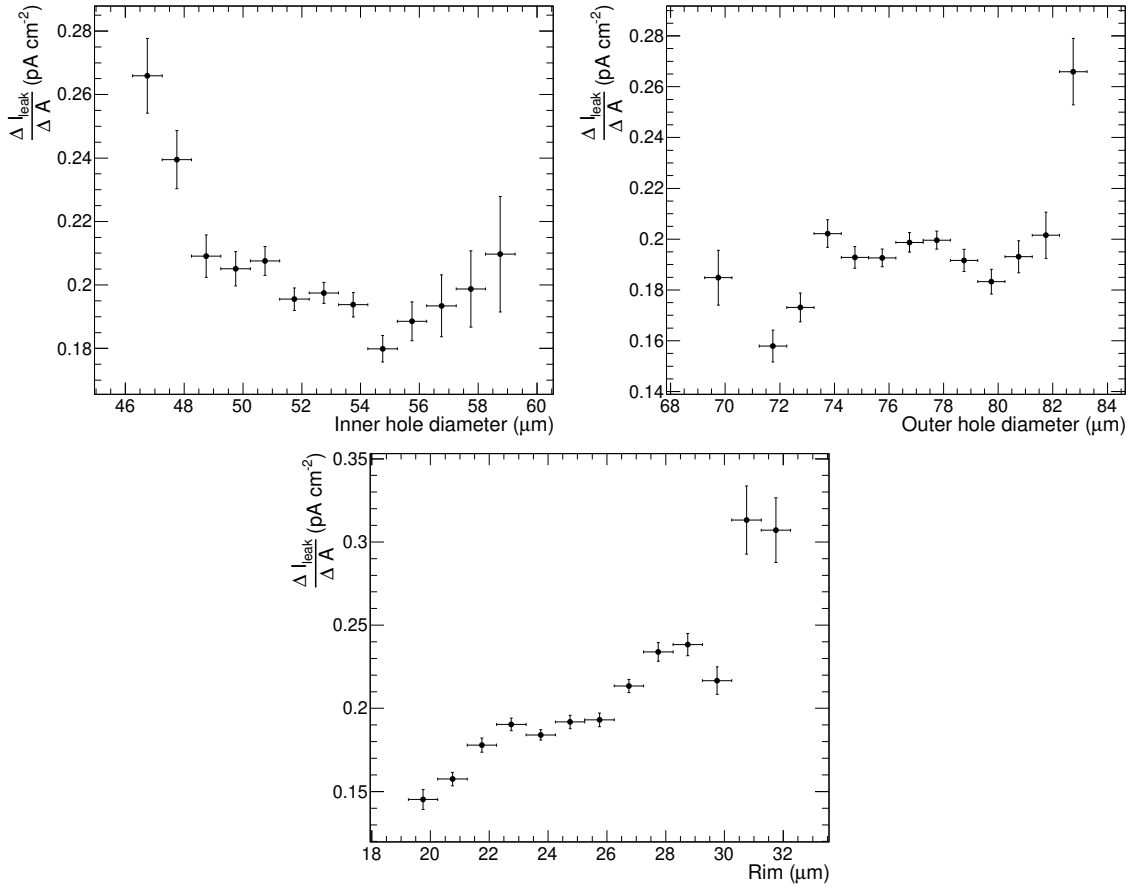


**Figure 5.13** Area normalised leakage current versus inner hole diameter (**top, left**), outer hole diameter (**top, right**) and the absolute difference (rim) between inner and outer diameter (**bottom**). The current values are obtained from the one-dimensional projection distributions from the plots in figure 5.12 along the *diameter-axis* for hole diameter ranges of  $1 \mu\text{m}$  (horizontal error bars)

electrical field strength and thus the individual gain of a GEM hole, the latter effect is an indication that the leakage current is affected by the field.

Whether the observed trends for the leakage current are of statistical relevance needs to be confirmed by further analysis. For this purpose, the area normalised leakage current data, which is illustrated in figure 5.12, is projected into one-dimensional distributions along the *diameter-axis*. Each of these distributions represent the area normalised leakage current within subsequent diameter bins of  $1 \mu\text{m}$  width. The mean value and the according statistical error of each of these distributions is obtained and plotted against the centre of the corresponding diameter range. The resulting diagrams for all three cases are shown in figure 5.13. At the top the mean area normalised leakage current against the inner and outer diameter is illustrated on the left and on the right, respectively. The rim dependence of the leakage current is shown at the bottom. In order to guarantee the statistical relevance of the data points only projection distributions with more than 50 entries are taken into account. The horizontal error bars represent the projected diameter range of  $1 \mu\text{m}$  for each data point.

It is found that the overall trends for the inner diameter and the rim, which are (barely) visible in the two-dimensional correlation plots in figure 5.12, are confirmed by the graphs in figure 5.13. As expected the area normalised leakage current increases towards smaller inner diameters and thus most probably correlates with the electrical field strength (or the individual gain) inside the GEM holes. It can be further seen that the leakage current starts to increase for diameters

larger than  $55\ \mu\text{m}$ . By the means of this thesis there is no explanation for this. Also these values provide very large error bars. Thus, higher statistics is needed in order to clarify this behaviour. Furthermore, a clear correlation between the area normalised leakage current and the rim is found. Except for one outlier a linear dependence can be estimated. In this case the possible explanation goes in the same direction as for the inner hole diameter dependence, since also the conicity of the GEM holes has an effect on the electrical field. For the outer hole diameter the kind of the correlation is not that clear. Disregarding the last data point, even no correlation, i.e. a constant behaviour of the leakage current with a varying outer hole diameter, is considered a possibility.

In order to gain more information about the nature of the correlation between the leakage current and the geometrical hole properties more statistics is required. Further suggestions on how to improve this kind of analysis are given in the following chapter 6.

## 6 Conclusion and outlook

In this work the measurement (procedure) of the leakage current through a GEM foil in the framework of the ALICE TPC upgrade is described in detail. To check the comparability of the different institutes, which perform the leakage current test with the same GEM foils, their overall measured leakage current level are compared. It was found that the data of different institutes is not compatible. For comparability reasons, only data provided by CERN is used, since it offers the largest possible statistics as a single institute. A statistical analysis of this leakage current data is performed in order to identify different determining factors of the small leakage currents. There, the correlations between the leakage current and the size of the active area, the pitch size and the geometrical hole properties such as the inner and outer hole diameter and the conicity of the GEM holes are investigated. In the following, limitations and possible improvements as well as new analysis strategies are presented and discussed.

**Leakage current measurement** Performing the leakage current test multiple times, there are suggestions concerning the testing procedure which is described in section 4.3. To avoid humidity during the measurement process the test box is flushed with nitrogen gas with a relatively high flow, which is then strongly reduced during the data taking to prevent the foil from vibrating. However, the absolute gas flow is neither measured nor prescribed. Therefore, it depends on the subjective perception of the testing person, which may lead to an incomparability not only between the different measurement institutes, but also between single measurements.

An example why the leakage current dependence on the gas flow and thus the foil vibration should be subject of further analysis is the influence of the foil framing. The comparability test between the different institutes revealed that the framing of the foil seems to lower their leakage current level. This can be linked to the higher mechanical sturdiness of a framed foil as compared to an unframed one, which makes them less prone to vibration. However, in theory higher vibration amplitudes would only lead to a higher noise and therefore a larger standard deviation, but would not affect the mean value. In order to clarify this, a dedicated investigation of the gas flow and framing impacts on the leakage current is proposed.

Moreover, in the comparison of the institutes only the leakage current levels are compared in order to check their comparability. The finding that the leakage current data is not comparable results in a strong limitation of the statistics, which then cannot be exploited in the analysis of the determining factors of the leakage current. For this reason, further research on the systematics of the institutes is needed in order to correct for them and thus increase the available statistics for further analysis. In this framework, the investigation of the influences of environmental factors such as temperature, gas pressure and humidity is suggested.

Also one has to keep in mind, that the increase of statistics by including data from all segments may not necessarily result in a much higher statistical significance, since the GEM foil segments are not independent. During a leakage current measurement they can interact electromagnetically via capacitive coupling and thus influence each other. A comparison with measurements where only one GEM segment is powered may provide information about the coupling strength and the significance of the impact on the individual leakage currents of adjacent segments.

As outlined in section 4.4 the reference measurement and offset subtraction from the measurement data is a crucial point. If this correction is not done correctly the entire measurement loses its informative value. Therefore, GSI includes the first seconds of the measurement process

---

in its raw data files to be able to check the correct offset subtraction in retrospect. However, other institutes do not stick to this or even use another correction scheme (Bonn). For this reason, it is not possible to assess the relevance of this measurement within a statistical analysis. For the evaluation of the foil quality this issue is of minor importance, since well performing foil will nonetheless have a leakage current below the test requirement, even with an incorrect offset correction. A unified prescription of the measurement process, especially concerning this reference measurement and correction procedure, would further contribute to the comparability between the different institutes and increase the data quality.

**Area dependence of leakage current** In section 5.3 it is demonstrated that the leakage current of a GEM foil is linearly dependent on the active area of the segment. With this result the naive expectation of the proportionality between area and leakage current is confirmed. Furthermore, distinct contributions of the different foil sizes (I, O1, O2, O3) are identified (cf. figure 5.5). Since there is the tendency that I and O3 foils as well as O1 and O2 foils are grouped in the sense that they can be described by two individual linear laws, the different contributions are most probably caused by systematic effects in the production process of the foils. There, I and O3 foils and O1 and O2 foils are produced (etched) on the same *sheet*, respectively [39]. This means that these two groups of foils are affected by the same systematics during the production process until they are cut apart, which may result in their slightly different leakage current levels. However, this hypothesis needs further investigation.

The usage of the design values for the segment areas is another systematic effect, which may modify the results of this analysis. Taking a closer look at a GEM foil segment (cf. figure 4.1 on the left) it can be seen that the active area of the segment (perforated) is surrounded by a narrow copper band without holes. This inactive part is also included in the used area values. Therefore, it is proposed to remeasure the active area of the foil segments explicitly taking into account the inactive parts. Since the circumference is not linearly correlated to the segment area, the fraction of inactive parts varies with each segment size. However, since the relative fraction of the inactive parts of a segment is small, this is considered a small effect for the area dependence of the leakage current. In contrast, for the area normalisation of the leakage current, which is crucial for the investigation of the pitch size and hole property impact, the corrected active area values would most probably increase the quality of these correlations.

Limited by the accessible area range, especially the inclusion of measurements on GEM foils with smaller segment sizes or active areas would significantly improve the informative value of this analysis. For example leakage current data from other projects that involve GEM technology could be utilised. Especially, the behaviour of very small foils is of interest to gain more reliable information of a possible (non-zero) offset and to investigate effects at the segment borders.

**Pitch size dependence of leakage current** A clear dependence of the leakage current on the pitch size and thus the hole density is found in section 5.4. The qualitative expectation that the leakage current increases with increasing hole density (decreasing pitch size) is confirmed. Additionally, it is shown with high significance that the leakage current cannot be understood by solely regarding the hole density. Therefore, other additional factors must contribute the leakage current of a GEM foil. Since also ordinary plate capacitors show leakage current, boundary effects at a segment's delimitation or defects in the insulator material are possible candidates to explain the found discrepancy. There, a comparison between unperforated, but segmented foils is proposed in order to verify the impact of these suggested possibilities.

Also the investigation of more than just two different pitch sizes would massively contribute to the understanding of the hole density impact on the leakage current. Additionally, other hole patterns may lead to a modified leakage current and can be included in the analysis.

**Dependence of leakage current on geometrical hole properties** The influence of the geometrical hole properties such as the inner and outer hole diameter and the conicity of the GEM holes are evaluated in section 5.5. Clear trends are found that the leakage current increases with decreasing inner hole diameter and decreasing conicity. Since the individual gain of a GEM hole is primarily determined by the inner hole size this a strong indication that the leakage current is correlated with the electrical field strength inside the holes. The gain also depends on the type of the working gas, pressure and temperature. Therefore, this behaviour can be verified, if such dependencies are found in further analyses. On the contrary, no clear correlation with the outer hole diameter is found.

Due to the fact that this analysis is based on the statistical fluctuations of the hole diameters, the covered value ranges are at maximum 20  $\mu\text{m}$ . Also the statistics for diameter values decreases drastically with increasing deviation from the nominal value. As a consequence, the significance of this analysis could be increased by increasing the statistics for extreme diameter values and the consideration of a broader value range. The latter can be achieved by explicitly producing GEM foils with bigger holes, which corresponds to longer etching times.

Moreover, the hole size information of a GEM segment is condensed into one single mean value, which is a very strong simplification. As it can be seen in figure 5.9 the variations of the hole diameters by trend show vertical patterns whereas the segments are oriented horizontally. Also in figure 5.10 it can be seen that the geometrical constraints of the segments lead to a *loss* of hole size data. For example, three distinct hole diameter contributions are mapped together in order to describe the mean of the segment. In order to account for this problem a foil segmentation with a higher granularity is needed in order to get more reliable, representative values for the hole size of a certain area. The improved mapping of the hole size values due to smaller foil segments would also have the effect that the statistics for the different hole diameter ranges (bins) are more equally distributed.

Within the scope of this thesis the influences of different determining factors on the leakage current flowing through a GEM foil are analysed. Clear correlations between the leakage current and the three investigated factors are demonstrated. Moreover, the found kinds of dependency or at least the trends are expected or can be explained by different hypotheses (additional investigation needed). Furthermore, clear evidence for the existing of further contributions to the leakage current is found. For the better understanding of effects in the already performed analyses and thus to increase their informative value as well as the investigation of the further determining factors proposals of supplementary experiments and analysis strategies are given.

# Appendices

## A.1 List of abbreviations (in alphabetical order)

### A

ACORDE	ALICE COsmic Ray DEtector
AD	Antiproton Decelerator
ALICE	A Large Ion Collider Experiment
APD	Avalanche Photo-Diode
ATLAS	A Toroidal LHC ApparatuS
AWAKE	Advanced WAKefield Experiment

### B

BNL	Brookhaven National Laboratory
-----	--------------------------------

### C

CE	Central Electrode
CERN	Conseil Européen pour la Recherche Nucléaire (European Council for Nuclear Research)
CMS	Compact Muon Solenoid

### E

EIC	Electron Ion Collider
ELENA	Extra Low ENergy Antiproton (deceleration ring)
EMCal	ElectroMagnetic Calorimeter

### F

FC	Field Cage
FAIR	Facility for Antiproton and Ion Research
FMD	Forward Multiplicity Detector
FWD	ForWard Detectors

### G

GEM	Gas Electron Multiplier
GG	Gating Grid
GSI	Gesellschaft für SchwerIonenforschung mbH (Helmholtz Center for Heavy Ion Research)

### H

HiRadMat	High-Radiation to Materials
HMPID	High-Momentum Particle IDentification (detector)
HV	High Voltage

### I

IBF	Ion BackFlow
IROC	Inner ReadOut Chamber
ISOLDE	Isotope Separator OnLine DEvice
ITS	Inner Tracking System

### L

LEIR	Low Energy Ion Ring
LHC	Large Hadron Collider
LHCb	Large Hadron Collider beauty
LINAC	LINear ACcelerator
LP	Large Pitch (280 $\mu\text{m}$ )
LS2	Long Shutdown 2

**M**

MAPS	Monolithic Active Pixel Sensors
MRPC	Multi-gap Resistive Plate Chamber
MSGC	Micro-Strip Gas Counter
MWPC	Multi Wire Proportional Chamber

**N**

n-ToF	neutrons Time of Flight
-------	-------------------------

**O**

OROC	Outer ReadOut Chamber
------	-----------------------

**P**

PCB	Printed Circuit Board
PHOS	PHOTon Spectrometer
PID	Particle IDentification
PMD	Photon Multiplicity Detector
PS	Proton Synchrotron

**Q**

QA	Quality Assurance
QCD	Quantum ChromoDynamics
QGP	Quark-Gluon Plasma

**R**

RHIC	Relativistic Heavy Ion Collider
RICH	Ring Imaging CHerenkov detector

**S**

SDD	Silicon Drift Detector
SP	Standard Pitch (140 $\mu\text{m}$ )
SPD	Silicon Pixel Detector
SPS	Super Proton Synchrotron
SSD	Silicon Strip Detector

**T**

TOF	Time Of Flight (Detector)
TPC	Time Projection Chamber
TPCU	Time Projection Chamber Upgrade
TRD	Transition Radiation Detector
TUM	Technische Universität München

**W**

WSU	Wayne State University
-----	------------------------

**Z**

ZDC	Zero Degree Calorimeter
-----	-------------------------

**A.2 List of figures**

1.1	Sketch: Confinement and fragmentation	2
1.2	Sketch: QCD phase diagram and QGP evolution in heavy-ion collisions	3
1.3	Sketch: CERN's accelerator complex	5
1.4	Sketch: ALICE detector system	6
1.5	Sketch: ALICE TPC and MWPC readout schematic	8
1.6	Plot: Particle identification with the ALICE TPC	10

2.1	Image: Microscope picture of a standard GEM foil . . . . .	13
2.2	Sketch: Electrical field and avalanche creation inside GEM holes . . . . .	14
2.3	Sketch: Two different detector concepts using GEMs . . . . .	15
3.1	Plot: Simulations of invariant $e^+e^-$ mass spectra for the current and upgraded TPC	18
3.2	Sketch and Image: Schematics of the new IROC and OROC design and photograph of GEM foils . . . . .	19
3.3	Image: Cross section through a GEM hole . . . . .	20
3.4	Sketch and plot: Schematic of the GEM stack design and plot of the IBF-energy-resolution correlation . . . . .	21
3.5	Sketch: Numbering scheme of the GEM foil segments . . . . .	22
3.6	Sketch: Schematic of the workflow in the TPC upgrade . . . . .	23
4.1	Image and sketch: Closeup of foil segments and HV path and wiring diagram of the leakage current test setup . . . . .	26
4.2	Images: Main steps of the leakage current testing procedure . . . . .	28
4.3	Plots: Typical signals from the leakage current measurement . . . . .	31
5.1	Plots: Exemplary histograms to obtain a central value for the leakage current of one foil segment . . . . .	34
5.2	Plots: Comparison of leakage current levels from different measurement sites . . . . .	35
5.3	Sketch: Segment areas of IROC and OROC GEM foils . . . . .	36
5.4	Plots: 2D correlation plots of leakage current and segment area for SP and LP foils	37
5.5	Plots: Linear dependence of the leakage current on the segment area and the contributions of the different foil sizes . . . . .	38
5.6	Sketch: Comparison of the hole densities for SP and LP foils . . . . .	40
5.7	Plots: 2D correlation plots of area normalised leakage current and segment area for SP and LP foils . . . . .	41
5.8	Plots: Area normalised leakage current distributions for SP and LP foils . . . . .	42
5.9	Plots: 2D hole size maps for inner and outer diameters of an O3 foil . . . . .	44
5.10	Plots: Inner and outer hole diameter distributions from two segments of an O3 foil	45
5.11	Plot: 2D correlation histogram between outer and inner hole diameter . . . . .	46
5.12	Plots: 2D correlation histograms between hole diameter and area normalised leakage current for SP foils . . . . .	47
5.13	Plots: Dependence of area normalised leakage current on three different hole diameter scenarios . . . . .	48
A.1	Plots: Leakage current distributions for each segment area of O3 foils . . . . .	56

### A.3 List of tables

3.1	Number of segments per foil size . . . . .	22
4.1	Rough nominal capacitance of OROC GEM foils . . . . .	30
5.1	Results of the linear fits for the area-leakage-current correlation . . . . .	39
5.2	Analysis results for the pitch size dependence of leakage current . . . . .	43

## A.4 Additional figures

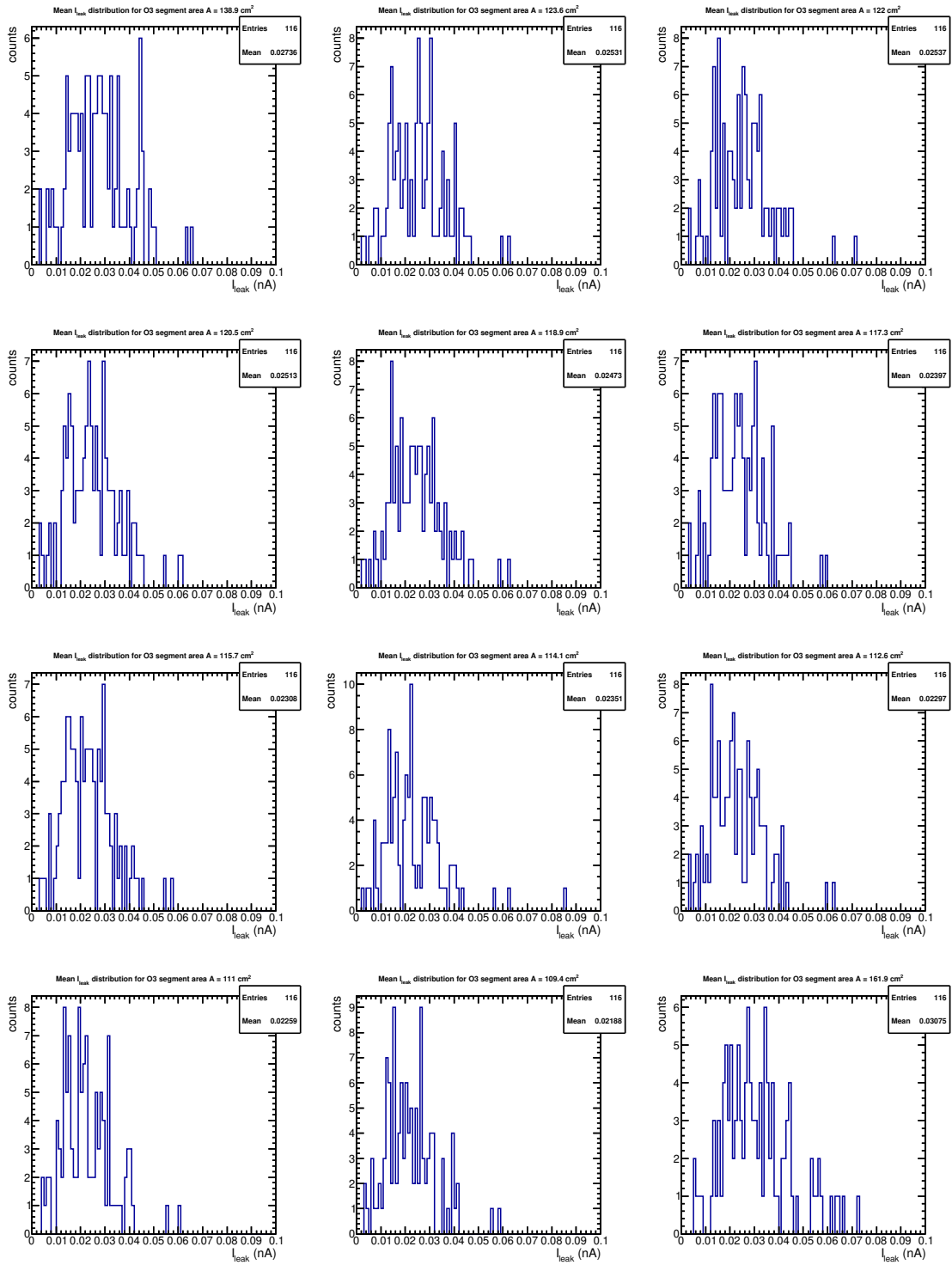


**Figure A.1** Exemplary leakage current distributions for each segment area of O3 foils. Since an O3 foil is subdivided in 24 segments, which are pairwise mirror-symmetric, there are 12 different segment areas

# References

- [1] K. Aamodt et al. The ALICE experiment at the CERN LHC. *JINST*, 3:S08002, 2008.
- [2] Anton Andronic. An overview of the experimental study of quark-gluon matter in high-energy nucleus-nucleus collisions. *Int. J. Mod. Phys.*, A29:1430047, 2014.
- [3] Longer term LHC schedule.  
<https://lhc-commissioning.web.cern.ch/lhc-commissioning/schedule/LHC-long-term.htm>  
(Accessed: 04 March 2018), January 2016.
- [4] J. Schukraft. Heavy Ion physics with the ALICE experiment at the CERN LHC. *Phil. Trans. Roy. Soc. Lond.*, A370:917–932, 2012.
- [5] C. Patrignani et al. Review of Particle Physics. *Chin. Phys.*, C40(10):100001, 2016.
- [6] Apoorva Patel. A flux tube model of the finite temperature deconfining transition in qcd. *Nuclear Physics B*, 243(3):411 – 422, 1984.
- [7] Philip Tanedo. QCD and confinement.  
<https://www.quantumdiaries.org/2010/10/22/qcd-and-confinement/> (Accessed: 05 March 2018).
- [8] Mengliang Wang, Magali Estienne, Sonja Kabana, Alexandre Shabetai, and Daicui Zhou. Measurement of jet fragmentation functions and of their moments in  $pp$  collisions at  $\sqrt{s} = 2.76$  TeV with ALICE at the LHC. Mesure des fonctions de fragmentation des jets et de leurs moments dans les collisions  $pp$  à  $\sqrt{s} = 2.76$  TeV avec ALICE au LHC, Dec 2016. Presented 10 Dec 2016.
- [9] Michael Strickland. Anisotropic Hydrodynamics: Three lectures. *Acta Phys. Polon.*, B45(12):2355–2394, 2014.
- [10] Declan Keane. The Beam Energy Scan at the Relativistic Heavy Ion Collider. *Journal of Physics: Conference Series*, 878(1):012015, 2017.
- [11] J. Alme et al. The alice tpc, a large 3-dimensional tracking device with fast readout for ultra-high multiplicity events. *Nuclear Instruments and Methods in Physics Research Section A: Accelerators, Spectrometers, Detectors and Associated Equipment*, 622(1):316 – 367, 2010.
- [12] Jaroslav Adam et al. Centrality dependence of the pseudorapidity density distribution for charged particles in Pb-Pb collisions at  $\sqrt{s_{NN}} = 5.02$  TeV. *Phys. Lett.*, B772:567–577, 2017.
- [13] P. Braun-Munzinger and J. Stachel. Charmonium from Statistical Hadronization of Heavy Quarks: A Probe for Deconfinement in the Quark-Gluon Plasma. *Landolt-Bornstein*, 23:424, 2010.
- [14] Renaud Vernet. Soft Probes of the Quark-Gluon Plasma with ALICE at LHC. In *24th Lake Louise Winter Institute: Fundamental Interactions (LLWI 2009) Lake Louise, Alberta, Canada, February 16-21, 2009*, 2009.

- [15] CERN's accelareator complex. <http://www.stfc.ac.uk/research/particle-physics-and-particle-astrophysics/large-hadron-collider/cern-accelerator-complex/> (Accessed: 07 March 2018).
- [16] Kyrre Skjerdal and the ALICE collaboration. Photoproduction of  $\rho^0$  in ultra-peripheral nuclear collisions at alice. *Journal of Physics: Conference Series*, 455(1):012010, 2013.
- [17] Betty Bezverkhny Abelev et al. Performance of the ALICE Experiment at the CERN LHC. *Int. J. Mod. Phys.*, A29:1430044, 2014.
- [18] G. Dellacasa et al. ALICE: Technical design report of the time projection chamber. 2000.
- [19] J. Wiechula. *Commissioning and Calibration of the ALICE TPC*. PhD thesis, Goethe-Universität Frankfurt am Main, 2008.
- [20] Silvia Masciocchi. Physics of particle detectors–Gaseous detectors 1. Presentation slides 10 May, Master course (summer term), University of Heidelberg, 2017.
- [21] Christian Lippmann et al. Upgrade of the ALICE Time Projection Chamber. 2014.
- [22] R. Schicker. Overview of ALICE results in pp, pA and AA collisions. *EPJ Web Conf.*, 138:01021, 2017.
- [23] Silvia Masciocchi. Physics of particle detectors–Interaction of particles with matter 1. Presentation slides 27 April, Master course (summer term), University of Heidelberg, 2017.
- [24] Fabio Sauli. Principles of operation of multiwire proportional and drift chambers. page 92 p, Geneva, 1977. CERN, CERN. CERN, Geneva, 1975 - 1976.
- [25] F. Sauli. GEM: A new concept for electron amplification in gas detectors. *Nucl. Instrum. Meth.*, A386:531–534, 1997.
- [26] Fabio Sauli. The gas electron multiplier (GEM): Operating principles and applications. *Nucl. Instrum. Meth.*, A805:2–24, 2016.
- [27] DuPont™ Kapton® Summary of Properties. <http://www.dupont.com/content/dam/dupont/products-and-services/membranes-and-films/polyimide-films/documents/DEC-Kapton-summary-of-properties.pdf> (Accessed: 04 April 2018).
- [28] F. V. Böhmer et al. Simulation of Space-Charge Effects in an Ungated GEM-based TPC. *Nucl. Instrum. Meth.*, A719:101–108, 2013.
- [29] M. Killenberg et al. Modeling and measurement of charge transfer in multiple GEM structures. *Nucl. Instrum. Meth.*, A498:369–383, 2003.
- [30] M. Ball, K. Eckstein, and T. Gunji. Ion backflow studies for the ALICE TPC upgrade with GEMs. *JINST*, 9:C04025, 2014.
- [31] M. Blatnik et al. Performance of a Quintuple-GEM Based RICH Detector Prototype. *IEEE Trans. Nucl. Sci.*, 62(6):3256–3264, 2015.
- [32] Giovanni Bencivenni et al. The Cylindrical-GEM detectors for the KLOE-2 Inner Tracker. *PoS, Bormio2014:047*, 2014.
- [33] CERN. Inverse Femtobarn. <http://writing-guidelines.web.cern.ch/entries/inverse-femtobarn> (Accessed: 04 April 2018).

- 
- [34] C. Lippmann. A continuous read-out tpc for the alice upgrade. *Nuclear Instruments and Methods in Physics Research Section A: Accelerators, Spectrometers, Detectors and Associated Equipment*, 824:543 – 547, 2016. Frontier Detectors for Frontier Physics: Proceedings of the 13th Pisa Meeting on Advanced Detectors.
- [35] Ernst Hellbär. Ion Movement and Space-Charge Distortions in the ALICE TPC. mathesis, Institut für Kernphysik Goethe-Universität, Frankfurt am Main, 2015.
- [36] T. Rudzki. Commissioning and testing of large-area GEM-based readout chambers for the high-rate ALICE TPC. Master thesis, University of Heidelberg, 2017.
- [37] Harald Appelshäuser. ALICE selects gas electron multipliers for its new TPC. *CERN Courier*, March 2016.
- [38] S. Bachmann et al. Discharge mechanisms and their prevention in the gas electron multiplier (GEM). *Nucl. Instrum. Meth.*, A479:294–308, 2002.
- [39] M. Ball, B. Ketzer, J. Ottnad, V. Ratza, and S. Urban. Quality assurance of gem foils for the upgrade of the alice tpc. *Journal of Instrumentation*, 12(01):C01081, 2017.
- [40] National Instruments Corporation. LabVIEW™ User Manual. <http://www.ni.com/pdf/manuals/320999e.pdf> (Accessed: 04 April 2018), April 2003.
- [41] Manuel Jahn. Quality assurance for gas electron multipliers with the leakage current test. Bachelor thesis, University of Heidelberg, 2017.
- [42] CERN. ROOT Data Analysis Framework. <https://root.cern.ch/> (Accessed: 28 March 2018).
- [43] Piotr Gasik. Segment areas of IROC and OROC GEM foils. Personal communication.

# Acknowledgement

First and foremost, I would like to express my gratitude to Silvia Masciocchi who gave me the opportunity to join the ALICE group at GSI and to perform the research for this thesis within the framework of the ALICE TPC upgrade. In particular, I am grateful for her kind supervision and the various discussions and meetings, which were always very instructive.

Furthermore, I would like to thank Dariusz Miskowiec for his patient coordination and explanation of the laboratory work. In addition to that, he always had helpful comments and ideas concerning the analysis strategy of the leakage current data.

I am also indebted to Lukas Kreis and Daniel Baitinger who spend many hours in the cleanroom and performed the leakage current tests with me. The suffering due to the long measurement time was always eased by some entertaining conversations.

Moreover, my gratitude goes to my office mates Sebastian Hornung, Tonatiuh Bustamente and Alexander Deisting for their multi-faceted comments on my work and helpful pieces of advice especially concerning ROOT.

In general, I would like to thank the entire group for being welcoming, outspoken and accommodating from the beginning on. I had a great and informative time at GSI.

For his nonbiased (in terms of physics), rapid language correction I would furthermore thank Clemens Krüger whom I can always count on.

Evidently, I owe all the people who are not mentioned by name, but contributed to this thesis in terms of proofreading, posing helpful comments or motivating me during the work and especially the writing process, a debt of gratitude.

Not to forget, special thanks to Sophie Klett for being a reliable partner throughout the hole time of studies. Her endless mental support is well appreciated.

Ond z'guader Letschd mecht I moine Eldera dange ohne selle mei Physik Schtudium in derra Form 'edd meglich g'wäsa wär. I kennt jeddz a haufa Sächle uffzähla wofir I eich dangbar ben, ab'r ihr wisset jo: Nedd gmäggert isch globt gnuag.

# Declaration

I declare that this thesis has been composed solely by myself and that it has not been submitted, in whole or in part, in any previous application for a degree. Except where stated otherwise by reference or acknowledgment, the work presented is entirely my own.

# Erklärung

Ich versichere, dass ich diese Arbeit selbstständig verfasst und keine anderen als die angegebenen Quellen und Hilfsmittel benutzt habe.

Heidelberg, April 5, 2018

Pascal Becht